

1-1-2003

# An integrated positioning system for the Toronto Transit System

Mahmoud Salem I.S. Abd El-Gelil

*Ryerson University*

Follow this and additional works at: <http://digitalcommons.ryerson.ca/dissertations>



Part of the [Civil Engineering Commons](#)

---

## Recommended Citation

Abd El-Gelil, Mahmoud Salem I.S., "An integrated positioning system for the Toronto Transit System" (2003). *Theses and dissertations*. Paper 10.

This Thesis is brought to you for free and open access by Digital Commons @ Ryerson. It has been accepted for inclusion in Theses and dissertations by an authorized administrator of Digital Commons @ Ryerson. For more information, please contact [bcameron@ryerson.ca](mailto:bcameron@ryerson.ca).

# An Integrated Positioning System for the Toronto Transit System

By

Mahmoud Salem I. S. Abd El-Gelil

(M.Sc. Alexandria Univ., Alexandria, Egypt, 1998)

A Thesis

Submitted to Ryerson University

School of Graduate Studies

In partial fulfillment of the requirement of degree of  
Master of Applied Science

In the Program of  
Civil Engineering

Toronto, Ontario, Canada

September, 2003

© Mahmoud Abd El-Gelil 2003



National Library  
of Canada

Bibliothèque nationale  
du Canada

Acquisitions and  
Bibliographic Services

Acquisitions et  
services bibliographiques

395 Wellington Street  
Ottawa ON K1A 0N4  
Canada

395, rue Wellington  
Ottawa ON K1A 0N4  
Canada

*Your file    Votre référence*

*ISBN: 0-612-85316-0*

*Our file    Notre référence*

*ISBN: 0-612-85316-0*

The author has granted a non-exclusive licence allowing the National Library of Canada to reproduce, loan, distribute or sell copies of this thesis in microform, paper or electronic formats.

L'auteur a accordé une licence non exclusive permettant à la Bibliothèque nationale du Canada de reproduire, prêter, distribuer ou vendre des copies de cette thèse sous la forme de microfiche/film, de reproduction sur papier ou sur format électronique.

The author retains ownership of the copyright in this thesis. Neither the thesis nor substantial extracts from it may be printed or otherwise reproduced without the author's permission.

L'auteur conserve la propriété du droit d'auteur qui protège cette thèse. Ni la thèse ni des extraits substantiels de celle-ci ne doivent être imprimés ou autrement reproduits sans son autorisation.

**Canada**

### **Author's declaration**

I hereby declare that I am the sole author of the thesis. I authorize Ryerson University to lend this thesis to other institutions or individuals for the purpose of scholarly research. I further authorize Ryerson University to reproduce this thesis by photocopying or by other means, in total or part, at the request of other institutions or individuals for the purpose of scholarly research.

Signature

-----

## Borrowers

Borrowers undertake to give proper credit for any use made of the thesis. Ryerson University requires the signatures of all persons using or photocopying this thesis.

Please sign below and give address and date.

[illegible]

## **ABSTRACT**

### **An Integrated Positioning System for the Toronto Transit System**

Mahmoud Salem I. S. Abd El-Gelil  
(M.Sc. Alexandria Univ, Alexandria, Egypt, 1998)  
Master of Applied Science  
In the Program of Civil Engineering  
Ryerson University (2003)

In this thesis, a hybrid positioning system is developed, which combines GPS, Dead Reckoning (DR) and Signpost technologies for the purpose of improving the Toronto Transit System bus service. The DR system is used as the main positioning system, while GPS and Signpost systems are used as aiding systems to compensate for the DR errors. The integration is done in the position domain, which simplifies the system design. A centralized Kalman filter with five states is developed to combine all the available measurements. Field tests have been designed and conducted to assess the system design and performance under various environmental conditions. It is shown that the achieved positioning accuracy of the integrated DR/GPS/Signpost system is at the few metres level in unobstructed environments. In addition, despite the signal obstruction in the downtown area, the positioning solution of the integrated system is still sufficiently precise.

## Acknowledgements

I would like to express my gratitude to my supervisor, Dr. Ahmed El-Rabbany, for his continuous guidance, support, and encouragement throughout my graduate studies. His guidance and advice are greatly appreciated. I was extremely lucky to have a supervisor like him.

This research was funded by the Geomatics for Informed Decision (GEOIDE) NCE, the Communications and Information Technology Ontario (CITO), and the Department of Civil Engineering Graduate Research Scholarships and Teaching Assistantship. Their contributions are gratefully acknowledged.

I would like to thank my friends, Morad L'Mehery and Waleed Mostafa, for their help in preparing the connections of the integrated system. Also, I would like to thank Warda from the Electrical Engineering Department for spending a lot of time explaining a lot of things in the digital design concepts. Thanks also go to Sokkia Corp. for providing a differential GPS system at no cost and to DTMI Spatial Inc. for providing a digital map for the Greater Toronto Area.

I wish to express my gratitude to Dr. Aboelmagd Noureldin, Royal Military College of Canada, for his advices and discussions during this research. To my good friends in Toronto, who are always there for me, many thanks for your endless support, especially Dr. Aly Emam, Mr. Essam Dabbour, Mr. Mohamad El-Diasty, Mr. Ibrahim Abd El-Lateef and Mr. Rifaat Abdul Allah.

Last, but not least, thank you to all my family members in Egypt. Special thanks go to my father, Salem; my brother, El-Sayed; and my sisters for supporting me. Also, I owe thanks to my wife and my sons, Salem and Ahmed, for their patience, support, and encouragement. I cannot forget my son Ahmed words: *“Stay in your office until you finish your master’s.”*

## **Dedication**

To My Friend

**Dr. Beshr**

"You were in my heart and mind during this period."



## Table of Contents

Author's declaration.....	ii
Borrowers.....	iii
Abstract.....	iv
Acknowledgements.....	v
Dedication.....	vi
Table of Contents.....	vii
List of Tables.....	ix
List of Figures.....	x
Notation.....	xii
CHAPTER 1: INTRODUCTION.....	1
1.1 STATEMENT OF THE PROBLEM.....	3
1.2 LITERATURE REVIEW.....	4
1.3 THESIS OBJECTIVES.....	9
1.4 CONTRIBUTION OF THE RESEARCH.....	10
1.5 THESIS OUTLINE.....	10
CHAPTER 2: CONVENTIONAL POSITIONING SYSTEMS.....	12
2.1 DEAD RECKONING.....	12
2.1.1 Distance Sensors.....	13
2.1.1.1 <i>Variable Reluctance Sensor</i> .....	15
2.1.1.2 <i>Hall-Effect Sensor</i> .....	17
2.1.1.3 <i>Eddy Current Sensors</i> .....	20
2.1.1.4 <i>Optical Sensors</i> .....	21
2.1.1.5 <i>Differential Odometry</i> .....	22
2.1.2 HEADING SENSORS.....	23
2.1.2.1 <i>Mechanical Gyros</i> .....	24
2.1.2.2 <i>Vibratory Gyros</i> .....	26
2.1.2.3 <i>Optical Gyros</i> .....	28
2.2 SIGNPOST POSITIONING SYSTEM.....	37
2.2.1 Signpost System Components.....	38
2.2.1.1 <i>Antennas</i> .....	39
2.2.1.2 <i>Transmitter Electronics</i> .....	39
2.2.1.3 <i>Receiver Electronics</i> .....	41
CHAPTER 3: GLOBAL POSITIONING SYSTEM.....	43
3.1 GPS COMPONENTS.....	43
3.2 GPS OBSERVATIONS.....	45
3.3 GPS ERRORS AND BIASES.....	48
3.3.1 Orbital Error.....	49
3.3.2 Satellite and Receiver Clock Errors.....	49
3.3.3 Multipath Error.....	50
3.3.4 System Noise.....	51
3.3.5 Tropospheric Error.....	52
3.3.6 Ionospheric Error.....	54

3.3.7 Satellite Geometry Effect.....	54
CHAPTER 4: METHODOLOGY .....	56
4.1 AIDING INTEGRATED SYSTEM .....	56
4.2 DEAD RECKONING MEASUREMENTS .....	57
4.3 KALMAN FILTER DESIGN.....	59
4.3.1 Kalman Filter .....	59
4.3.2 Position Error.....	63
4.3.3 Scale Factor Stochastic Model.....	65
4.3.4 Azimuth Error and Gyro Drift .....	66
4.3.4 Kalman Filter Parameters and States .....	68
CHAPTER 5: EXPERIMENTAL WORK AND RESULTS ANALYSIS.....	72
5.1 SENSORS DESCRIPTION .....	72
5.1.1 Dead Reckoning Sensors .....	73
5.1.1.1 KVH E-Core 1000 Fiber Optic Gyro .....	73
5.1.1.2 Wheel Sensor.....	75
5.1.2 Dead Reckoning Interface and Time Tag .....	75
5.1.3 G8 Ashtech Receiver .....	76
5.2 HARDWARE ARCHITECTURE .....	78
5.3 DESCRIPTION OF SOFTWARE .....	78
5.4 TEST DESCRIPTION.....	80
5.4.1 Test One .....	81
5.4.1.1 The DR System Alone .....	84
5.4.1.2 The DR/Signpost Solution .....	85
5.4.1.3 GPS/DR/Signpost integrated System .....	87
5.4.2 Test Two .....	87
5.4.2.1 The DR System Alone .....	88
5.4.2.2 The DR/Signpost Solution .....	89
5.4.2.3 The DR/GPS Solution .....	91
5.4.2.4 GPS/DR/Signpost integrated System with GPS outages.....	91
5.4.3 Remarks on Open Area Test.....	92
5.5 MASKED AREA TEST .....	94
5.5.1 The DR System Alone .....	95
5.5.2 The DR/Signpost Solution .....	95
5.5.3 The DR/GPS Solution.....	97
5.5.4 GPS/DR/Signpost Integrated System .....	97
CHAPTER 6: CONCLUSIONS AND RECOMMENDATIONS.....	100
6.1 CONCLUSIONS.....	100
6.2 RECOMMENDATIONS.....	102
REFERENCES .....	103

## **List of Tables**

Table 2.1	Wheel speed sensor comparison (Modified from Zhao, 1997) .....	15
Table 2.2	Gyro comparison (Zhao, 1997).....	24
Table 2.3	Advantages and disadvantages of signpost technology .....	38
Table 4.1	Kalman filter parameters .....	71
Table 5.1	KVH E-Core 1000 Fiber Optic Gyro specifications.....	74
Table 5.2	Technical specifications for G8 receiver .....	77
Table 5.3	Results of the open area Test .....	94

## List of Figures

Figure 1.1 Mobile traffic surveillance (Rabie et al., 2003).....	2
Figure 1.2 Interaction between the four objectives of the main project (El-Rabbany et al., 2000) .....	3
Figure 1.3 System structure of sensor constraint GPS navigation system (Hayashi 1996)6	
Figure 1.4 Integrated DR/DGPS Implementation Functional Flow (Rogers, 2000) .....	7
Figure 1.5 PortaNav Map-Aided GPS Navigation System from (Bullock, 1995).....	8
Figure 1.6 DR, GPS, and Signpost integrated system (suggested system).....	9
Figure 2.1 Dead Reckoning concept.....	13
Figure 2.2 Odometer concept and interface .....	14
Figure 2.3 Variable reluctance position sensors .....	16
Figure 2.4 A schematic diagram of a Hall-effect sensor .....	18
Figure 2.5 Circuit diagrams of linear (A) and threshold (B) Hall-effect sensors (Fraden, 1997) .....	19
Figure 2.6 G&S Digital Hall-effect sensors (G&S, 1998).....	19
Figure 2.7 Electromagnetic proximity sensor.....	21
Figure 2.8 Geometry of differential odometry.....	23
Figure 2.9 Mechanical gyros with a single degree-of-freedom (Lawrence, 1998).....	25
Figure 2.10 Vibratory gyros and its concept.....	27
Figure 2.11 Two-beam interferometer using the fiber optic technology .....	30
Figure 2.12 Concept of Ring Laser Gyro.....	32
Figure 2.13 Ring Laser Gyro responses for input angular rate.....	33
Figure 2.14 FOG Electrical and Optical Circuits (Bennett et al., 1998).....	34
Figure 2.15 Sagnac interferometer responses for open loop configuration (Bennett et al., 1998) .....	36
Figure 2.16 Signpost System .....	37
Figure 2.17 Narrow focus beacons and Wide focus beacons .....	39
Figure 2.18 Block diagram of transmitter electronics for a signpost (Drane and Rizos, 1997) .....	41
Figure 2.19 Block diagram of receiver electronics for a signpost (Drane and Rizos, 1997) .....	42
Figure 3.1 GPS constellation System (from El-Rabbany, 2002).....	44
Figure 3.2 Pseudorange measurement .....	47
Figure 3.3 Multipath effect .....	51
Figure 4.1 Feed-forward aiding system .....	57
Figure 4.2 Feed-back aiding system (Extended Kalman Filter).....	57
Figure 4.3 Transformation from Navigation frame to Geographic frame .....	59
Figure 4.4 Kalman filter loop.....	63
Figure 4.5 Scale factor model.....	66
Figure 4.6 Gyro output without any external rotation .....	67
Figure 4.7 Auto-correlation function for Gyro .....	68
Figure 4.8 Azimuth and gyro drift error .....	68
Figure 5.1 E-Core 1000 Fiber Optic Gyro (KVH™ RD1100).....	74
Figure 5.2 DR Wiring Diagram .....	77
Figure 5.3 G8 OEM board and Housing (Magellan Corp., 1998).....	77

Figure 5.4 The integrated system architecture.....	78
Figure 5.5 Flowchart diagram of the integrated positioning system .....	80
Figure 5.6 Actual trajectory of test and bus stop location .....	81
Figure 5.7 Number of Satellites observed during Test One.....	82
Figure 5.8 HDOP during Test One .....	83
Figure 5.9 Azimuth angle during Test One .....	83
Figure 5.10 DR System with known initial azimuth and start point (Test One) .....	84
Figure 5.11 Solution of DR System alone (Test One).....	85
Figure 5.12 The DR/Signpost solution (Test One).....	86
Figure 5.13 The DR/Signpost errors (Test One).....	86
Figure 5.14 GPS/DR/Signpost integrated system (Test One).....	87
Figure 5.15 DR system alone (Test Two).....	88
Figure 5.16 DR System with known initial azimuth and start point (Test Two).....	89
Figure 5.17 The DR/Signpost solution (Test Two) .....	90
Figure 5.18 The DR/signpost system errors (Test Two).....	90
Figure 5.19 DR/ GPS error for 100 seconds GPS outages (Test Two).....	91
Figure 5.20 DR/GPS/Signpost for 100 seconds GPS outages (Test Two) .....	92
Figure 5.21 GPS/DR/Signpost error for 100 seconds GPS outages (Test Two) .....	93
Figure 5.22 Number of Satellite during Downtown Test .....	95
Figure 5.23 DR System alone (Downtown Test).....	96
Figure 5.24 DR/signpost solution (Downtown Test).....	96
Figure 5.25 DR/GPS solution (Downtown Test).....	97
Figure 5.26 GPS solution when the number of satellites is 4 or more (Downtown Test).....	98
Figure 5.27 GPS/DR/SP integrated system (Downtown Test).....	99

## Notation

### Symbols

$\psi$	Azimuth angle measured from the north direction
$\omega$	Rotation rate
$\rho$	True range from satellite to receiver
$\mu$	Magnetic permeability
$\xi$	Conductivity of the object material
$\delta$	The effective depth of the object
$\alpha$	Angular acceleration
$\lambda$	Carrier-phase wave length (m)
$\Phi$	Carrier-phase observation (m)
$\phi$	Geodetic latitude
$\lambda$	Geodetic longitude
$\delta\psi$	Error in azimuth
$\varepsilon_\Phi$	Carrier-phase measurement noise (m)
$\Delta d_i$	The inner wheel traveled distance
$\Delta d_o$	The outer wheel traveled distance
$\phi_m$	Average latitude
$\varepsilon_p$	Pseudorange measurement noise (m)
$\delta_r$	Receiver clock error
$\delta^s$	Satellite clock error
$a_{cor}$	Coriolis acceleration

$B$	Magnetic field
$c$	Speed of light
$C$	Moment of inertia about the spin axis
$d_\rho$	Orbital error
$d_{fog}$	FOG rate measurements drift
$d^{ion}$	Error due to ionospheric effect
$d_m$	Multipath effect
$dM_f/dt$	Rate of change in the magnetic flux in webers per seconds
$d^{trop}$	Error due to Tropospheric effect
$E_v$	Satellite elevation angle
$f$	Frequency (cycle/s)
$F$	Dynamic matrix
$F_e$	Electromagnetic force
$F_H$	Transverse force on the moving charge carries
$G$	Noise shaping filter
$H$	Design matrix which relates the measurements to the unknowns
$I$	Inertia of Gyro
$K$	Kalman gain matrix
$K_s$	Sagnac scale factor
$N$	Number of loops of Fiber Optic Gyro coil
$N$	Ambiguity parameter
$n$	Refraction index

$N^{Trop}$	Refractivity
$PR$	GPS pseudorange measurement
$q$	Spectral density for individual states
$Q$	Process noise matrix
$R$	Measurements covariance matrix
$R_M$	Meridian radius
$R_N$	Prime vertical radius
$SF$	Scale factor
$T$	Applied torque
$v$	Electric current flow
$W$	White noise
$Z$	Vector of measurements

### Acronyms

APTS	Advanced Public Transportation Systems
AS	Anti-Spoofing
C/A	Coarse acquisition code
DGPS	Differential GPS
DoD	Department of Defense
DR	Dead Reckoning
EKF	Extended Kalman filter
FOG	Fiber Optic Gyro
GDOP	Geometric Dilution Of Precision



GPS	Global Positioning System
HDOP	Horizontal Dilution of Precision
IFOG	Interferometric Fiber Optic Gyro
IGS	International GPS Service
ITS	Intelligent Transportation System
KF	Kalman Filtering
L1	Civilian GPS frequency 1575.42 MHz
L2	Military GPS frequency 1227.6 MHz
PRN	Pseudo random noise code
RLG	Ring Laser Gyro
SA	Selective Availability
SNR	Signal to Noise Ratio
TEC	Total electronic content
TTC	Toronto Transit Commission
UHF	Ultra High Frequency
WGS84	World Geodetic System 84

# **CHAPTER 1**

## **INTRODUCTION**

Transit system authorities in many countries are facing a challenging trend of financial constraints that limits their capabilities to expand existing services and to increase the ridership. The Toronto Transit Commission (TTC) is no exception. To improve the operational efficiency of the Toronto transit system, the TTC is exploring a number of new technologies, centering on the implementation of Intelligent Transportation Systems (ITS). The ITS technologies explored include the transit vehicle priority at signalized intersections and the use of a mobile bus-mounted machine vision system for transit and traffic monitoring, among others (Greenough and Noehammer, 1999; Rabie et al., 2003). A key element to a successful ITS implementation, however, is the availability of reliable real time vehicle location information.

To enhance the operational efficiency of the TTC system, a multidisciplinary research project was carried out by a team of researchers from Ryerson University and the University of Toronto. The research project was concerned with one area of Intelligent Transportation Systems (ITS), namely the Advanced Public Transportation Systems (APTS) (Shalaby et al., 2002). The project had four distinct, albeit linked, objectives. First, it aimed to improve the accuracy and reliability of real time bus location using an integrated GPS/DR/Signpost system. The second objective was to develop a binocular machine vision system, mounted on buses in an urban corridor, to dynamically monitor traffic conditions along the corridor. In contrast to earlier machine vision technologies used for traffic management, which relied mainly on fixed point detection and simpler

algorithms to detect certain traffic characteristics, the new approach uses a recent trend in computer vision research, namely, the active vision paradigm (Figure 1.1). The third objective of this research was to develop a passenger information system for the provision of real time bus arrival times at bus stops, using information on real time bus location and real time scheduling. Finally, the fourth objective of the research project was to develop a model and an algorithm for real time scheduling based on real time bus location, traffic conditions, and expected arrival times at bus stops. Figure 1.2 shows how the four objectives are linked together.

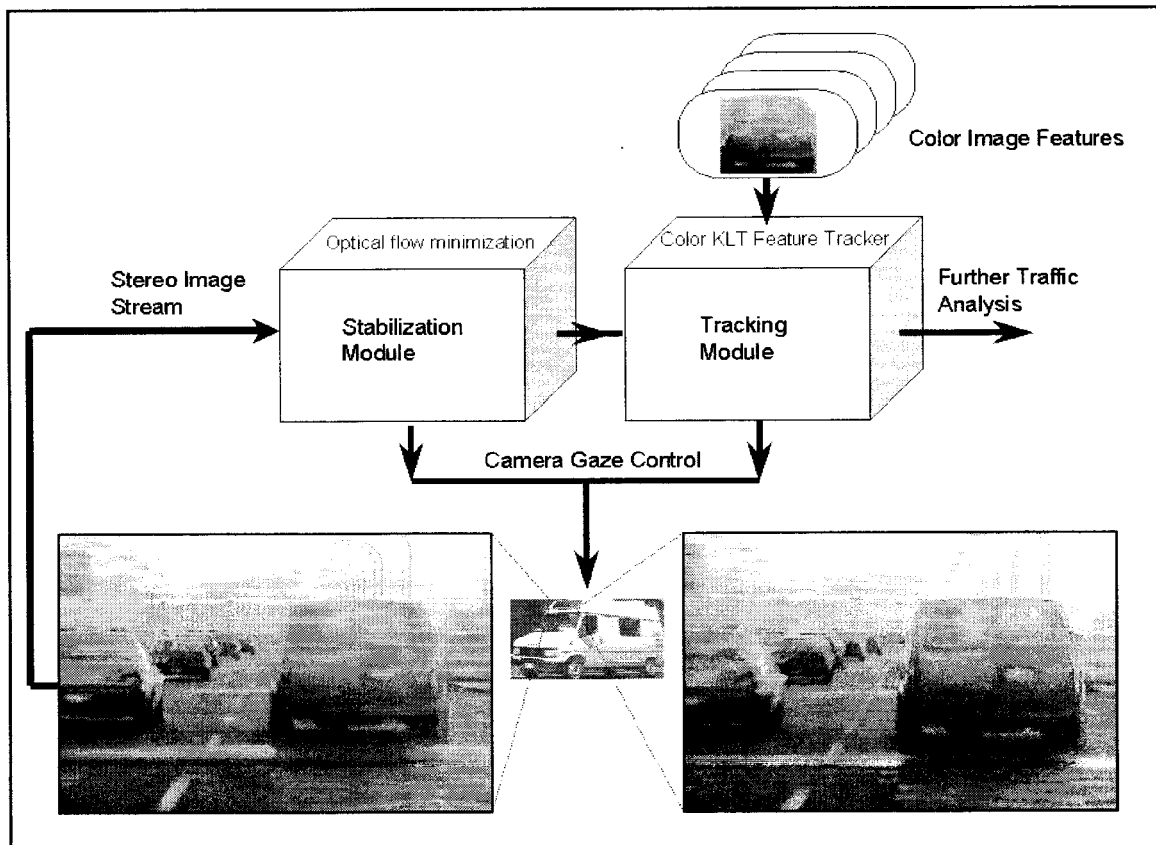


Figure 1.1 Mobile traffic surveillance (Rabie et al., 2003)

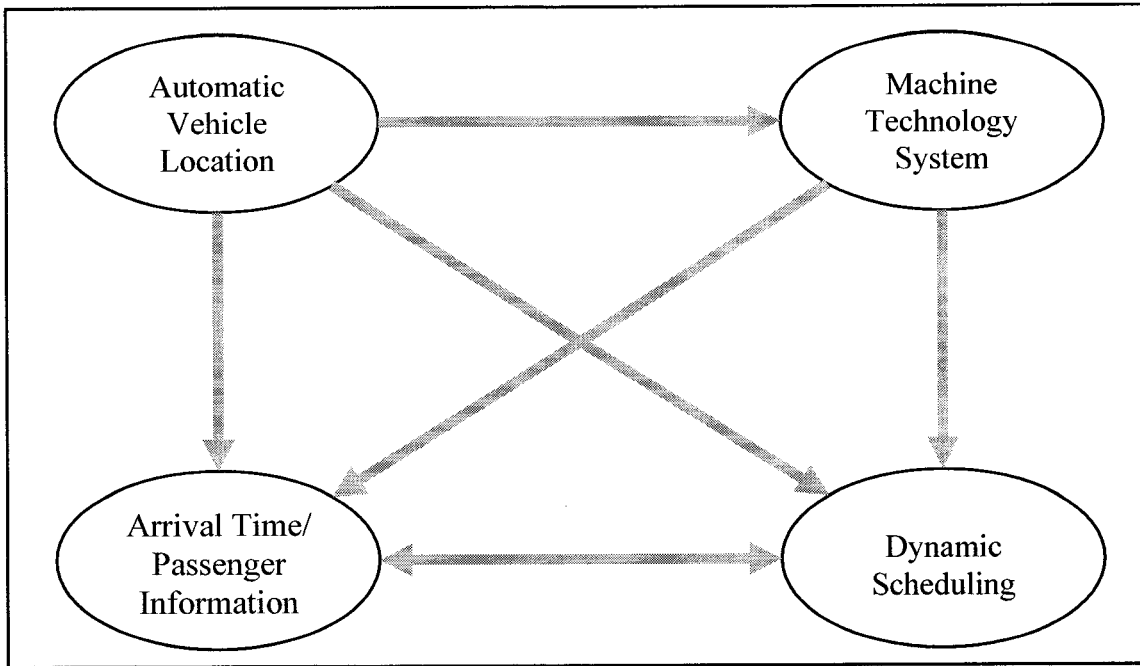


Figure 1.2 Interaction between the four objectives of the main project (El-Rabbany et al., 2000)

### 1.1 STATEMENT OF THE PROBLEM

The Toronto Transit Commission operates nearly 1500 buses; all are equipped with DR systems that are used to locate the buses in real time by combining the measurements from the odometer and the gyro, the bus's position can be determined with respect to an initial (known) position (El-Rabbany et al., 2000). In addition, a total of 730 radio beacon transmitters (signposts) are placed at known locations along the bus routes to compensate for the drift of the DR systems (Pekilis and Heti, 1992). The real time positions of the buses are sent to the control center via communication links and are displayed on a base map.

TTC is currently utilizing a two-way radio system that operates on the UHF 420-430 MHz, spaced in half channels at 15.5 KHz (a total of 42 channels are available). Of the

42 channels, 31 are used for data transmission, while the remaining 11 channels are used for voice communication (El-Rabbany et al., 2000). The system is built as a custom-designed, integrated communications system network. Unfortunately, the current positioning and communication systems suffer from accuracy and/or reliability limitations. This accuracy limitation is caused by the current system biases and drifts. The DR system gives accurate heading and distance measurements for a short time, but gyro and odometer errors accumulate after a while and navigation errors grow.

Generally, these errors can be defined very well, but their contribution to positioning accuracy is not a trivial task, as they are complex and nonlinear (Drane and Rizos, 1997). In fact, the propagation of the DR error into position error is different since the DR sensor errors grow with time or distance from the initial calibration or update. For two-dimensional positioning problems, DR sensors are mostly of two kinds: direction (or rate of direction change) sensors, such as compasses and gyros; and distance sensors, such as odometers. Errors in direction sensors grow with time, but error in the distance sensor is a function of distance traveled.

Furthermore, the signpost system has some limitations. Since it is a discrete positioning system in the spatial domain, it depends on the distances between two successive. In addition, it is not possible to track a bus that goes off-route, as a result of, for example, road closure (El-Rabbany and Abd El-Gelil, 2003).

## **1.2 LITERATURE REVIEW**

It has become common, since low-cost and reliable positioning sensors are being introduced, to combine GPS with other positioning sensors to enhance navigation capability in the absence of GPS signals (Barbour and Schmidt 2001; Borenstein 1998).

There is a lot of research work in the area of integrated systems with different kinds of sensors.

Hayashi (1996) developed an integrated system combining a differential GPS, a barometer, and a gyro (Figure 1.3). The suggested system is a portable one with no direct attachment to the vehicle. A new navigation concept called Sensor Constraint GPS navigation was applied in Hayashi's research. It employed a barometric pressure transducer and a fiber optic gyro in addition to GPS unit. The vertical and horizontal displacements are constrained according to the sensor information. This concept increased the position availability in urban area since two GPS satellites were enough for position solution. Furthermore, this augmented system can be used to detect the solution that contains a multipath error by monitoring the large GPS range residuals or by knowing the vehicle dynamic model. A decentralized Kalman filter was applied for sensors measurements where every individual sensor had its own filter. Finally, the augmented least squares and Kalman position estimators were chosen for a constrained position solution. In his recommendations, Hayashi (1996) suggested that the number of satellites needed for positioning could be reduced to only one satellite by adding another sensor to estimate, e.g., receiver clock offset. Zhang (1997) used the same sensors and techniques used in Hayashi's research, but added a rubidium clock to estimate the receiver clock offset. Three satellites were enough to fix the vehicle location with the added clock. However, the positioning accuracy and the navigation availability were improved significantly when the three sensors were used together. In fact, adding more sensors with suitable models improves the navigation solution.

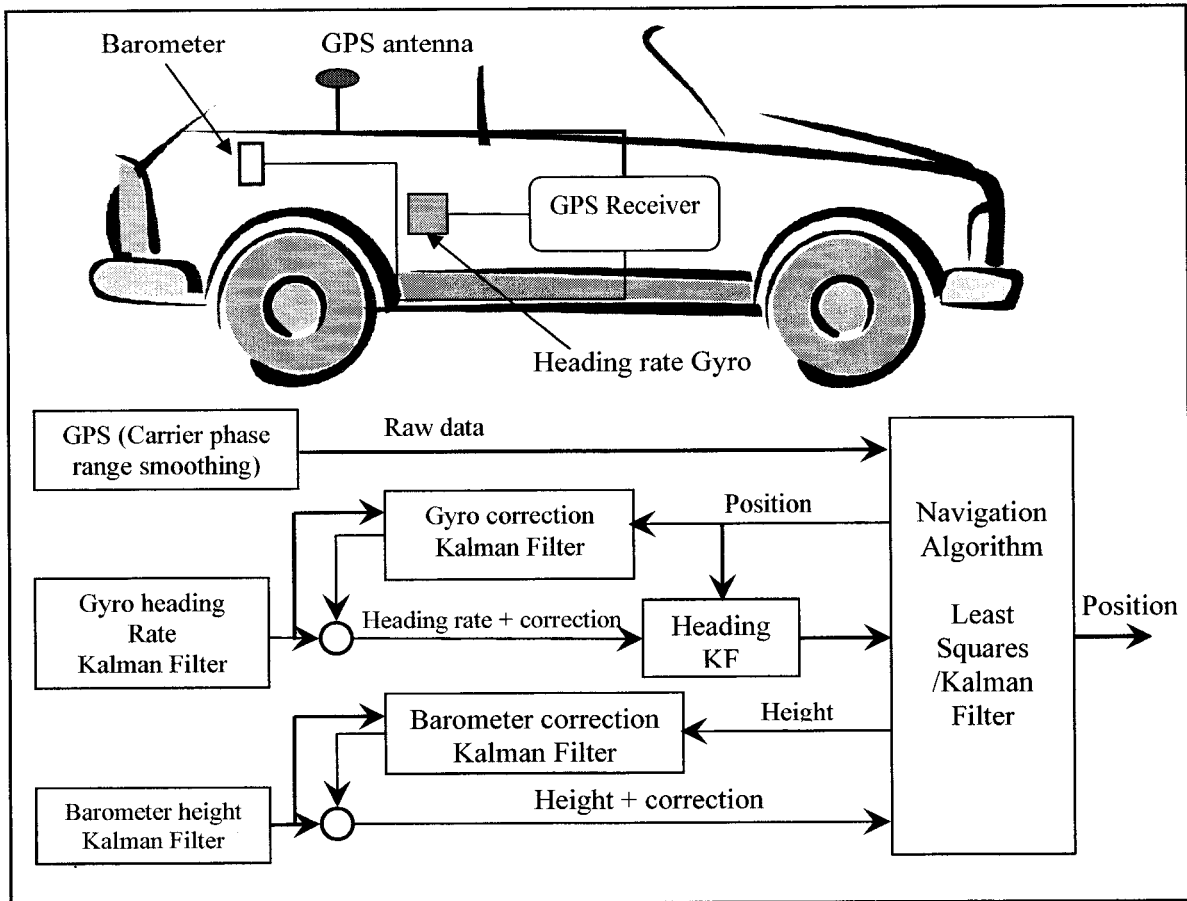


Figure 1.3 System structure of sensor constraint GPS navigation system (Hayashi 1996)

Rogers (2000) used the same aiding system mentioned above but, instead of using barometer, a radar ground speed sensor was installed to measure the traveled distance (Figure 1.4). The results from this work were presented in real time using Kalman filtering technique with five states parameters. Differential odometer and vibrating gyro for heading and inclinometer were used by Stephen and Lachapelle (2000). Since each odometer measures distances traveled by one wheel only, two are required for differential odometry, which gives redundant heading measurements. Inclinometer was used to measure pitch and roll angles so that gyro reading could be corrected. Zickel and Nehemia (1994) used GPS as an aiding system for DR sensors (digital odometer and

compass). In the open area, the GPS was the main positioning system, but when the GPS signals were blocked for any reason, the DR was working as the main positioning system.

To increase the number of visible satellites in the urban areas, Tsakiri et al. (1999) suggested integration between GPS/DR systems and GLONASS. They used two receivers: one for GPS signals and the other for GLONASS signals. The results showed that GPS positioning solutions can be obtained 75% of the time in downtown, but with GPS/GLONASS integrated, this percentage improved to 85%. During GPS/GLONASS outages, DR provides an adequate bridge.

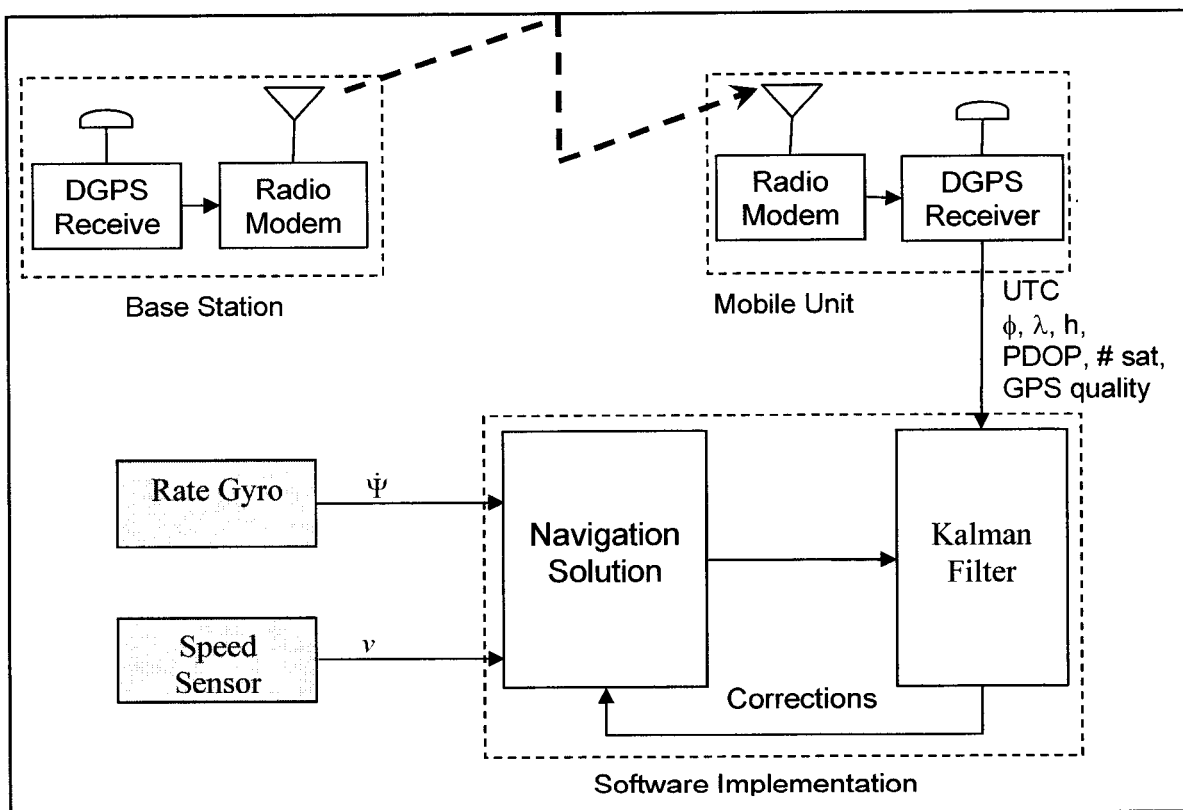


Figure 1.4 Integrated DR/DGPS Implementation Functional Flow (Rogers, 2000)



In addition to hardware aiding systems, map matching was investigated by many researchers. Harris (1989) employed the differential odometer theory with a map database component and GPS. Differential odometry gives heading information, as mentioned earlier, so there was no need for another heading sensor. In Harris's research, map matching and DR were used to update position when GPS signals were masked. Ishikawa et al. (1995) utilized map matching technology in addition to odometer, fiber optic gyro, and GPS receiver to enhance positioning accuracy. They used the fiber optic gyro readings to smooth the vehicle trajectory, which happens when the vehicle goes through a straight road. Bullock (1995) did not use any DR components at all; only map aiding and GPS were used. The system was designed to be a portable land navigation system (Figure 1.5). Etak digital road map was selected, together with a Trimble Mobile GPS and a PCMCIA card-type GPS receiver, and the portaNAV map-aided GPS navigation system was created.

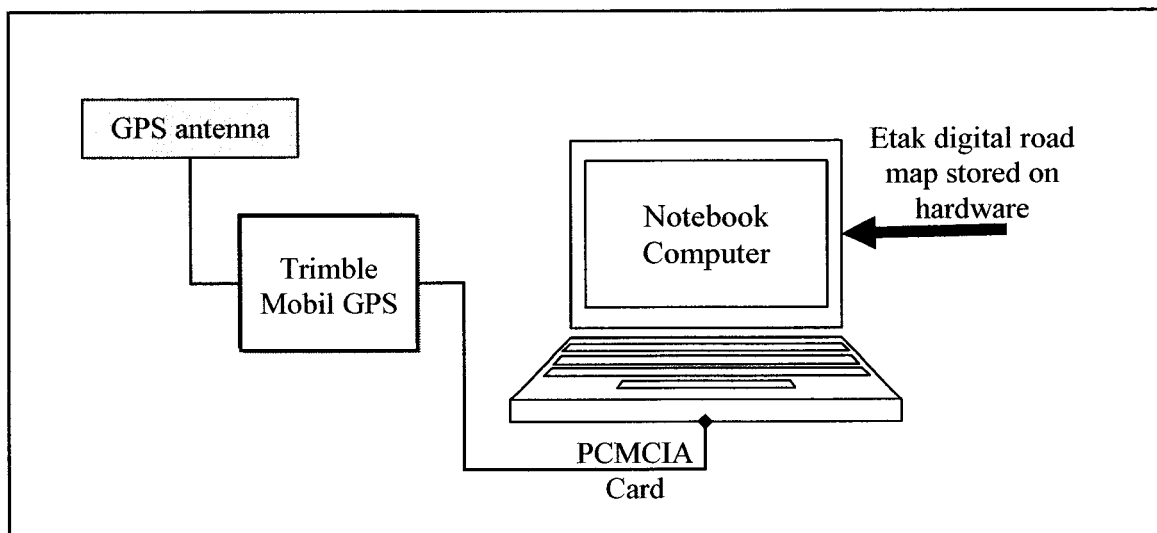


Figure 1.5 PortaNav Map-Aided GPS Navigation System from (Bullock, 1995)

### 1.3 THESIS OBJECTIVES

This thesis develops the first component of the project, namely the integrated positioning system (Shalaby et al., 2002). The proposed integrated system consists of a low-cost, autonomous GPS system, supplemented by the existing DR/signpost system. Figure 1.6 illustrates the suggested system. The augmentation of GPS with various sensors not only overcomes performance issues found in each individual sensor, but also produces an integrated system whose performance exceeds that of the individual sensors (Kaplan, 1996). With this integrated system, GPS helps in controlling the drift of the DR system using frequent calibration, while the DR becomes the main positioning system during the GPS outages. An optimal positioning solution is obtained using Kalman filtering technique, which fuses and utilizes all the available sensor information.

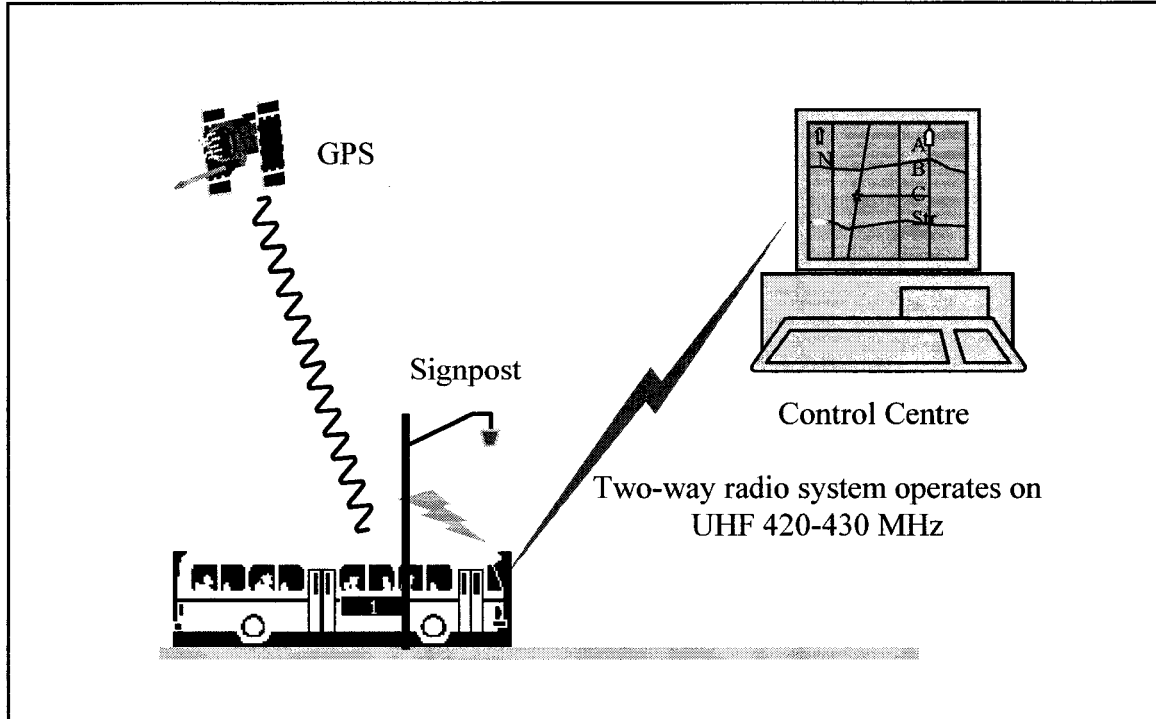


Figure 1.6 DR, GPS, and Signpost integrated system (suggested system)

The suggested integrated system has many advantages over previously developed systems. It is accurate as the signposts are considered as reference stations, and GPS has long term stability. Moreover, it is lower in cost, as it uses the already existing infrastructure (i.e. signpost) and wheel sensors which is already installed in all buses and vehicles.

#### **1.4 CONTRIBUTION OF THE RESEARCH**

The contribution of this research can be summarized as follows:

1. To evaluate the performance of the existing conventional system (i.e., DR and signpost systems);
2. To examine the effect of signpost distribution and location;
3. To develop algorithms and software for a low-cost integrated positioning system, which combines GPS with the existing conventional systems (DR and signpost).
4. To demonstrate the applicability of the developed system methodology using field data.

#### **1.5 THESIS OUTLINE**

Chapter 2 gives details of the conventional technology used for positioning, namely the DR and the signpost systems. The transmission sensors and their technologies are presented, followed by the direction sensors, each of which is discussed in detail with its advantages and disadvantages. This chapter ends with the signpost components.

Chapter 3 introduces the Global Positioning System (GPS), starting with an overview of the system architecture as developed by United States Department of Defense (DoD).

The GPS pseudorange measurement is defined, along with its measurement equations. Discussion of GPS error sources concludes this chapter.

Chapter 4 presents the methodologies used and its implementation including different aiding systems and Kalman filtering technique. Field test results for both open areas and masked areas are presented and the navigation performance of the individual system and the integrated system are evaluated.

Chapter 5 describes the integrated system, the practical tests, and data analysis.

Chapter 6 presents the conclusions and recommendations based on this research.

## CHAPTER 2

### CONVENTIONAL POSITIONING SYSTEMS

DR sensors, among the oldest navigation technologies, measure distance and direction from a fixed point. These sensors are still found on many fleets and buses as a secondary sensor. DR sensor is self-contained within the vehicle; this means that no infrastructure is required for its operation. Since the DR is presently the main positioning system for TTC bus location, this chapter presents its main concept and the different technologies for distance sensors and directional sensors. The last section illustrates the signpost components and concepts.

#### 2.1 DEAD RECKONING

DR navigation is the process of determining a vehicle's location at different time intervals relative to an initial point by integrating measured distance increments and headings of travel. Usually, a curvilinear route is approximated by a sequence of connected vectors in a linear, piecewise mode (Figure 2.1). The vehicle position at any particular epoch  $n$  can be defined by:

$$x_n = x_0 + \sum_{i=1}^n \Delta \ell_i \sin \psi_i \quad (2.1)$$

$$y_n = y_0 + \sum_{i=1}^n \Delta \ell_i \cos \psi_i \quad (2.2)$$

where  $(x_0, y_0)$  is the initial vehicle position at time  $t_0$ ,  $\Delta \ell_i$  is the traveled distance or the magnitude of the displacement between time  $t_{n-1}$  and time  $t_n$ , and  $\psi$  is the azimuth angle.

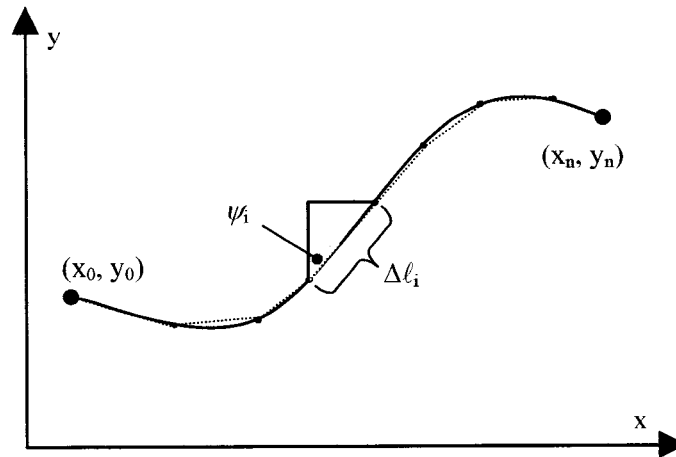


Figure 2.1 Dead Reckoning concept

From a historical point of view, most DR sensors that are used in automobile navigation were developed long before the automobile navigation itself. These include the odometer, the magnetic compass, and the gyrocompass. However, the gyrocompass, developed in 1906, has limited use in automobile navigation systems (French, 1986). Nowadays, the market for automatic vehicle location offers many sensors that can be used as DR subsystems within the positioning system, including odometers, speedometers, altimeters, barometers, inclinometers, magnetic compasses, and gyros. All of these sensors have limitations. Even the most precise DR systems require periodic re-initialization and frequent calibration.

### 2.1.1 Distance Sensors

An odometer is used to measure the distance traveled by the vehicle or, specifically, by individual wheels. Most vehicles have a transmission-based odometer to record the traveled distance. This device is installed by the vehicle's manufacturer, mainly to evaluate the vehicle's age and to give an indication about periods of maintenance. Odometers are electronic devices that generate an integer number of digital pulses each

time a tire on the vehicle makes one revolution (Figure 2.2). Scale factor is used to convert the number of pulses counted by the odometer within a specified time interval to the distance traveled by the vehicle (Abbott, 1999).

The odometer scale factor is not a constant value since it depends on the radius of the vehicle's tire. The tire's radius changes with its pressure, temperature, and the vehicle's speed. The reasons for the scale factor variation are discussed in details in Zickel and Nehemia (1994).

In addition to the odometer scale factor varying error, the output of an odometer contains random errors. These errors arise because the output of the odometer is a pulse train, implying that distances measured by the odometer are quantized into packets represented by the single pulse. Therefore, measured distances cannot be resolved more accurately than the distance corresponding to only one pulse. Abbott (1999) suggested that quantization error can be treated as white noise.

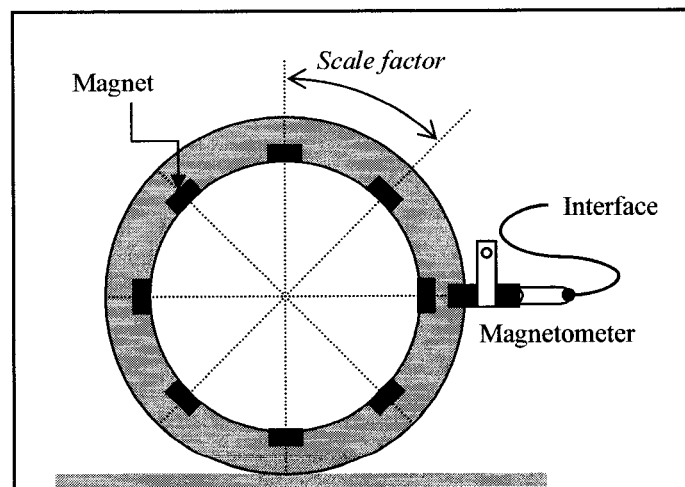


Figure 2.2 Odometer concept and interface

There are different technologies used to convert the wheel shaft mechanical motion to electronic signals. The most widely used sensors are the magnetic sensors that depend on the magnetic field, such as variable reluctance, Hall-effect sensors, and reed switches sensors. For the sake of completeness, several types of sensor mechanics are presented in the next subsections. Table 2.1 illustrates different types of distance sensors.

Table 2.1 Wheel speed sensor comparison (Modified from Zhao, 1997)

Sensor	Frequency range	Magnet	Ferrous wheel	SNR
Variable-Reluctance	1-100 KHz	Yes	Yes	Low
Hall-Effect	0-1 MHz	Yes	Yes	Moderate
Optical	0-10 MHz	No	No	Very High
Eddy current	0-500 KHz	No	No	High

#### 2.1.1.1 Variable Reluctance Sensor

A variable reluctance sensor is an electromagnetic device consisting of a permanent magnet surrounded by a winding of wire. The sensor is used in conjunction with a ferrous target wheel that has either notches or teeth (Figure 2.3). According to Faraday's Law, if a coil is perpendicular to a varying magnetic field, a current (or voltage) is created in the coil. This current (voltage) is proportional to the electromagnetic force generated in the coil, and the electromagnetic force is proportional to rate of change in the magnetic flux:

$$F_e = -\frac{dM_f}{dt} \quad (2.3)$$

where  $dM_f/dt$  is the rate of change in the magnetic flux in webers per second, and  $F_e$  is the electromagnetic force in volts.



Rotation of the target wheel near the tip of the sensor changes the magnetic flux, creating an analog voltage signal in the sensor coil. When a tooth on the ferrous wheel begins to pass between the magnet poles, the coil voltage starts increasing from zero, reaches a maximum, and falls to zero again. To complete a full sine wave, the voltage starts to increase until it reaches the maximum value in the opposite direction. As a result, sensor accuracy increases as the number of tabs around the shaft increase.

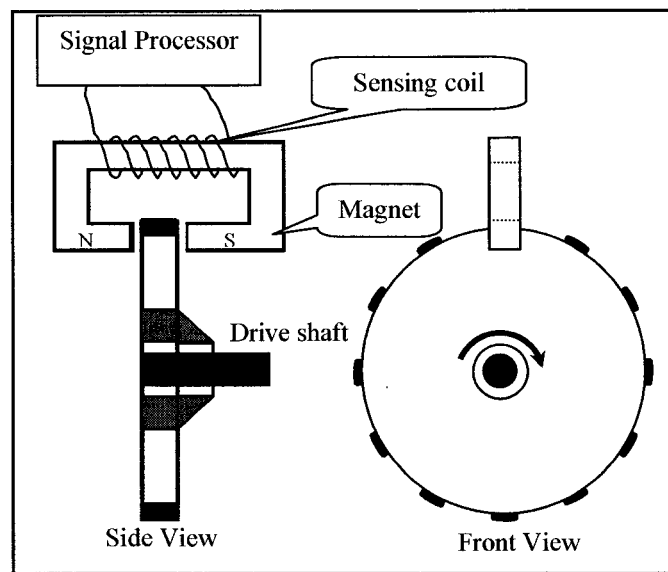


Figure 2.3 Variable reluctance position sensors

In spite of their simple construction and low-cost, variable reluctance sensors have some shortcomings. If the vehicle's speed is very low, the shaft rotates slowly and a very weak signal is produced. In this case, the cut-off speed for this sensor is identified as the speed at which the sensor no longer processes any signal. Second, it is difficult to output a constant voltage envelope. The voltage level and frequency change as the speed of the ferrous wheel changes. Third, the Signal to Noise Ratio (SNR) is corrupted by the vibrations or resonance. In high speeds, the output range of this sensor tends to flatten (Zhao, 1997).

### 2.1.1.2 Hall-Effect Sensor

The Hall-effect sensor has been known for more than one hundred years, named after E. H. Hall, who discovered it in 1879, it has been put to visible use only in the last three decades (Fraden, 1997). Its first practical application (outside of laboratory experiments) was in the 1950s as a microwave power sensor. Currently, the Hall-effect sensors are used to detect the magnetic fields, positions, and displacement of objects. The Hall-effect occurs when an electric current ( $v$ ) flows through a conductor in a magnetic field ( $B$ ); the magnetic field exerts a transverse force ( $F_H$ ) on the moving charge carriers, which tends to drag them to conductor's corner. This force can be defined as follows (Fraden, 1997):

$$F_H = qvB \quad (2.4)$$

$F_H$  is perpendicular to the  $v$  and  $B$  plane. This force is most evident in a thin, flat conductor, as illustrated in Figure 2.4. A buildup of charge at the sides of the conductors balances this magnetic influence, producing a measurable voltage,  $V_H$ , between the two sides of the conductor.

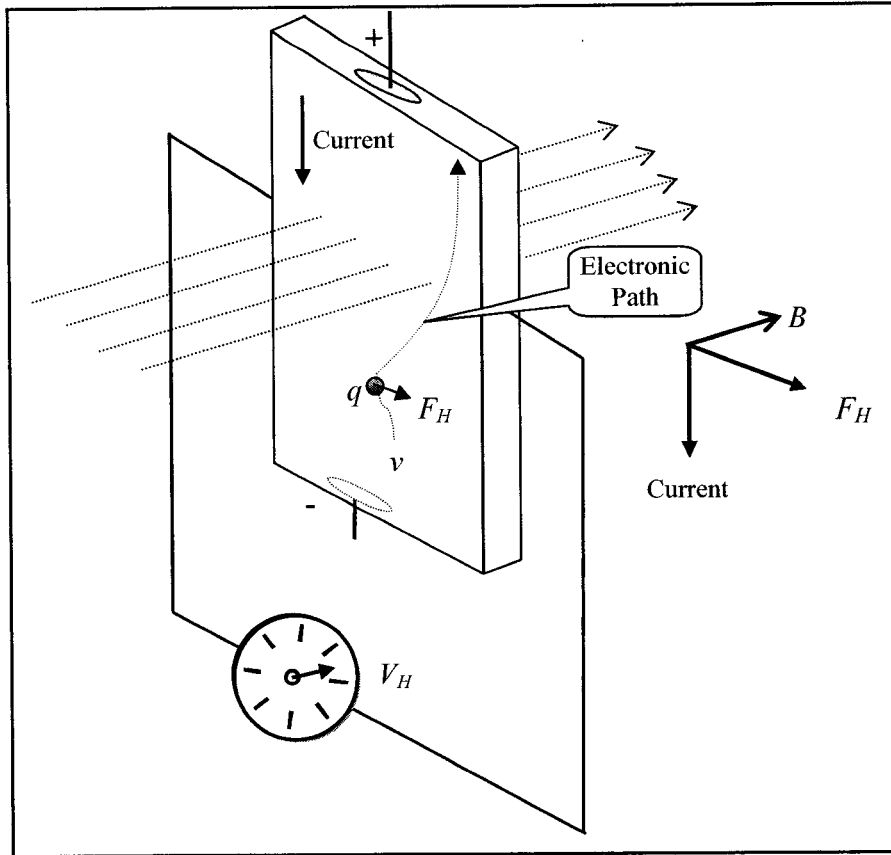


Figure 2.4 A schematic diagram of a Hall-effect sensor

In fact, the Hall-effect sensors are usually fabricated as monolithic silicon chips and encapsulated into small epoxy or ceramic packages. There are two types of Hall-effect sensors (Figure 2.5): linear and threshold. A linear sensor usually includes an amplifier for an easier interface with the peripheral circuits. The threshold sensors, in addition to an amplifier, contain a Schmitt trigger detector with built-in hysteresis (Fraden, 1997). These sensors are preferable to a variable reluctance sensor, since they do not have a dead-band. This allows sensing of lower wheel speeds. In addition, the analog signals generated from this sensor are proportional to the magnetic field strength over the sensor. As well, this sensor is more accurate, since it can measure the sine wave phase in a way that is more accurate than counting full cycles (Stephen, 2000). A classical Hall-effect

digital speed sensor is shown in Figure 2.6, in which the naturally occurring sinusoidal signal is squared up as a digital pulse train.

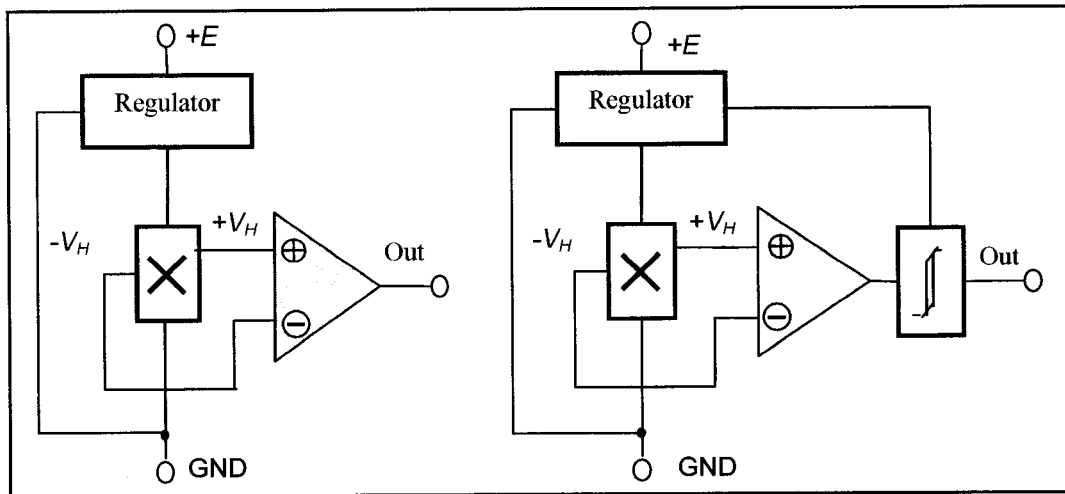


Figure 2.5 Circuit diagrams of linear (A) and threshold (B) Hall-effect sensors (Fraden, 1997)

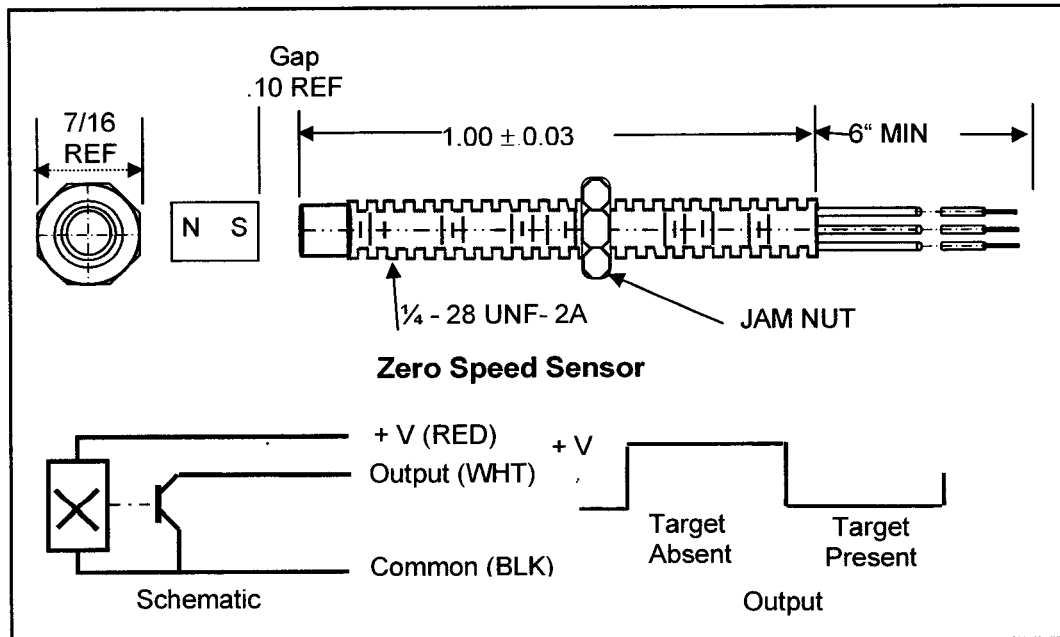


Figure 2.6 G&S Digital Hall-effect sensors (G&S, 1998)

Sensors that use Hall-effect are not the preeminent ones. Despite their precision, they have some limitations. Their response is sensitive to the upper and lower limits of operating temperature. This response degrades as the temperature approaches these limits; furthermore, they cannot be used in temperatures lower than -40 °C or higher than 65.6 °C (Zhao, 1997). Careful alignment and mounting are needed when setting up these sensors, since they are sensitive to the gap size between sensor and disk.

#### *2.1.1.3 Eddy Current Sensors*

An eddy current is a local electric current induced in a conductive material by the magnetic field produced by the active coil. A dual-coil is used, one as a reference and the other for sensing the magnetic current induced in the active object (Figure 2.7). This local electric current, in turn, induces a magnetic field opposite to the one from the active coil, resulting in a disbalance with respect to the reference coil. The distance between the object and the sensor coil is very important; the closer the object is to the coil, the larger the change will be in the magnetic impedance. The effective depth of the object ( $\delta$ ) where eddy current is produced is given by (Fraden, 1997):

$$\delta = \frac{1}{\sqrt{\pi f \mu \xi}} \quad (2.5)$$

where  $f$  is the excitation frequency of the circuit,  $\mu$  is the magnetic permeability of the object material, and  $\xi$  is the conductivity of the object material.

For effective operation, the object material must be larger than the effective depth of the eddy current to make the transducer successful. This is because the transducer assumes that the eddy current is localized near the surface of a semi-infinite solid, and the actual

eddy current amplitude decreases quadratic with distance. Generally, the relationship between the coil impedance and the distance to the object  $x$  is nonlinear and temperature dependent (Fraden, 1997).

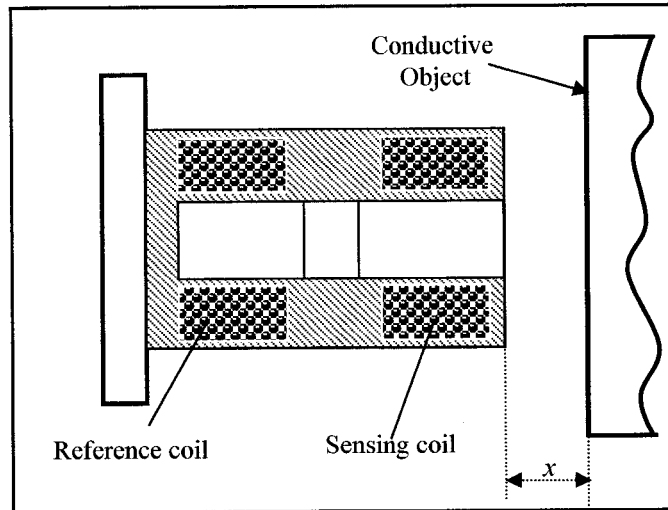


Figure 2.7 Electromagnetic proximity sensor

#### 2.1.1.4 Optical Sensors

There is a large variety of optical sensors available for measuring the rotation of the wheel shaft. Most sensors use a visible or infrared laser beam to project a spot of light onto a target, which is then reflected from the nearby surface to the collector. The collector induces an output current that is proportional to the flux of returned light. The signal is reflected from a shaft with a series of tabs surrounding it. A proximity sensor measures the strength of the reflections from the shaft, and adds to the count each time the detection threshold is reached, i.e., when the tabs pass the detector. In other words, an optical sensor usually requires at least three essential components: a light source, a photo-detector, and a light guidance device (Fraden, 1997). The observation is not continuous, as it is for Hall-effect sensors, but is, instead, a discrete count of fractions of a full

rotation. Similar systems pass a continuous signal past the edge of the shaft, and the signal is interrupted by the passing tabs. Electro-Optical Integrated Circuits have become progressively more affordable in recent years, so sensors like this are becoming relatively common.

The optical sensor is sometimes preferable for its simplicity, absence of loading effect, and its long-term stability. Since it works according to optical phenomenon, it is insensitive to stray magnetic fields and electrostatic interferences, which makes it relatively suitable for many applications.

#### *2.1.1.5 Differential Odometry*

Two odometers, one on the right wheel and another on the left wheel, provide the traveled distance and heading change (i.e., change in azimuth) (Harris, 1989). When the vehicle turns, the inner wheel travels a shorter distance  $\Delta d_i$  than the outer wheel  $\Delta d_o$  without slippage (Figure 2.8). Distance traveled over ground by the vehicle is calculated by averaging the two accumulated distances:

$$\Delta d = \frac{\Delta d_i + \Delta d_o}{2} \quad (2.6)$$

The difference between odometry can be used to estimate the heading change  $\Delta\psi$  (Harris, 1989):

$$\Delta\psi = \frac{\Delta d_o - \Delta d_i}{Track\ width} \quad (2.7)$$

where *Track width* is the effective turning width of the car.

The most significant errors for differential odometry are wheel slippage and scale factor error. Stephen (2000) gave a numerical example to demonstrate how the scale factor error affects the azimuth. Also, data rate must be high, especially when the car turns.

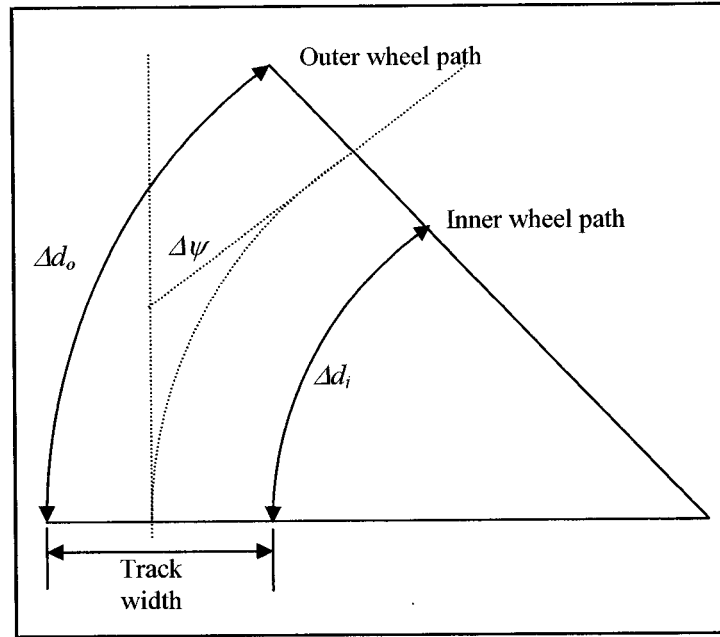


Figure 2.8 Geometry of differential odometry

### 2.1.2 HEADING SENSORS

In many cases, where a geomagnetic field is either absent (in space), or changed by the existence of some disturbances, a gyro is a crucial sensor for defining the attitude of the vehicle (Fraden, 1997). A gyro is also used to measure the relative attitude or orientation as well as absolute direction in a number of applications, including inertial navigation (Jekeli, 2001). Gyros are classified as either gimbaled or strapdown. Gimbaled gyros are maintained with a fixed orientation in an inertial frame, which makes it relatively bulky and with superior performance (El-Sheimy, 2002). However, the strapdown system is preferred for land navigation since it is low in cost and small in size.



Generally, low-cost gyros measure rotation on a fixed plane with respect to the vehicle (body frame), which is not generally on the plane perpendicular to the gravity vector. Therefore, the gyro senses the rotation not only in heading, but also in pitch and roll. For low-cost navigation systems, there is no means to measure the other two components (roll and pitch), so their effects will be ignored. Gyros include mechanical, vibratory, and optical devices. A comparison of these gyro types is presented in Table 2.2.

Table 2.2 Gyro comparison (Zhao, 1997)

Type	Performance	Cost	Size
Mechanical	Very good	Expensive	Large
Vibratory	Good	Cheap	Small
Optical	Very good	Moderate	Moderate

#### 2.1.2.1 Mechanical Gyros

A mechanical gyro is comprised of a massive disk that is free to rotate about a spin axis confined within a framework that is free to rotate about one or two axes (Figure 2.9). Hence, depending on the number of rotating axes, gyros can be either of a single or two degree-of-freedom types (Lawrence, 1998).

When the rotor freely rotates, it tends to maintain its axial position. If the gyro platform rotates around the input axis, the gyro will develop a torque around a perpendicular (inertial axis) axis, thus turning its spin axis around the output axis. This phenomenon is called precession of a gyro. It can be explained by Newton's second law of motion for rotation: the time rate of change of angular momentum about any given axis is equal to

the torque applied about the given axis. That is, the rate of change of angular momentum  $\mathbf{H}$  will equal the applied torque  $T$  about the input axis (Lawrence, 1998):

$$T = \frac{d\mathbf{H}}{dt} = \mathbf{H}\Omega \quad (2.8)$$

where  $\mathbf{H}$  = inertia of gyro  $\times$  angular velocity  $= I\omega$  and  $\Omega$  is the precession rate (the angular velocity of the rotor about the axis normal to the plane of the spin and input torque). However, if the torque acts about the axis of rotation, its effect is to increase the angular velocity:

$$T = C d\omega / dt = C\alpha \quad (2.9)$$

where  $C$  is the moment of inertia about the spin axis and  $\alpha$  is the angular acceleration.

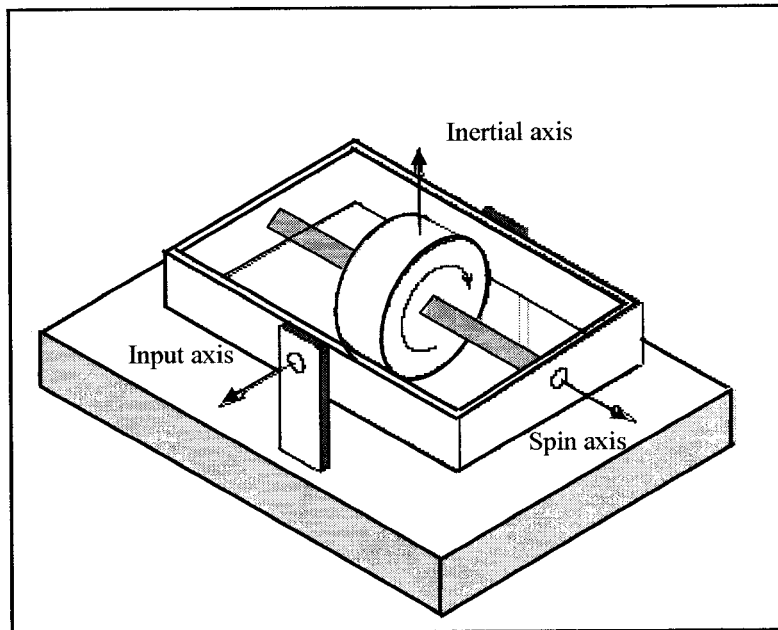


Figure 2.9 Mechanical gyros with a single degree-of-freedom (Lawrence, 1998)

The accuracy of mechanical gyros greatly depends on the effects that may cause additional unwanted torques and cause drifts. There are several sources for unwanted

torques, including friction, imbalanced rotor, and magnetic effect. One method that is generally used to minimize rotor friction eliminates the suspension completely by floating the rotor and the driving motor in a viscous, high-density liquid, such as one of the fluorocarbons (Lawrence, 1998). This method has some limitations as it requires close temperature control of the liquid and also may suffer from aging effects. The other method of friction reduction is to use so-called gas bearings, where the shaft of the rotor is supported by high-pressure helium, hydrogen, or air (Fraden, 1997).

#### *2.1.2.2 Vibratory Gyros*

Vibratory gyros are the less expensive one in the market nowadays. The main reason for that is they have neither wheels nor flotation fluids (Lawrence, 1998). However, they are designed and manufactured in macro scale as well as in micro scale and all of them are physically different but follow the same operating principal. Normally, vibratory gyros are based on the transfer of electrical energy to vibrations and vice versa. These vibration modes are caused by Coriolis acceleration (Yazdi et al., 1998).

Coriolis acceleration is caused by Coriolis force which is a fictitious force exerted on a body when it moves in a rotating reference frame (Figure 2.10). To understand the Coriolis effect, Yazdi et al. (1998) simplified this concept as shown in Figure 2.10. Assume there is an observer sitting on the x-axis of the xyz coordinate system and watching a moving particle in the y direction with velocity  $v$ . If the coordinate system along with the observer starts rotating around the z-axis with an angular velocity  $\Omega$ , the observer thinks that the particle is changing its trajectory toward the x-axis with an acceleration equal to  $2 v \times \Omega$ .

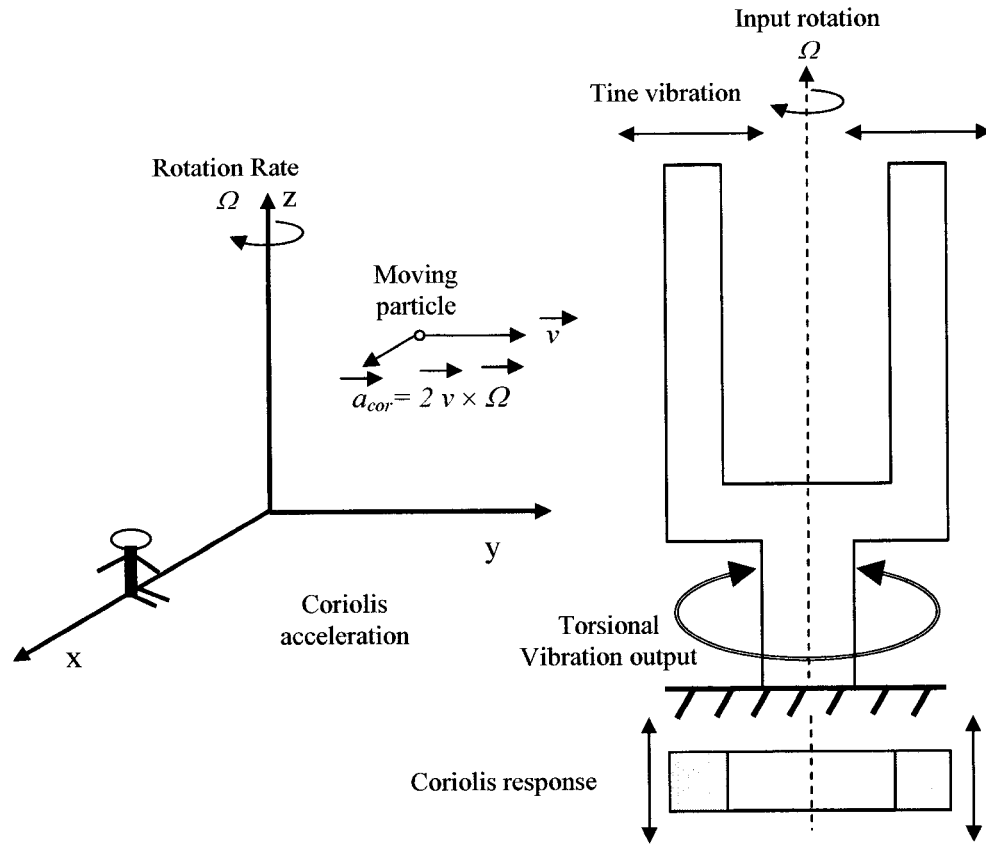


Figure 2.10 Vibratory gyros and its concept

Although there are a number of different commercial vibratory gyros such as tuning forks, vibrating beams, vibrating string, and vibrating shells (Yazdi et al., 1998). The classical one is the tuning forks. As seen from Figure 2.10, it consists of flexural vibration of tines that are connected to a junction bar. For this arrangement, there are two types of motion; the primary motion in the y-direction caused by electrodes deposited onto the sides and the secondary motion as a result of Coriolis acceleration in the x-direction. The secondary motion is detected piezoelectrically by electrodes on the top of tines. Furthermore, the Coriolis force will generate a periodic torque on the junction bar which can be detected by electrodes, too (Burdess et al., 1994).

Vibratory gyros typically reveal certain undesirable behaviors that impede the angular rate measurement accuracy, such as nonlinearity, cross-axis sensitivity, scale factor error, and quadrature error. These errors are result from both the mechanical and electrical components of a gyro.

### 2.1.2.3 Optical Gyros

Optical gyros are based on different sensing principles, being kinematic rather than dynamic. They do not have spinning proof mass like the mechanical gyros that follow Newton's laws of motion. Light waves act as the sensor element in the optical gyro, so there is no need for mass, and there is no effect from the environment in which the gyro is located (e.g., gravity effect). There are two facts about the optical gyro that make it different from other gyros. First, it is not suitable for local-level stabilization since it cannot be torqued or commanded. Second, it has a single degree of freedom, which means that three gyros are needed to measure three angular rates about three axes (Jekeli, 2001).

The physical phenomenon that explains the operation of an optical gyro is known as the Sagnac effect. A simple representation of the Sagnac effect is shown in Figure 2.11. Two beams of light generated by a laser propagating in opposite directions within an optical ring having radius  $R$ . One beam goes in clockwise ( $cw$ ) direction, while the other goes in a counterclockwise ( $ccw$ ) direction. The amount of time that light takes to travel within the ring, assuming only one loop, is  $t$  (Lefevre, 1993):

$$t = \frac{2\pi R}{c} \quad (2.10)$$

where  $c$  is the speed of light. Now, consider that the ring is rotating at a rate  $\omega$  in the clockwise direction. The two light beams travel a different fiber length and take a different time to traverse the total length of the fiber. The effective path lengths in the clockwise and counterclockwise directions can be defined as follows:

$$L_{cw} = 2\pi R + R\omega t_{cw} \quad (2.11)$$

$$L_{ccw} = 2\pi R - R\omega t_{ccw} \quad (2.12)$$

where  $t_{cw}$  and  $t_{ccw}$  are the transit times in the clockwise and counterclockwise directions, respectively. The optical path length difference  $\delta L$  can be obtained from equations (2.11) and (2.12) with  $N$  number of loops:

$$\begin{aligned} \delta L &= L_{cw} - L_{ccw} \\ &= \left( \frac{4\pi NR^2}{c} \right) * \omega \end{aligned} \quad (2.13)$$

From Equation (2.13), the apparent lengthening or shortening of the path is a directly proportional area ( $\pi R^2$ ) enclosed by the path for a constant rotation; and the sensitivity of an optical gyro depends in some way on its size. For a fiber optic coil of length  $L = 2\pi RN$ , the optical path difference can be rewritten as (Aein, 1995):

$$\delta L = \left( \frac{2RL}{c} \right) * \omega \quad (2.14)$$

It can be noted that by increasing the number of turns of the fiber optic coil (i.e., increasing the length of the fiber optic cable), the sensitivity of the two-beam Sagnac interferometer can be enhanced. However, the attenuation of the light beam along the fiber optic coil will impose restrictions on the increase of its length (Senior, 1993).

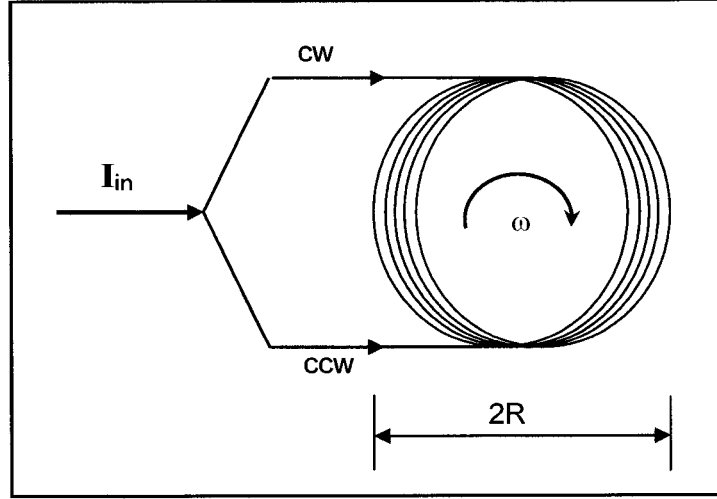


Figure 2.11 Two-beam interferometer using the fiber optic technology

In the case of the analog or Interferometric Fiber Optic Gyro (IFOG), the Sagnac phase shift caused by a rotation can be expressed in terms of  $\delta L$  as:

$$\begin{aligned}
 \delta \phi_s &= \left( \frac{2\pi}{\lambda} \right) * \delta L \\
 &= \left( \frac{8\pi^2 N R^2}{\lambda c} \right) * \omega \\
 &= K_s * \omega
 \end{aligned} \tag{2.15}$$

where  $\lambda$  is the wave length of the free-space optical energy, and  $K_s$  is called the Sagnac scale factor.

In the case of digital or resonant gyros, the energy in the counter propagating beams is coupled into the fiber loop at two different frequencies in the presence of rotation. The relative frequency difference  $\delta f$  between the two waves can also be written in terms of  $\delta L$  as (Yu and Yin, 2002):

$$\frac{\delta f}{f} = \frac{\delta L}{L} \tag{2.16}$$

The fundamental equation that relates  $\delta f$  to  $\omega$  is given by

$$\delta f = \left( \frac{2R}{\lambda} \right) * \omega \quad (2.17)$$

Optical gyros may be described as either passive or active and as resonant or non-resonant, according to how the Sagnac effect can be measured. If it is measured using external means, the sensor is passive, but in the case of active sensors, the Sagnac phase causes a frequency change internal to the gyro that signals the rotation directly (Lawrence, 1998). Two types of optical gyros will be presented next, along with their concepts and related errors.

### **Ring Laser Gyro**

The Ring Laser Gyro (RLG) is the most widely used gyro as an active resonant sensor and it has recently seen increased usage in strapdown navigation system mechanizations. Most RLG sensors are single degree-of-freedom sensors requiring three mechanizations for an inertial navigation implementation. RLG bases its operation, like any optical gyros, on the Sagnac effect. The number of RLG sides depends on the number of mirrors found at the corner. Figure 2.12 illustrates a triangle version of the RLG where there are three mirrors.

RLGs operate by using mirrors to set up a closed loop for the path of a laser. Beams of light are directed both clockwise and counter-clockwise around the closed path, and the position of one or more mirrors is then tuned to create a perfect standing wave pattern that remains stationary in inertial space. The mirrors are dielectric mirrors that reflect only the frequency of the laser. A fraction of the light is allowed to pass through one of the mirrors to photodiodes, which measure the interference pattern created by rotation.



They are typically very expensive, since they require a high voltage power source, a high power laser, and very fine machining of the laser cavity and mirrors.

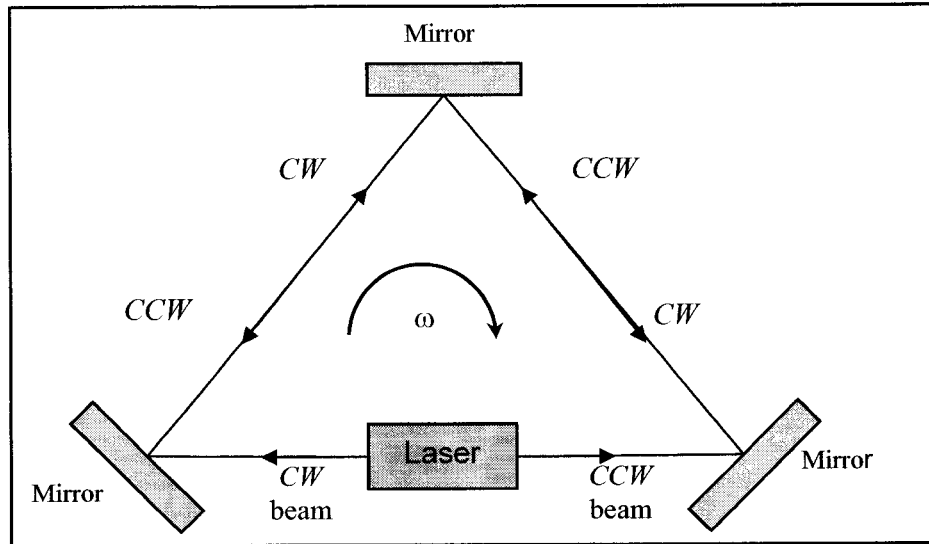


Figure 2.12 Concept of Ring Laser Gyro

One of the more considerable problems of the ring laser gyro is its susceptibility to a phenomenon called frequency lock-in. The two beams of light should have different frequencies when the gyro rotates around the normal axis to the resonator plane; however, the expected output frequency does not appear at low angular rate (Jekeli, 2001). This effect is caused by imperfections in the various components of the resonator cavity. Jekeli (2001) indicates that the earth's rotation ( $15^\circ/\text{hr}$ ) cannot be detected as its rate lies within the dead band region. The look-in phenomenon and the gyro response are shown in Figure 2.13.

There are three types of errors that have great effects on the gyro measurements: scale factor error, drift error, and random noise. Scale factor error may include a constant part and linearly parts. The uncompensated drift error may comprise residual temperature and

magnetic sensitivity terms in addition to a constant part due to medium flow and optical backscattering effects (Jekeli, 2001).

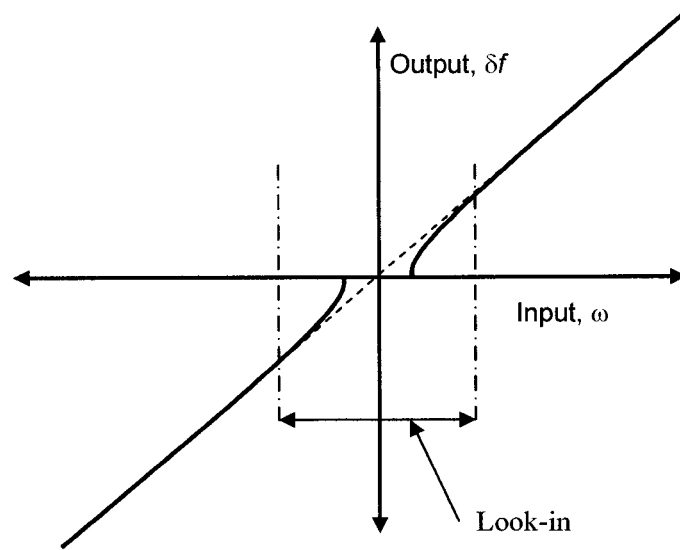


Figure 2.13 Ring Laser Gyro responses for input angular rate

Advantages of laser technology over any of the mechanical implementations include an extremely high dynamic range, excellent reliability since there are no mechanical parts to fail, and none of the dynamics related (acceleration) errors that are found in mechanical implementations. However, the laser cavity must be precisely machined and sealed, and an expensive high voltage laser is needed to construct an RLG.

### **Fiber Optic Gyro**

Fiber optic gyros (FOGs) have grown in popularity due to the rapid growth of fiber optic technology. In terms of the commercial value, FOG is the most important application of the fiber optic sensors (Stephen, 2000). It was recognized very early that the FOG presented the vision of all solid-state inertial sensor with no moving parts, high reliability, high tolerance for shock and vibration, and a potential of very low-cost (Mark et al., 1991).

The potential of FOG is clearly recognized since several companies worldwide are manufacturing them in large quantities to support automobile navigation systems, pointing and tracking of satellite antennas, and inertial measurement systems for commuter aircraft and missiles. There are also other applications for FOG including mining operations and tunneling.

Interferometric FOG can be configured as either “closed-loop” or “open-loop.” The complexity of the closed-loop restricts it to avionics and inertial navigation grade applications (Bennett et al., 1998). Figure 2.14 illustrates the open-loop configuration, which consists of a fiber coil, two directional couplers, a polarizer, optical source, and detector. A piezoelectric device, wound with a small length of one end of the fiber coil, applies a non-reciprocal phase modulation.

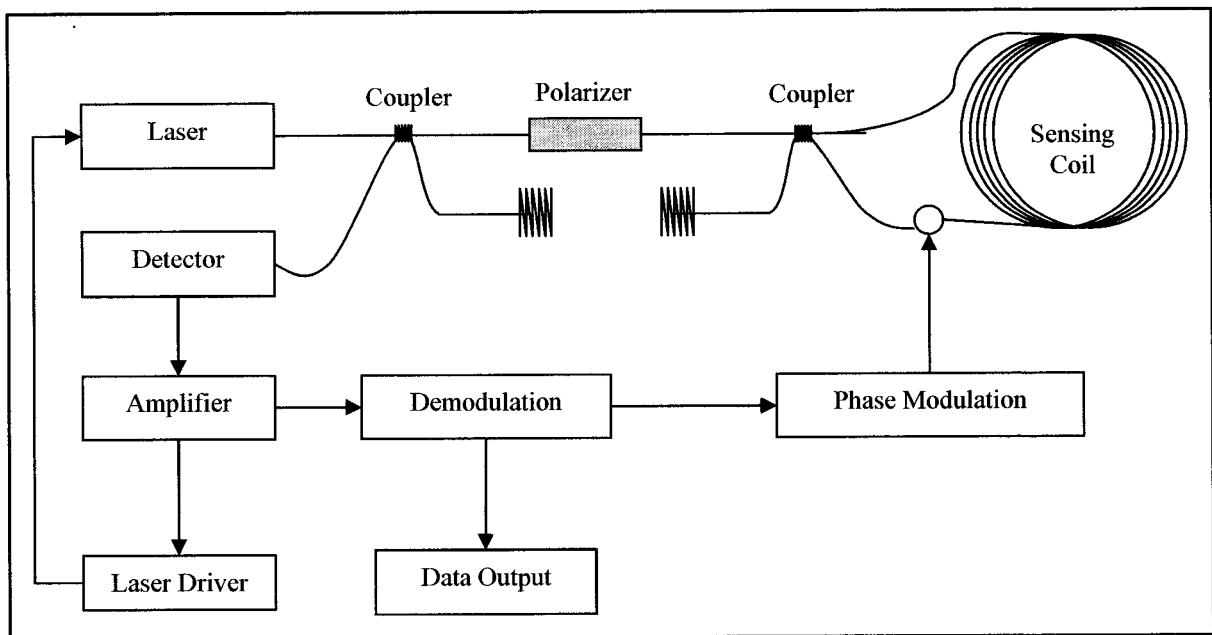


Figure 2.14 FOG Electrical and Optical Circuits (Bennett et al., 1998)

In a FOG, the optical path is a fiber optic cable that is normally coiled  $N$  times around a cylinder. The light beam is emitted from a laser diode or superluminescent diode, passed

through a polarizer, and split by the coupler into two signals with equal intensity. The light going to one side of the coil passes immediately through a phase modulator, while the light moving in the opposite direction will not pass the phase modulator until it has almost completed the path and is about to be recombined by the coupler. The light is combined at the coupler, cleaned again by the polarizer, and passed on to the photo detector. The two light beams pass through the same path, and all environmental effects, except rotation, have the same effect on each beam and are canceled.

At the directional coupler attached to the coil, the two waves combine in an optical interferometer. The light intensity returning from the coil to the polarizer is a raised cosine function (Figure 2.15), having a maximum value when there is no rotation and a minimum when the optical phase difference is  $\pm\pi$  (half an optical wavelength). This effect is independent of the shape of the optical path, and of the propagation medium (Lefevre, 1993). FOG is sensitive only to rotation about the axis perpendicular to the plane of the coil. Due to the cosine shape, the change in interferometer output is small for small input rotation rates, and it would not be possible to determine the sense of rotation since the decrement in amplitude is equal for both directions of rotation, making it necessary to apply a dynamic phase bias to the light path. Not only does applying a dynamic phase bias overcome these problems, but it also moves the demodulation to a frequency well removed from DC, eliminating bias drifts associated with offsets in the low level amplifiers.

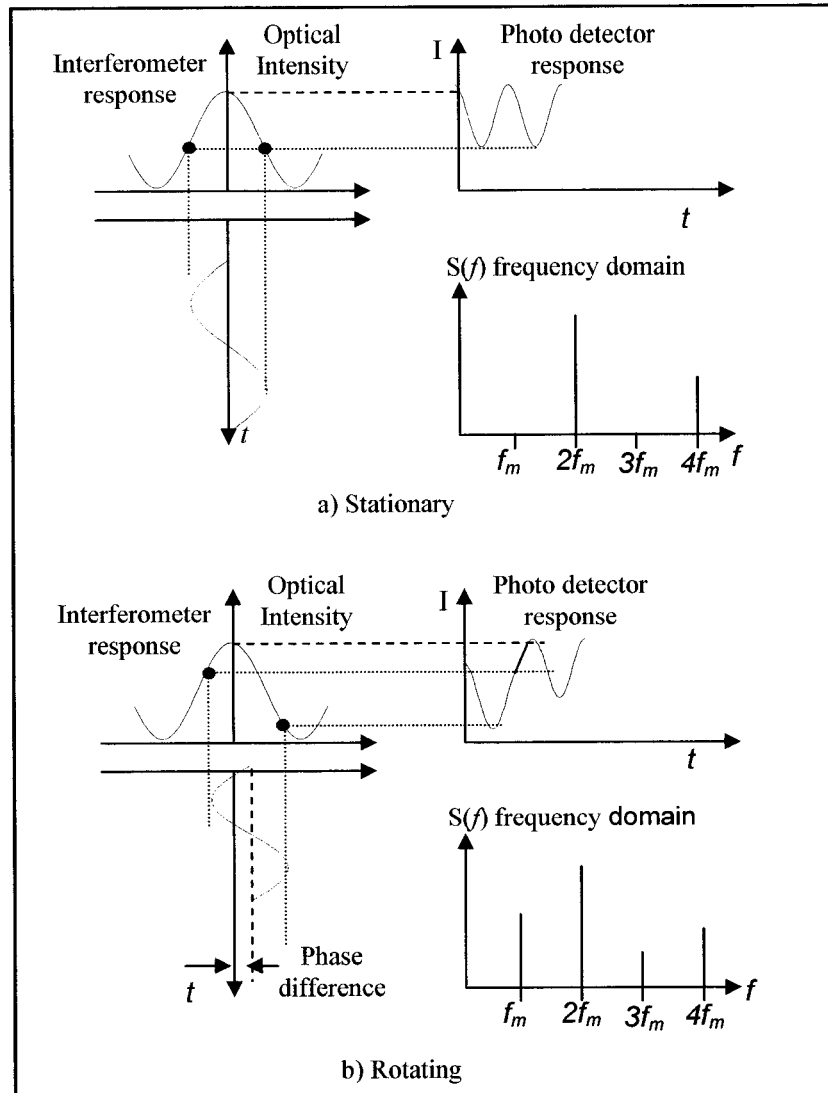


Figure 2.15 Sagnac interferometer responses for open loop configuration (Bennett et al., 1998)

In practice, environmental effects can limit the rotation measurement accuracy of high performance IFOGs. Environmental noise sources, such as the Faraday effect and the “Shupe” effect, introduce an optical intensity-induced nonreciprocal phenomenon (Lawrence, 1998; Lefevre, 1993). Nonreciprocity is caused by different polarizations of the two beams, thus requiring that they first pass through a polarizer. The magnitude of the environmental effects depends strongly on the way the FOG is packaged and used.

A typical error model for the FOG can be expressed in a similar way to RLG error, consisting of a scale factor error, drift error, and random noise. Commercial grade IFOG has uncompensated drift from 0.5 °/hr to 150 °/hr, and uncompensated scale factor errors from 100 ppm over 1000 ppm (Jekeli, 2001).

## 2.2 SIGNPOST POSITIONING SYSTEM

The signposts concept is a simple positioning system. As the bus location can be defined by virtue of the fact that the bus is located near a known location (signpost). Signposts depend mainly on the three types of waves, specifically radio, light, and sound waves and are installed on utility poles (Figure 2.16). This system may be composed of an on-board, short-range communication device and an infrastructure mounted beacon. The existing systems work in two modes (Okunieff, 1997). The first one is a vehicle with a transponder continuously sending a signal; within range, the signpost responds with its identification code. In the second mode, the signpost continuously broadcasts its identification number, which can be detected by any bus or vehicle equipped with the proper receiver.

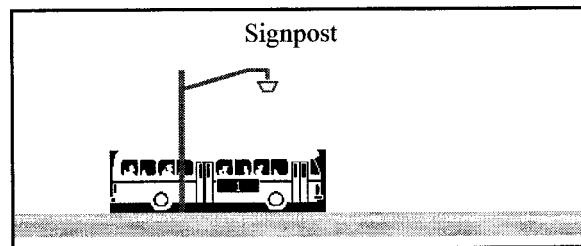


Figure 2.16 Signpost System

The signpost signal coverage is determined by a number of factors, including the type of signpost and its signal strength. There are two types of signpost beacons available according to their coverage area (Pekilis and Heti, 1992). The first is wide focus beacons, where the signpost emits a broad signal that covers an entire intersection (i.e., 60 meters radius). Narrow focus beacons transmit their identification code over a closely defined area. Generally, narrow focus beacons are more accurate but, in practical terms, wide focus beacons can be used to cover several routes, and suitable software can be used to correct the final solution. Figure 2.17 illustrates the two types of signpost systems.

Unfortunately, signpost systems whether narrow focus or wide focus, are not useful at all if a bus changes its regular route. Thus, changes or expansions in bus routes could require the installation of additional signposts. The advantages and disadvantages of signpost technology are summarized in Table 2.3.

### 2.2.1 Signpost System Components

Signpost components are similar to any wave-based system. Such a system consists of two antennas, transmitter electronics, and receiver electronics with specific characteristics.

Table 2.3 Advantages and disadvantages of signpost technology

Advantages	Disadvantages
Low-cost for the bus-mounted unit	Requires well-equipped infrastructure
Robustness	Can be used only for fixed routes
	Frequency of updates depends on density of signposts

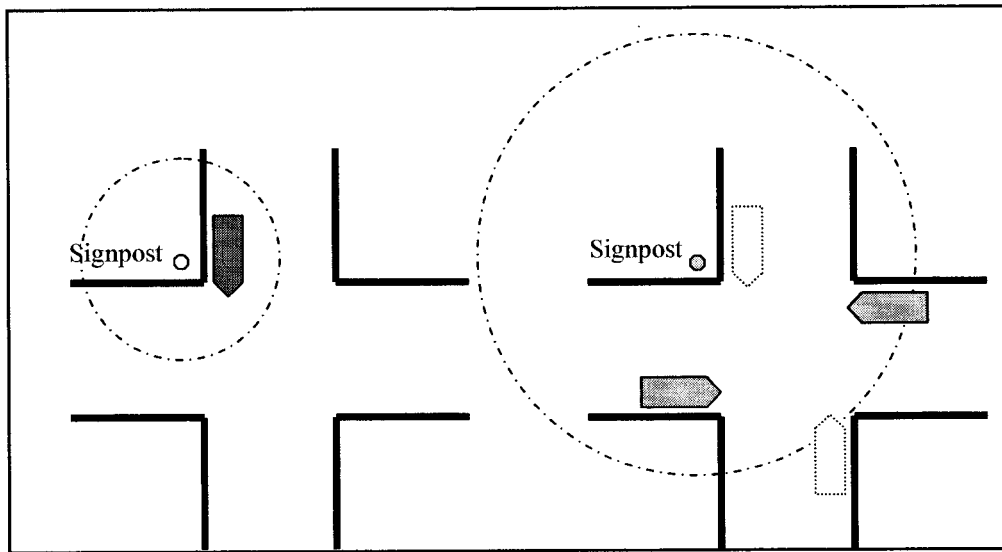


Figure 2.17 Narrow focus beacons and Wide focus beacons

#### 2.2.1.1 Antennas

The requirement of the signpost antenna (transmitter/receiver) combination is that the output signals are received in localized, well-defined areas. Localization can be achieved using high frequency signals with low-power transmission. The atmosphere will attenuate short-wave length and limit the distance of transmission. Furthermore, low power will reduce the probability of reception over any large distance. The well-defined area requirement can be achieved using an antenna with a narrow beam width, or at least with a pattern that covers only the required area.

#### 2.2.1.2 Transmitter Electronics

Figure 2.18 illustrates the conceptual block diagram of the transmitter electronics for a signpost positioning system. The power supply and user interface are excluded from this block diagram. However, the transmitter consists of seven main components:



1. *Oscillator*: which produces the fundamental frequency  $f_0$  in a periodic sinusoid waveform. This oscillator must be stable with less frequency drift. However, small frequency drifts can degrade system performance. If the drift is very large, signals outside the allotted frequency band can result.

2. *Translator*: responsible for converting the fundamental frequency  $f_0$  produced by the oscillator to the final frequency needed for transmission.

3. *Modulator* is the process by which the code is added to the waveform produced by the translator. Most signpost systems require low data rate; in this case, a simple binary modulation (zeros and ones) technique is used.

4. *Amplifier*: boosts the signal power to the level that warrants the signal will arrive at the receiver.

5. *Filter*: filters out any extra energy lying outside the desired band.

6. *Source*: produces the data that is to be sent as part of signpost transmission. This data is primarily the transmitter's identification number.

7. *Coding*: performs channel coding on the data to detect and correct the errors that occur during transmission. There are two different coding ways: block coding and convolution coding. In block coding, the data stream is divided into segments, and the coding operation is carried out for every segment. The simplest form of block coding is a parity check. Convolution coding is a continuous operation carried out on the whole data stream.

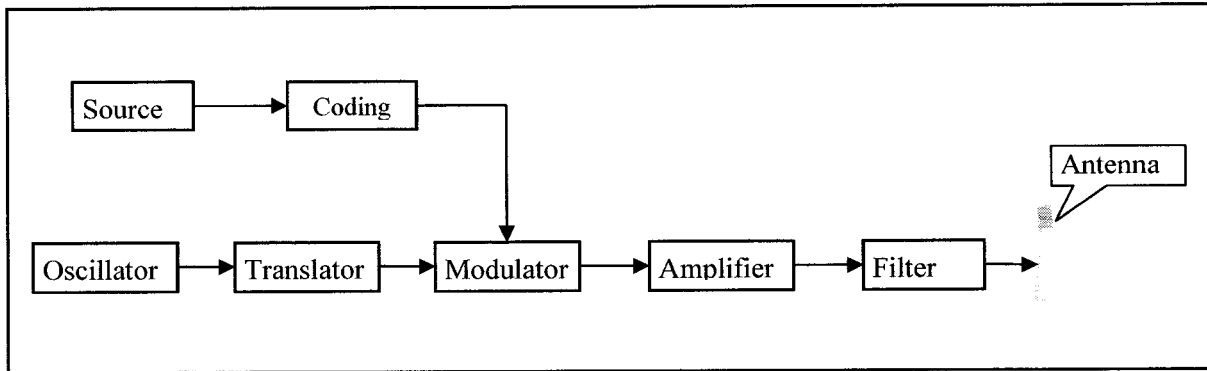


Figure 2.18 Block diagram of transmitter electronics for a signpost (Drane and Rizos, 1997)

#### 2.2.1.3 Receiver Electronics

Figure 2.19 illustrates the conceptual block diagram of the receiver electronics for a signpost positioning system. The signal received by the antenna is very weak and distorted by noise. The signal is taken directly from the antenna to the amplifier, where it is enhanced to a suitable level for processing. After that, the signal is demodulated into the original transmitted bits. Finally, the signal is checked for any errors. The functions of the demodulator and decoder are described below.

*Demodulator:* is applied to get binary data from the waveform signal. The performance of the data demodulator can be characterized in terms of the error probability, which is the probability of making a decision error. To guarantee a low probability of error, the signal power, bandwidth, data rate, and modulation technique must be chosen normally.

*Decoder:* is the last step, and is used to detect and/or correct any errors in transmission. However, channel coding and decoding techniques are quite complex, and many sophisticated approaches have been developed (Drane and Rizos, 1997).

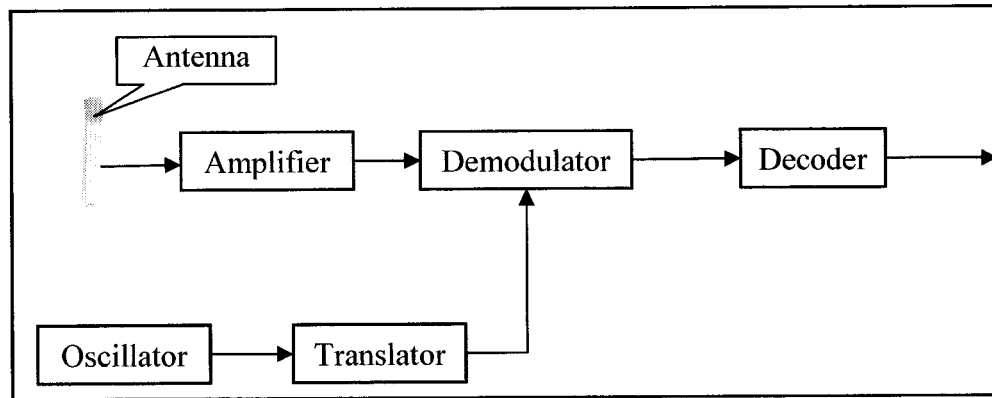


Figure 2.19 Block diagram of receiver electronics for a signpost (Drane and Rizos, 1997)

## **CHAPTER 3**

### **GLOBAL POSITIONING SYSTEM**

Global Positioning System (GPS) is a satellite-based radio system designed and developed by the U.S. Department of Defense (DoD). Using signals transmitted by its satellites, GPS can provide real-time measures of position, velocity, and time, independent of weather conditions, virtually 24 hours a day. In this chapter, GPS components will be reviewed. Also a review of pseudorange and carrier-phase observation equations will be presented as well as GPS errors and biases.

#### **3.1 GPS COMPONENTS**

The GPS system, like all satellite-based navigation systems, is composed of three segments: space, control, and user (Figure 3.1). The space segment is comprised of a nominal constellation of 24 GPS satellites orbiting about 20,200 km above the earth's surface in six, equally spaced, orbital planes. There are at least four satellites distributed in each plane since the actual constellation includes more than 24 satellites. Each satellite transmits sine wave signals on two frequencies, L1 at 1575.42 MHz and L2 at 1227.60 MHz. The L1 frequency is modulated by two pseudorandom noise (PRN) codes in the binary format; one is the Coarse Acquisition (C/A) code and the other is the Precise (P) code. At present, the L2 frequency is modulated only by the P code. The C/A-code is transmitted at 1.023 Mbps and is repeated every one millisecond, while the P-code is transmitted at 10.23 Mbps and is repeated every 266 days (38 weeks). The navigation message, which contains the GPS satellite ephemeris, clock, and satellite health information, is modulated on both frequencies (El-Rabbany, 2002).

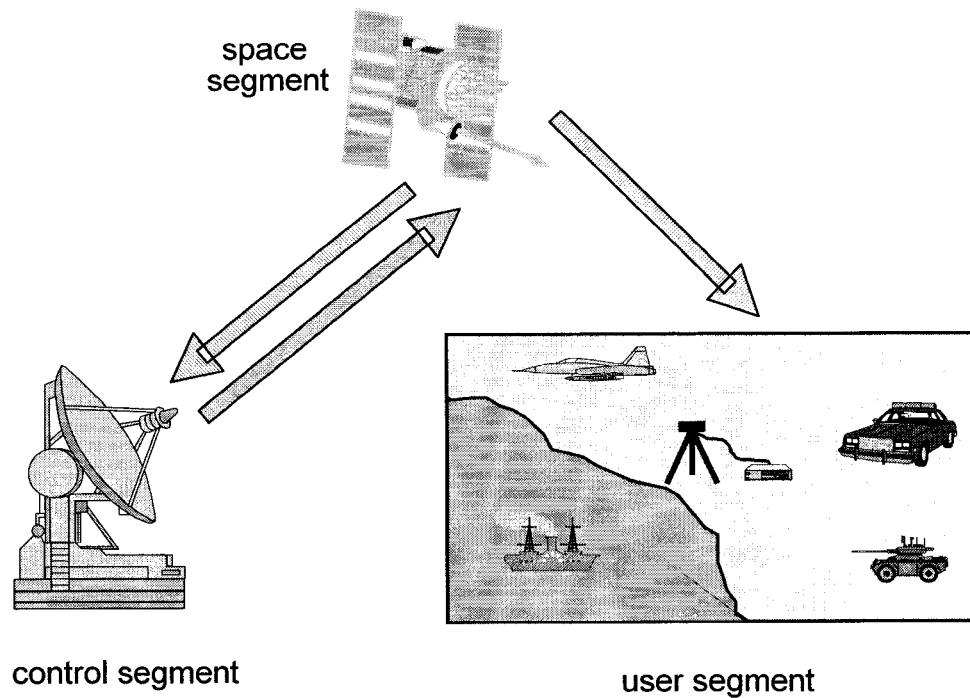


Figure 3.1 GPS constellation System (from El-Rabbany, 2002)

The GPS system was declared fully operational on July 17, 1995, when 24 blocks II satellite were available. Therefore, a minimum of four and a maximum of ten GPS satellites will be visible anywhere in the world, if an elevation angle of  $10^\circ$  is considered. However, since Anti-spoofing (AS) is turned on, the P-code is converted to Y-code, which allows access only to users who have the key. Since receiver technology is developing quickly, many civilian receivers can still measure L2 pseudorange and carrier-phase data through various techniques (El-Rabbany, 2002).

The control segment consists of a master control station, a worldwide network of monitor stations, and ground control stations. The monitor stations are responsible for collecting GPS data and sending these data to the master control station. All estimates of the broadcast ephemeris and other satellites' parameters are carried out at the master control

station. The outcome from the master control station is sent to one of the ground control stations that upload it to the satellites on the S-band frequency (Hofmann-Wellenhof et al., 2001).

The user segment consists of any GPS receiver connected to a GPS antenna that can receive the radio signals from the GPS satellites. The received signals are used to obtain the GPS solution parameters which may be obtained either in real time or post processing.

### **3.2 GPS OBSERVATIONS**

The fundamental observables used in the GPS are the carrier-phase and the pseudorange. The carrier-phase is the most important for applications where centimeter to decimeter level accuracy is needed. The pseudorange is less accurate than the carrier-phase measurements and will be presented in detail, as it is used by the developed integrated system.

Carrier-phase measurements are made on a beat phase. A beat phase is formed by the difference between the incoming carrier-phase and the reference signal generated by the receiver. Only a fractional part of one cycle can be measured accurately. The phase change is measured by the Doppler count, which is the number of accumulated whole cycles. Therefore, the initial number of integer cycles in the carrier-phase measurements is unknown. This is the so-called initial ambiguity parameter (Wells et al., 1987).

The pseudorange is measured by comparing the code arriving from the satellite with a replica of the code generated in the receiver to determine the time shift to correlate the two signals (Figure 3.2). Let  $t^s$  and  $t_r$  denote the readings of the satellite clock at emission

time (according to satellite time scale), and receiver clock at the signal reception time (according to receiver time scale). In addition to the satellite and receiver time scales, there is a more or less ideal time scale called GPS time ( $t_{(GPS)}$ ). The difference between the clock readings is equivalent to the time shift  $\Delta t$  (Wells et al., 1987):

$$\begin{aligned}
 \Delta t &= t_R - t^s \\
 &= [t_{r(GPS)} - \delta_r] - [t_{(GPS)}^s - \delta^s] \\
 &= \Delta t_{(GPS)} + (\delta^s - \delta_r) \\
 &= \Delta t_{(GPS)} + \Delta \delta
 \end{aligned} \tag{3.1}$$

where  $\delta^s$ ,  $\delta_r$  are the satellite and the receiver clock error, respectively. The satellite clock error  $\delta^s$  can be modeled, up to a residual value of several nanoseconds, by a second degree polynomial with the coefficients being transmitted in the navigation message. By applying the satellite clock correction,  $\Delta \delta$  becomes equal to the receiver clock delay. The time interval  $\Delta t$  multiplied by the speed of light  $c$  yields the pseudorange  $PR$  (Hofmann-Wellenhof et al., 2001):

$$\begin{aligned}
 PR &= c\Delta t = c\Delta t_{(GPS)} + c\Delta \delta \\
 &= \rho + c\Delta \delta
 \end{aligned} \tag{3.2}$$

where  $\rho$  is the true distance between the satellite antenna at epoch  $t_{(GPS)}^s$  and the receiver antenna at epoch  $t_{r(GPS)}$ . It is important to notice that the C/A-code repeats itself every millisecond, which corresponds to 300 km in range. Since the satellites are at a distance of about 20000 km from the earth, C/A-code pseudoranges are ambiguous. However, this ambiguity can be fixed using approximate position coordinates (Lachapelle, 1991).

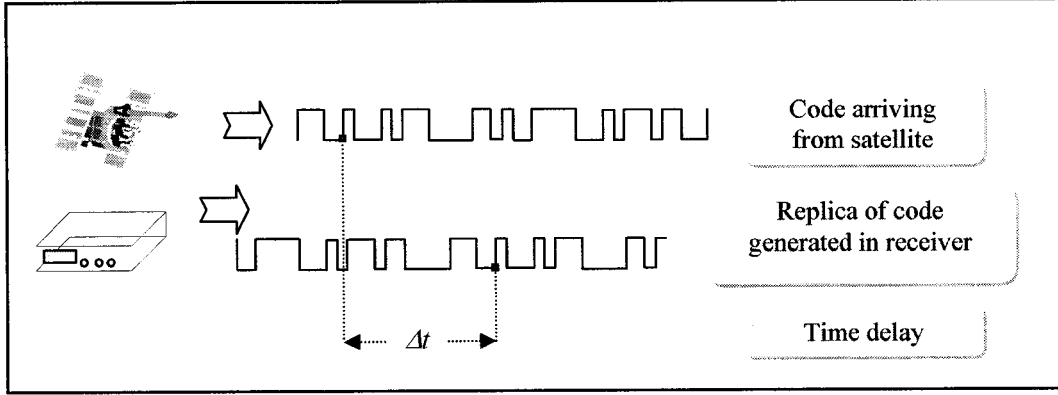


Figure 3.2 Pseudorange measurement

Assuming that the receiver coordinates are  $(x_r, y_r, z_r)$  and the satellite coordinates are  $(x^s, y^s, z^s)$ , the slant distance between the satellite and the receiver can be written as:

$$\rho = \sqrt{(x^s - x_r)^2 + (y^s - y_r)^2 + (z^s - z_r)^2} \quad (3.3)$$

From equations 3.2 and 3.3, four pseudoranges from four different satellites are used to solve the three position components and one receiver clock error (Leick, 1995). However, more than four satellites give a redundancy observation; hence least squares or Kalman filtering can be used to estimate the receiver position and clock error unknowns.

In Equation 3.2, no biases are considered. However, in reality, there are biases due to, e.g., earth's atmosphere, orbital error, multipath, and measurement noise. Considering these biases, the pseudorange observation equation can be expressed as (Kaplan, 1996):

$$PR = \rho + c\Delta\delta + d^{ion} + d^{trop} + d_\rho + d_m + \varepsilon_p \quad (3.4)$$

where

$PR$  is the pseudorange observation (m)

$\rho$  is the satellite receiver range (m)



$c$  is the speed of light (m/s)  
 $d^{ion}$  is the ionospheric correction (m)  
 $d^{trop}$  is the tropospheric correction (m)  
 $d_m$  is the multipath effect (m)  
 $d_p$  is the orbital error (m), and  
 $\varepsilon_p$  is the pseudorange measurement noise (m).

Finally, for the sake of completeness, the carrier-phase observation equation can be defined as:

$$\Phi = \rho + c\Delta\delta + \lambda N - d^{ion} + d^{trop} + d_p + \varepsilon_\phi \quad (3.5)$$

where

$\Phi$  is the carrier-phase observation (m)  
 $\lambda$  is the carrier-phase wave length (m)  
 $N$  is the carrier-phase integer ambiguity parameter (cycles), and  
 $\varepsilon_\phi$  is the carrier-phase measurement noise (m).

### 3.3 GPS ERRORS AND BIASES

GPS measurements, either pseudorange or carrier-phase, are affected by several types of errors and biases. These errors are classified as satellites-related errors, receiver-related errors, and atmospheric-related errors. The satellite-related errors include orbital errors, satellite clock errors, and the effect of selective availability that has been turned off since May 2000 (El-Rabbany, 2002). The second type of error includes the receiver clock errors, multipath errors, system noise, and antenna phase center. The last one is signal propagation error, which is divided into two main parts: the tropospheric effect and the

ionospheric effect. In addition to these three types of errors, there is the significant effect of the satellite geometry.

### 3.3.1 Orbital Error

The main assumption to use GPS for positioning is that the satellite coordinates are known. These coordinates can be obtained in terms of an ephemeris, which is a mathematical description of where a satellite is at a given time. Currently, orbital data are available in three formats: almanac, broadcast ephemeris, and precise ephemeris (Hofmann-Wellenhof et al., 2001). These data types differ in accuracy. The broadcast orbits errors have been consistently decreasing over the last decade, from a median of about 7 m in 1992 to 4 m in 2000 (Jefferson and Bar-Sever, 2000).

A precise orbit is an alternative method for computing the satellite coordinates. It is very accurate but, unfortunately, it is not available for real-time applications at present. These ephemeris parameters are produced by a number of agencies in different forms according to the availability of data collected, namely ultra-rapid, rapid, final orbit (IGS, 2001).

### 3.3.2 Satellite and Receiver Clock Errors

Every satellite has cesium and/or rubidium atomic clocks onboard. These clocks are very accurate, but not perfect (El-Rabbany, 2002). Due to instabilities in the GPS satellite oscillators, the user must correct for the satellite clock error. The satellite clock error can be approximated by using second-degree polynomial (Wells et al., 1987):

$$\delta t^s = a_0 + a_1(t - t_{oc}) + a_2(t - t_{oc})^2 \quad (3.6)$$

where

$t_{oc}$  is the reference epoch (s)

$t$  is the measurement transmission time (s)  
 $a_0$  is the satellite clock offset (ns)  
 $a_1$  is the fractional frequency offset (ns/s), and  
 $a_2$  is the fractional frequency drift (ns/s<sup>2</sup>).

The coefficients  $a_0$ ,  $a_1$ , and  $a_2$  above, are transmitted as part of the navigation message.

Unlike GPS satellites, GPS receivers use low-priced clocks, which are much less accurate than atomic clocks. For real-time applications, the receiver clock error is added as an additional unknown parameter. So, four satellites are required in view for positioning. An external accurate clock can also be used to aid GPS receiver to enhance the final solution or to reduce the number of unknowns (Zhang, 1997).

### **3.3.3 Multipath Error**

Multipath is the phenomenon whereby a signal is reflected from various objects and arrives at the GPS antenna via different paths (Hofmann-Wellenhof et al., 2001). An example of this effect is shown in Figure 3.3. As a result, it is highly dependent upon the conditions surrounding the receiver antenna (e.g., buildings and vehicles) and the type of antenna that is used (Raquet, 1998).

Multipath is one of the most significant errors, especially for pseudorange, since the GPS receiver cannot distinguish between a direct signal and a reflected one. As a result, the antenna takes the measurement based on the combined signal rather than on the direct signal, resulting in the multipath error. Multipath errors are difficult to remove because there is no suitable model that can be used for the general case. However, the maximum multipath error may be in the range of 15 m for code measurements and a quarter wavelengths for the phase measurements (Ray, 2000)

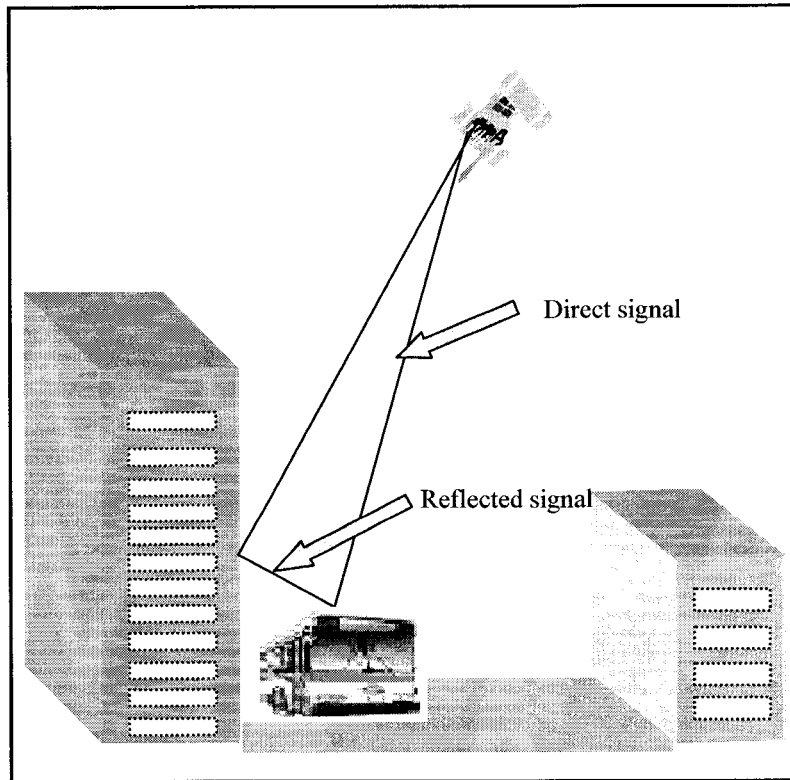


Figure 3.3 Multipath effect

Improvements in GPS receivers have decreased the multipath errors. Examples of such improvements are Strobe Correlator and Multipath Estimating Delay Lock Loops (MEDLL) (El-Rabbany, 2002). Lachapelle et al. (1996a) found that MEDLL was the most effective method in reducing multipath error.

#### 3.3.4 System Noise

System noise is any noise that is generated by the receiver itself while taking measurements. This noise depends mainly on the receiver's electronics. It consists mostly of thermal noise intercepted by the antenna or produced by the receiver's internal components. Its magnitude depends on parameters such as bandwidth; carrier to noise density ratio; and code and code tracking mechanization parameters.

The receiver noise is not correlated between the pseudorange and carrier-phase measurements since they depend on different techniques. The former depends on the Delay Lock Loop (DLL) and the latter depends on Phase Lock Loop (PLL). The DLL measurement errors are composed of thermal noise and dynamic stress error (Kaplan, 1996).

Typically, the level of receiver noise is less than 1% of the wavelength. In Raquet (1998), the carrier-phase noise level was shown to have a maximum standard deviation of 0.8 mm for L1 and 1.3 mm for L2 for a high-grade receiver. It was also shown that the noise level of the code and carrier-phase measurements decreases as the elevation angle increases up to about 45°, where it becomes constant (Olynik, 2002).

### 3.3.5 Tropospheric Error

The troposphere layer is the lower region of the atmosphere. It is electrically natural and extends to approximately 50 km above the surface of the earth. It is a non-dispersive medium for frequencies less than 15 GHz (Hofmann-Wellenhof et al., 2001). However, within this region, the phase and the code velocities will be less than the speed of light in the free space. Hence, the measured satellite-to-receiver range will be longer than the actual geometric range (El-Rabbany, 2002). The magnitude of tropospheric delay  $d^{Trop}$  can be expressed as (Hofmann-Wellenhof et al., 2001):

$$d^{Trop} = \int (n-1) ds \quad (3.7)$$

where  $n$  is the index of refraction along the path of signal. Usually, instead of the refractive index  $n$  in Equation 3.7, the refractivity ( $N^{Trop} = 10^6(n-1)$ ) is used:

$$d^{Trop} = 10^{-6} \int N^{Trop} ds \quad (3.8)$$

The tropospheric delay is a function of the distance traveled by the electromagnetic signal through the neutral atmosphere. This distance is a function of the elevation of the satellite. Therefore, the tropospheric delay for a satellite at elevation ( $E_v$ ) is often written as the product of the delay at the zenith ( $E_v=90^\circ$ ) and a mapping function  $F$  which relates this zenith delay to the delay at elevation ( $E_v$ ):

$$d^{Trop} = F(E_v, \underline{P}).d^{Trop}(90^\circ) \quad (3.9)$$

$F(E_v, \underline{P})$  is a function of elevation; sometimes it includes other parameters, contained in the vector  $\underline{P}$ .

The effect of the troposphere is usually considered as a mixture of a dry and a wet component. The dry component contributes about 90% of the total tropospheric delay and can be modeled mathematically with high accuracy at the zenith. The wet component is approximately 10% of the total tropospheric delay. Unlike the dry component, the accurate estimation of the wet component is difficult because of the variability of water vapor. When the elevation angle of a satellite decreases (below  $10^\circ$ ), the tropospheric delay will be much greater and will be estimated with much less accuracy. This in turn affects the accuracy of the estimated position. This loss of accuracy is one major reason why satellites with elevation angles greater than  $10^\circ$  are used for GPS positioning.

Generally, the tropospheric delay is affected by a number of parameters, such as the temperature, humidity, pressure, the height of the user, and the humidity along the signal path through the troposphere.

### **3.3.6 Ionospheric Error**

The ionosphere is a layer of the atmosphere that is approximately from 50 to 1000 km above the Earth's surface. It is composed of a sufficient concentration of free electrons to affect electromagnetic waves significantly. GPS signals traveling through the ionosphere are affected by refraction and dispersion. Unlike the troposphere, its effect on the code is different from the phase measurements. It speeds up the propagation of the carrier-phase beyond the speed of light, while it slows down the pseudorange code by the same amount.

The ionospheric effect is proportional to the Total Electron Content (TEC) along the signal propagation path. The TEC varies with solar ionizing flux, magnetic activity, sunspot cycle, season, time of day, user location, and satellite elevation angle. Normally, the amount of ionospheric error may range from 5 m to 15 m (at night, during periods of minimum sunspot activity, with the satellite at the zenith). However, the ionospheric effect can be more than 150 m (at midday, during periods of intense sunspot activity, with the satellite at low elevation) (Wells et al, 1987).

### **3.3.7 Satellite Geometry Effect**

The satellite geometry, which represents the geometric locations of GPS satellites as seen by the receiver, plays an important role in the total positioning accuracy. Good satellite geometry is obtained when the satellites are spread out in the sky. In general, the more spread out the satellites are in the sky, the better the satellite geometry. In an urban environment, weak satellite geometry is frequently observed in terms of cross-track satellite geometry, the direction perpendicular to the vehicle trajectory.

The effect of the satellite geometry is generally represented by the Geometric Dilution Of Precision (GDOP), which is computed from the square root of the trace of the cofactor matrix obtained in a position fix, using pseudoranges to a minimum of four tracked satellites. Thus,

$$GDOP = \sqrt{q_{\phi}^2 + q_{\lambda}^2 + q_h^2 + q_t^2} \quad (3.10)$$

where  $q_{\phi}^2, q_{\lambda}^2, q_h^2$ , and  $q_t^2$  represent the cofactors of the latitude, longitude, height, and time, respectively, which is obtained from the cofactor matrix of the estimated position parameters. The GDOP values are not constant; they vary with time and user location.



## **CHAPTER 4**

### **METHODOLOGY**

As mentioned earlier, the DR system is not a reliable positioning system by itself. Therefore, merging the DR solution with other aiding systems gives a better performance. This chapter first describes different aiding systems followed by the DR measurements and related mathematics. Also, DR modeling errors are presented in detail as well as Kalman filter concept, design, and parameters.

#### **4.1 AIDING INTEGRATED SYSTEM**

The concept of sensor aiding is based on estimating the DR errors by comparison with another navigation aid, such as GPS or signpost. DR has good short term accuracy characteristics but its accuracy is subject to long term effects, such as gyro drift and integration error. To generate accurate navigation solutions, DR must be combined with another aiding sensor. There are two kinds of DR aiding concepts, the feed-forward and the feed-back.

Figure 4.1 illustrates the feed-forward concept. In this method, DR estimates the current position using the previous position and new measurements (Equations 2.1 and 2.2). At signpost location, if the GPS solution is available, the difference between the DR and the signpost will feed to the filter. In this case, the quantity passed to the filter is a combination of DR error, aiding sensor error, and imperfections or limitations in the dynamic model. The best estimate for the DR system will be defined through the filter and the final solution is updated.

Figure 4.2 illustrates the feed-back or extended Kalman filter. The same procedures as in the feed-forward method are used, but filter corrections feed the DR solution for the next step (Brown and Hwang, 1997).

## 4.2 DEAD RECKONING MEASUREMENTS

As mentioned in Chapter 2, DR navigation is based on integrating velocity to obtain traveled distance and heading. DR navigation requires that the traveled distance and direction (heading) be available on a continuous basis. Coordinates of start point and initial direction are needed since DR is a relative positioning system (Zhao, 1997).

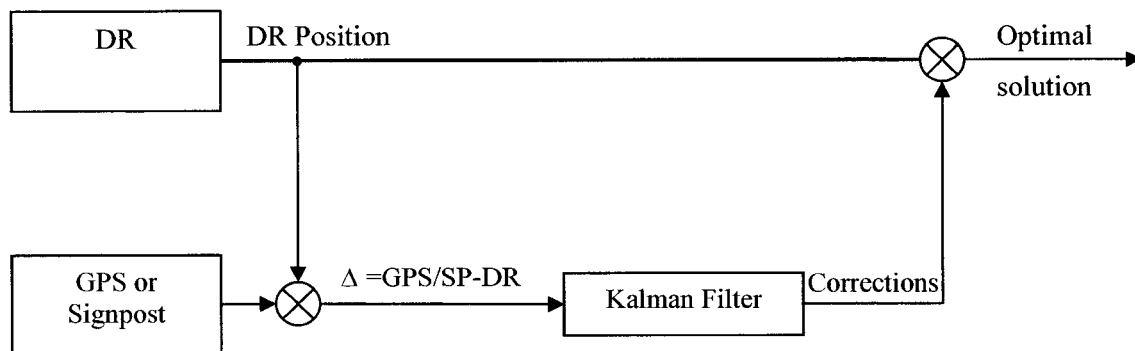


Figure 4.1 Feed-forward aiding system

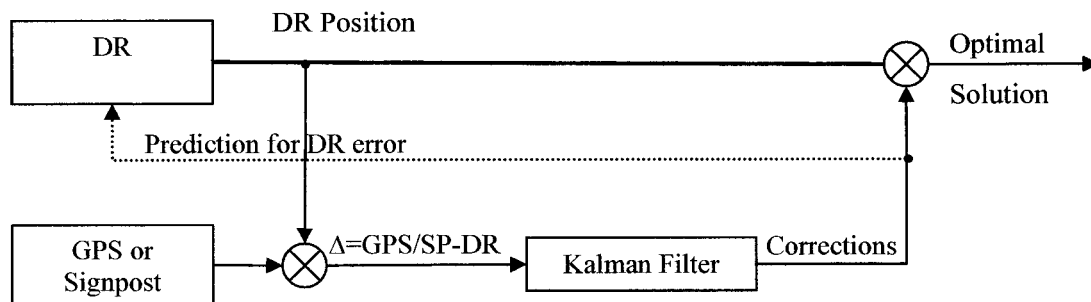


Figure 4.2 Feed-back aiding system (Extended Kalman Filter)

The output velocity from the system is in the body frame which generally refers to the vehicle to be navigated and its axes are typically defined along the forward, right, and through-the-floor directions (Jekeli, 2001). To get this velocity in the navigation frame (North and East), transformation from the body frame to the navigation frame must be carried out first via heading angle (Figure 4.3):

$$\mathbf{v}^N = \mathbf{R}_B^N \mathbf{v}^B$$

$$\begin{bmatrix} v^{north} \\ v^{east} \end{bmatrix} = \begin{bmatrix} \cos \psi & -\sin \psi \\ \sin \psi & \cos \psi \end{bmatrix} \begin{bmatrix} v \\ 0 \end{bmatrix} \quad (4.1)$$

where:

$v^{north}$  and  $v^{east}$  are velocities in the north and east directions, respectively,  $\mathbf{R}_B^N$  is the transformation matrix from the body frame to the navigation frame,  $v$  is the velocity in the body frame (direction of motion), and  $\psi$  is the heading angle, counter-clockwise being positive.

The main assumptions for the above equation are that the pitch and roll angles are small enough, so their effect will be ignored. The heading  $\psi$  in the above equation can be obtained by numerical integration for the rate gyro output:

$$\psi = \psi_0 + \int \dot{\psi} dt \quad (4.2)$$

where  $\psi_0$  is the initial heading, which may be estimated from the road direction or any other known information.

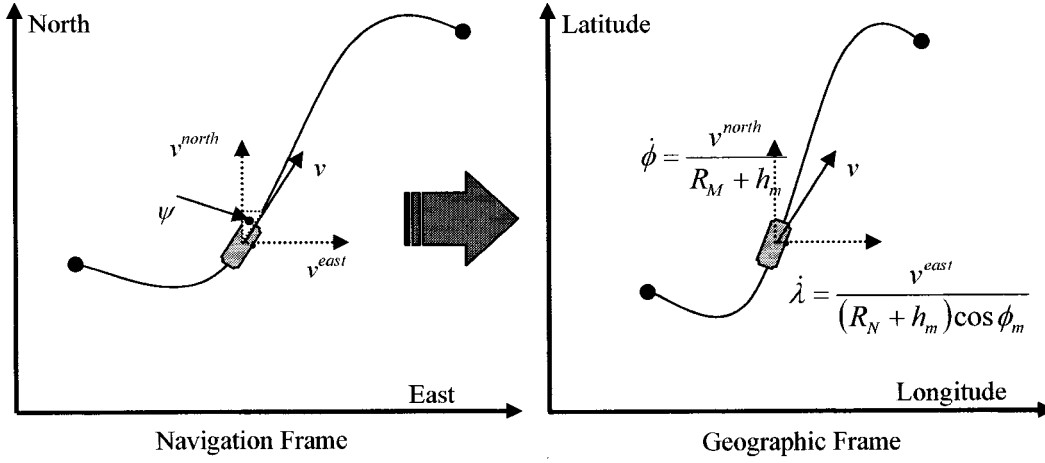


Figure 4.3 Transformation from Navigation frame to Geographic frame

The second transformation is from the navigation frame to the geographic frame, which is given by:

$$\begin{bmatrix} \dot{\phi} \\ \dot{\lambda} \end{bmatrix} = \begin{bmatrix} \frac{1}{R_M + h} & 0 \\ 0 & \frac{1}{(R_N + h) \cos \phi_m} \end{bmatrix} \begin{bmatrix} v^{north} \\ v^{east} \end{bmatrix} \quad (4.3)$$

where:

$\dot{\phi}$  and  $\dot{\lambda}$  are the rates of change in the latitude and longitude directions, respectively;  $R_M$  and  $R_N$  are the meridian and prime vertical radii of curvatures of the best-fitting ellipsoid, respectively; and  $\phi_m$  is the average latitude and  $h$  is the ellipsoidal height in the region.

## 4.3 KALMAN FILTER DESIGN

### 4.3.1 Kalman Filter

Kalman filtering technique has been widely used in several applications since its introduction in 1960 (Welch and Bishop, 2001). It has been the subject of extensive

research and application, particularly in the area of autonomous or aided navigation. Its recursive implementation is well suited to accommodating diverse sources of data at different times in a statistically optimal manner (Gelb, 1974). It estimates the state of a system based on knowledge of system dynamics and a series of measurements corrupted by noise.

Kalman filter consists mainly of two steps. The first is the prediction step, which depends on the assumed dynamic model and the statistical properties associated with its noise. The key to this is the dynamic model with its associated process noise value. If the model is wrong, the solution will be suboptimal, even with good measurements (Ryan, 2002). The second step is the update, which combines the historical data through the dynamic model, with the new information in an optimal fusion.

The state model can be expressed as a first-order differential equation:

$$\dot{x} = Fx + Gu \quad (4.4)$$

where:

$x$  is the state vector of unknown parameters,  $F$  is the dynamic matrix,  $G$  is a type of shaping filter, and  $u$  is a zero meaning Gaussian white noise.

The state-space solution for the Equation 4.4 can be written as a function of time ( $t$ ) as (Brown and Hwang, 1997):

$$x(t_{k+1}) = \Phi(t_{k+1}, t_k)x(t_k) + \int_{t_k}^{t_{k+1}} \Phi(t_{k+1}, \tau)G(\tau)u(\tau)d\tau \quad (4.5)$$

The dynamic model can be described in the following discrete form:

$$x_{k+1} = \Phi_k x_k + w_k \quad (4.6)$$

where:

$\Phi$  is the transition matrix relating  $x_k$  and  $x_{k+1}$  in the absence of a forcing function, and  $w_k$  is white noise with known system noise covariance structure.

The inverse Laplace transformation  $\{L^{-1}[f(s)]\}$  is the analytical method used to find out the transition matrix  $\Phi$  (Gelb, 1974):

$$\Phi_k = L^{-1} \left\{ [sI - F]^{-1} \right\}_{t=dt} \quad (4.7)$$

where  $I$  is an identity matrix and  $s$  is the Laplace transform parameter. The measurements can be modeled as a linear combination of the system states corrupted by measurements noise:

$$z_k = H_k x_k + e_k \quad (4.8)$$

where:

$z_k$  is the vector of measurements at time  $k$ ,  $H_k$  is design matrix relating the measurements to the system states  $x_k$ , and  $e_k$  is the measurement noise.

To apply Kalman filtering technique, two assumptions must be satisfied:

1. The system noise and the measurement noise are uncorrelated with each other and are zero mean random process, i.e.,:

$$E[w_k e_j^T] = 0 \quad \text{for all } j \text{ and } k$$

$$w_k \sim N(0, Q_k); \quad e_k \sim N(0, R_k)$$

and the covariance matrices are:

$$E[w_k w_j^T] = \begin{cases} Q_k, & k = j \\ 0, & k \neq j \end{cases}, \quad E[e_k e_j^T] = \begin{cases} R_k, & k = j \\ 0, & k \neq j \end{cases} \quad (4.9)$$

2. The initial mean value of the system state and the covariance matrix of the initial system noise are known, i.e.,:

$$\hat{x}_0 = E[x_0]; \quad P_0 = E[(x_0 - \hat{x}_0)(x_0 - \hat{x}_0)^T] \quad (4.10)$$

As mentioned earlier, Kalman filter is built on two steps; the first is the prediction step:

$$x_{k+1}^- = \Phi_{k+1,k} x_k^+ \quad (4.11)$$

$$P_{k+1}^- = \Phi_{k+1,k} P_k^+ \Phi_{k+1,k}^T + Q_k, \quad (4.12)$$

where superscript (-) and (+) signs indicate before and after measurements update, respectively.

The second step is the measurement update:

$$\text{State update: } x_{k+1}^+ = x_{k+1}^- + K_{k+1} [z_{k+1} - H_{k+1} x_{k+1}^-] \quad (4.13)$$

$$\text{Kalman gain: } K_{k+1} = P_{k+1}^- H_{k+1}^T [H_{k+1} P_{k+1}^- H_{k+1}^T + R_{k+1}]^{-1} \quad (4.14)$$

$$\text{Covariance update: } P_{k+1}^+ = [I - K_{k+1} H_{k+1}] P_{k+1}^- \quad (4.15)$$

Equations (4.11) through (4.15) comprise the Kalman filter recursive equations. It becomes clear that once the loop is entered, it can be continued ad infinitum. Figure 4.4 illustrates the Kalman filter algorithm for a linear discrete system (Brown and Hwang, 1997).

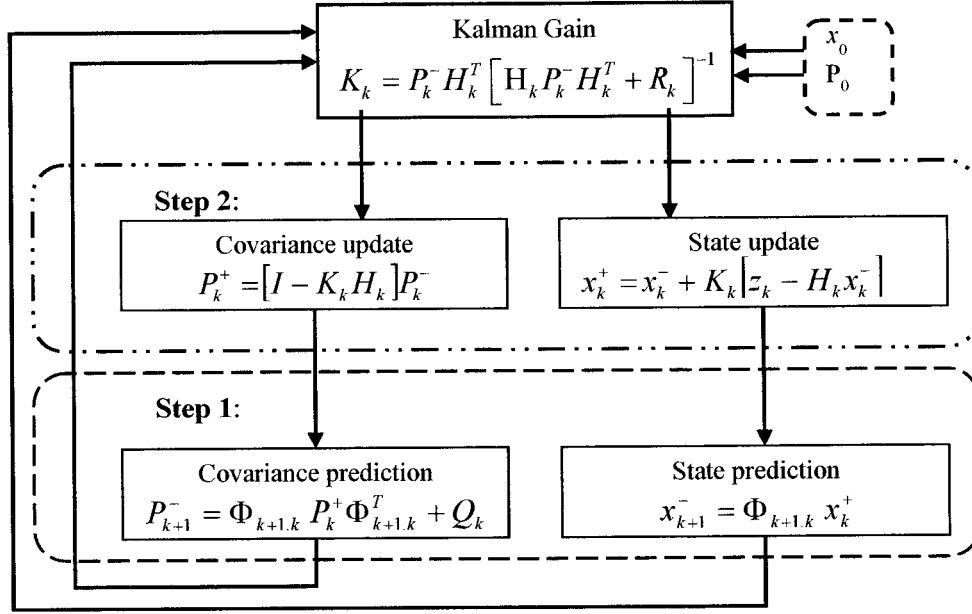


Figure 4.4 Kalman filter loop

### 4.3.2 Position Error

Generally, the DR navigation system has two sources of error. The first one comes from the velocity sensor (odometer) while the second source is from the heading sensor. The error in the estimated position is the combination of these two errors.

The output velocity is defined as:

$$\bar{v} = v + \delta v. \quad (4.16)$$

where the bar ( ) indicates variables that contain error and  $\delta v$  is the velocity error which results from the odometer scale factor error ( $dSF$ ). Equation 4.16 can be rewritten as:

$$\bar{v} = v + v.dSF = (1 + dSF)v \quad (4.17)$$

To get the velocity in the navigation frame, azimuth must be used in this transformation which corrupted by azimuth error  $\delta\psi$  as:



$$\bar{\psi} = \psi + \delta\psi \quad (4.18)$$

Transformation matrix becomes:

$$\bar{R}_B^N = \begin{bmatrix} \cos \bar{\psi} & -\sin \bar{\psi} \\ \sin \bar{\psi} & \cos \bar{\psi} \end{bmatrix} \quad (4.19)$$

where  $\bar{R}_B^N$  is the corrupted transformation matrix from the body frame to the navigation frame. Substitute  $\bar{\psi}$  from Equation (4.17) into Equation (4.19):

$$\begin{aligned} \bar{R}_B^N &= \begin{bmatrix} c(\psi + \delta\psi) & -s(\psi + \delta\psi) \\ s(\psi + \delta\psi) & c(\psi + \delta\psi) \end{bmatrix} \\ &= \begin{bmatrix} c\psi.c\delta\psi - s\psi.s\delta\psi & -s\psi.c\delta\psi - c\psi.s\delta\psi \\ s\psi.c\delta\psi + c\psi.s\delta\psi & c\psi.c\delta\psi - s\psi.s\delta\psi \end{bmatrix} \end{aligned} \quad (4.20)$$

for small  $\delta\psi$ :  $c\delta\psi \approx 1$  and  $s\delta\psi \approx \delta\psi$  and from now on  $c \equiv \cos$ ,  $s \equiv \sin$

Equation (4.20) is rewritten as:

$$\bar{R}_B^N = \begin{bmatrix} c\psi - \delta\psi s\psi & -s\psi - \delta\psi c\psi \\ s\psi + \delta\psi c\psi & c\psi - \delta\psi s\psi \end{bmatrix} \quad (4.21)$$

The corrupted velocity in the navigation frame becomes:

$$\bar{\mathbf{v}}^N = \bar{R}_B^N \bar{\mathbf{v}} \quad (4.22)$$

Substituting from equations 4.18 and 4.21 for  $\bar{\mathbf{v}}$  and  $\bar{R}_B^N$ , and writing  $\bar{\mathbf{v}}^N$  in the vector format:

$$\begin{bmatrix} \bar{\mathbf{v}}^{north} \\ \bar{\mathbf{v}}^{east} \end{bmatrix} = \begin{bmatrix} c\psi - \delta\psi s\psi & -s\psi - \delta\psi c\psi \\ s\psi + \delta\psi c\psi & c\psi - \delta\psi s\psi \end{bmatrix} \begin{bmatrix} (1 + dSF)v \\ 0 \end{bmatrix} \quad (4.23)$$

The above equation can be rewritten in a simple format after multiplication and with neglecting small elements:

$$\begin{bmatrix} \bar{v}^{north} \\ \bar{v}^{east} \end{bmatrix} = \begin{bmatrix} c\psi & -s\psi \\ s\psi & c\psi \end{bmatrix} \begin{bmatrix} v \\ 0 \end{bmatrix} + \begin{bmatrix} v.c\psi & -v.s\psi \\ v.s\psi & v.c\psi \end{bmatrix} \begin{bmatrix} dSF \\ \delta\psi \end{bmatrix} \quad (4.24)$$

The velocity error in the navigation frame can then be written as:

$$\delta v^N = \bar{v}^N - v^N \quad (4.25)$$

Substitute from Equations 4.1 and 4.24 into Equation 4.25 which will take this form:

$$\begin{bmatrix} \delta v^{north} \\ \delta v^{east} \end{bmatrix} = \begin{bmatrix} v.c\psi & -v.s\psi \\ v.s\psi & v.c\psi \end{bmatrix} \begin{bmatrix} dSF \\ \delta\psi \end{bmatrix} \quad (4.26)$$

From Equation (4.26), the horizontal error components are included in the DR navigation system are written as (Abd El-Gelil and El-Rabbany, 2003):

$$\begin{bmatrix} \delta \dot{p}^{north} \\ \delta \dot{p}^{east} \end{bmatrix} = \begin{bmatrix} \delta v^{north} \\ \delta v^{east} \end{bmatrix} = \begin{bmatrix} v.c\psi & -v.s\psi \\ v.s\psi & v.c\psi \end{bmatrix} \begin{bmatrix} dSF \\ \delta\psi \end{bmatrix} \quad (4.27)$$

where  $\delta \dot{p}^{north}$ ,  $\delta \dot{p}^{east}$  are the rate of change in the DR position error in the north and east directions, respectively.

### 4.3.3 Scale Factor Stochastic Model

The odometer scale factor is not constant because it depends on the radius of the vehicle's wheel, which changes with tire pressure, temperature, and vehicle's speed. However, the odometer scale factor can be calibrated from time to time by driving to a known distance. However, this calibration must be carried out at different speeds to get a best estimate for the scale factor. In this research, the first order Gauss-Markov process was applied to define the scale factor error as (Da and Dedes, 1995):

$$dSF = -\alpha dSF + w_{sf} \quad (4.28)$$

where  $\alpha$  is the inverse of the correlation time and  $w_{sf}$  is white noise that is introduced by the quantization error, as discussed in Chapter 2. Figure 4.5 illustrates the stochastic model for the scale factor.

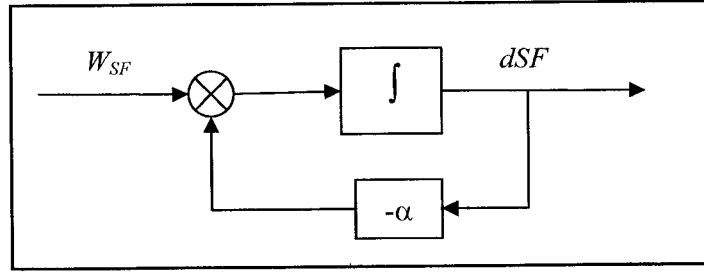


Figure 4.5 Scale factor model

#### 4.3.4 Azimuth Error and Gyro Drift

The bias offset is the apparent rotation rate when the gyro is not rotating about its sensitive axis. FOG has a temperature sensor whose output is available in digital version. In a land navigation application, the bias offset can be estimated by measuring the apparent rotation rate when the vehicle is stationary. This can be subtracted from the gyro output to yield the true rotation rate about the sensitive axis.

The noise output of the gyro sensor has to be characterized to decide on its type (e.g., white noise, random walk, or correlated). This requires the determination of the autocorrelation function. The shape of the autocorrelation function of the noise determines its type and the most appropriate stochastic model to use. To estimate the bias value and the noise characteristics, data were recorded at 10 Hz for 16 hours continuously in the static mode where there is no rotation (Figure 4.6). The autocorrelation function was computed from the raw data and plotted in Figure 4.7. It is clear that the

autocorrelation is equal to one at zero lag and almost zero for any other time delay value.

Figure 4.8 shows the accumulated error in azimuth.

The azimuth error ( $\delta\psi$ ) is attributable to gyro measurement errors. This can be quantified as the combined effect of gyro drift error ( $\delta d_{fog}$ ) and a white noise sequence ( $w_\psi$ ), which represents unmodeled errors

$$\delta\dot{\psi} = \delta d_{fog} + w_\psi \quad (4.29)$$

The random walk for gyro drift error was used successfully by Zhang (1995) and Harvey (1998), especially for low-end solid-state gyros and is confirmed by the above experiment. The differential equation for the gyro drift error can be written as:

$$\delta\dot{d}_{fog} = w_{fog} \quad (4.30)$$

Equations 4.29 and 4.30 can be conceptually presented as in Figure 4.8.

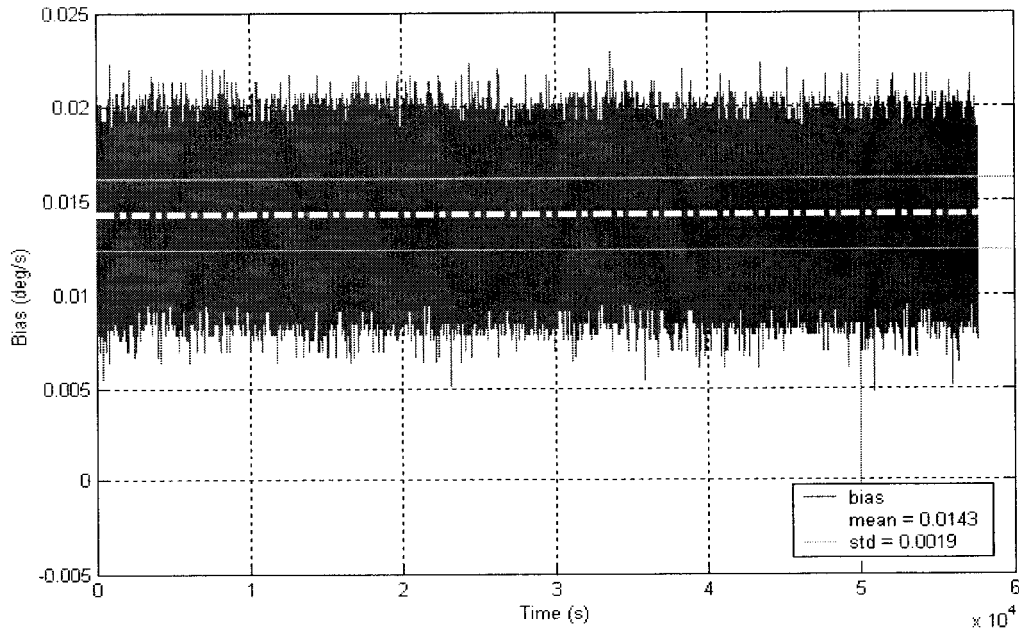


Figure 4.6 Gyro output without any external rotation

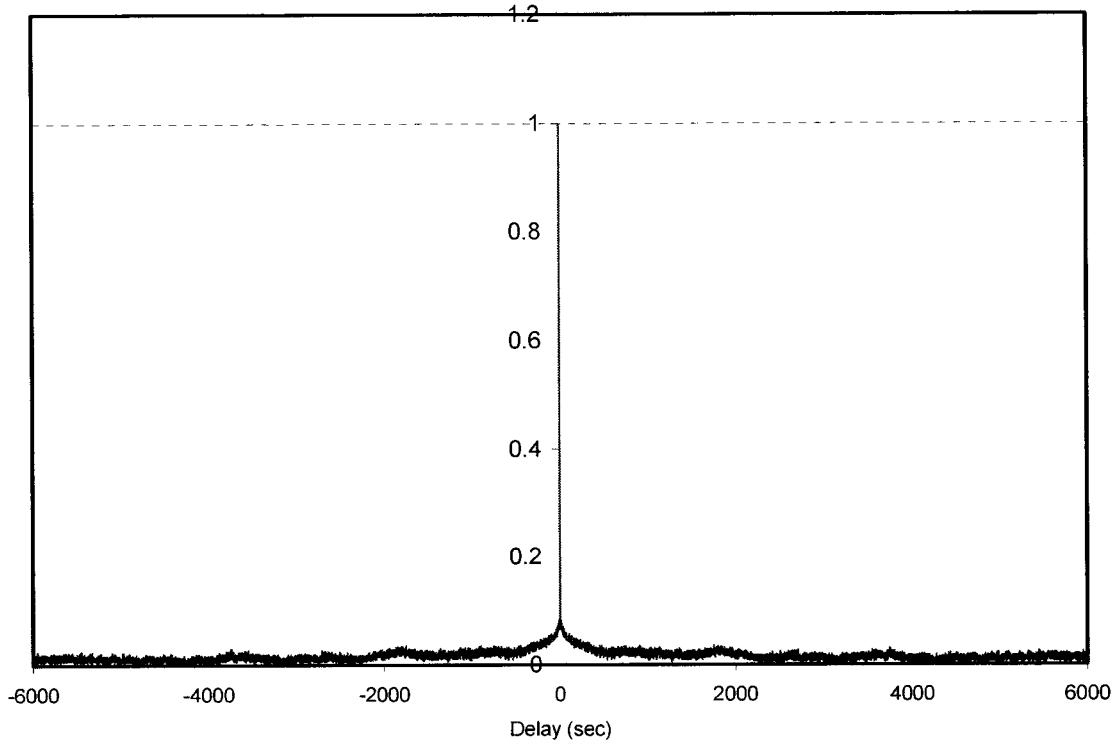


Figure 4.7 Auto-correlation function for Gyro

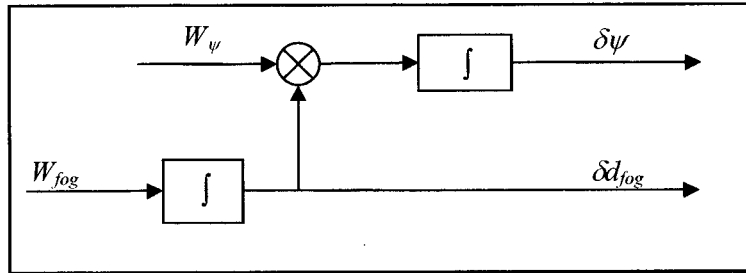


Figure 4.8 Azimuth and gyro drift error

#### 4.3.4 Kalman Filter Parameters and States

The Kalman filter estimates the error in the north and east positions, the odometer scale factor, the heading, and the gyro drift. In this case, the state vector will be composed of five states (Abd El-Gelil and El-Rabbany, 2002):

$$x = \begin{bmatrix} \delta P^{north} & \delta P^{east} & dSF & \delta \psi & \delta d_{fog} \end{bmatrix}^T \quad (4.31)$$

where  $\delta P^{north}$  and  $\delta P^{east}$  represent the errors in the north and east position respectively, and the remaining terms defined above.

From Equations 4.27 to 4.30, the final dynamic model can be represented in the matrix format as follows:

$$\begin{bmatrix} \delta \dot{P}^{north} \\ \delta \dot{P}^{east} \\ \delta \dot{SF} \\ \delta \dot{\psi} \\ \delta \dot{d}_{fog} \end{bmatrix} = \begin{bmatrix} 0 & 0 & v.c\psi & -v.s\psi & 0 \\ 0 & 0 & v.s\psi & v.c\psi & 0 \\ 0 & 0 & -\alpha & 0 & 0 \\ 0 & 0 & 0 & 0 & 1 \\ 0 & 0 & 0 & 0 & 0 \end{bmatrix} \begin{bmatrix} \delta P^{north} \\ \delta P^{east} \\ dSF \\ \delta \psi \\ \delta d_{fog} \end{bmatrix} + \begin{bmatrix} 0 \\ 0 \\ w_{sf} \\ w_{\psi} \\ w_{fog} \end{bmatrix} \quad (4.32)$$

The discrete form of the error propagation equation used to propagate estimates of the filter state from instant time  $k$  to time  $k+1$  can be calculated numerically (with the assumption that the sampling interval is relatively small, e.g., one second):

$$\Phi_k = \exp(F\Delta t) \approx I + F\Delta t \quad (4.33)$$

$$\Phi_k = \begin{bmatrix} 0 & 0 & v(c\psi)\Delta t & -v(s\psi)\Delta t & 0 \\ 0 & 0 & v(s\psi)\Delta t & v(c\psi)\Delta t & 0 \\ 0 & 0 & e^{(-\alpha\Delta t)} & 0 & 0 \\ 0 & 0 & 0 & 1 & \Delta t \\ 0 & 0 & 0 & 0 & 1 \end{bmatrix}_k \quad (4.34)$$

where all parameters are defined before. Once getting the transition matrix, the Kalman filter equation in the discrete form becomes (Rogers, 2000):

$$\begin{bmatrix} \delta P^{north} \\ \delta P^{east} \\ dSF \\ \delta \psi \\ \delta d_{fog} \end{bmatrix}_{k+1} = \begin{bmatrix} 0 & 0 & v(c\psi)\Delta t & -v(s\psi)\Delta t & 0 \\ 0 & 0 & v(s\psi)\Delta t & v(c\psi)\Delta t & 0 \\ 0 & 0 & e^{(-\alpha\Delta t)} & 0 & 0 \\ 0 & 0 & 0 & 1 & \Delta t \\ 0 & 0 & 0 & 0 & 1 \end{bmatrix}_k \begin{bmatrix} \delta P^{north} \\ \delta P^{east} \\ dSF \\ \delta \psi \\ \delta d_{fog} \end{bmatrix}_k + \begin{bmatrix} 0 \\ 0 \\ w_{sf} \\ w_{\psi} \\ w_{fog} \end{bmatrix}_k \quad (4.35)$$

To complete the Kalman filter design, the observation must be defined, which will update the filter. In this case, the position errors in the north and east directions are estimated as the difference between the DR and the GPS and/or Signpost solution:

$$\begin{bmatrix} \Delta^n \\ \Delta^e \end{bmatrix} = \begin{bmatrix} \frac{1}{R_M + h} & 0 \\ 0 & \frac{1}{(R_N + h)\cos \phi_m} \end{bmatrix} \begin{bmatrix} \phi_{GPS/SP} - \phi_{DR} \\ \lambda_{GPS/SP} - \lambda_{DR} \end{bmatrix} \quad (4.36)$$

The design matrix  $H$  in Equation 4.8 for the position error update based on Equation 4.36 becomes:

$$H = \begin{bmatrix} 1 & 0 & 0 & 0 & 0 \\ 0 & 1 & 0 & 0 & 0 \end{bmatrix} \quad (4.37)$$

The process noise matrix ( $Q_k$ ) can be defined by knowing the transition matrix  $\Phi$  and the spectrum density matrix ( $q_k$ ) as follows (Gelb, 1974):

$$Q_k = \int_0^{\Delta t} \Phi(t_{k+1}, \xi) q_k \Phi(t_{k+1}, \eta) d\xi \quad (4.38)$$

This is a rank 5 square matrix whose elements are given by:

$$\begin{aligned} Q(1,1) &= q(1,1)\Delta t + \frac{v^2(c\Psi)^2(\Delta t)^3}{3}q(3,3) + \frac{v^2(s\Psi)^2(\Delta t)^3}{3}q(4,4) \\ Q(1,2) &= Q(2,1) = \frac{v^2(c\Psi)(s\Psi)(\Delta t)^3}{3}q(3,3) - \frac{v^2(c\Psi)(s\Psi)(\Delta t)^3}{3}q(4,4) \\ Q(1,3) &= Q(3,1) = \frac{v(c\Psi)\exp(-\alpha\Delta t)}{-\alpha}q(3,3) \\ Q(1,4) &= Q(4,1) = \frac{-v(s\Psi)(\Delta t)^2}{2}q(4,4) \\ Q(1,5) &= Q(5,1) = Q(2,5) = Q(5,2) = Q(3,4) = Q(4,3) = Q(3,5) = Q(5,3) = 0 \end{aligned}$$

$$Q(2,2) = q(2,2)\Delta t + \frac{v^2(s\Psi)^2(\Delta t)^3}{3}q(3,3) + \frac{v^2(c\Psi)^2(\Delta t)^3}{3}q(4,4)$$

$$Q(2,3) = Q(3,2) = -\frac{v(s\Psi)\exp(-\alpha\Delta t)}{\alpha}q(3,3)$$

$$Q(2,4) = Q(4,2) = \frac{v(c\Psi)(\Delta t)^2}{2}q(4,4)$$

$$Q(3,3) = \frac{(1-\exp(-2\alpha\Delta t))}{2\alpha}q(3,3)$$

$$Q(4,4) = q(4,4)\Delta t + \frac{(\Delta t)^3}{3}q(5,5)$$

$$Q(4,5) = Q(5,4) = \frac{(\Delta t)^2}{2}q(5,5)$$

$$Q(5,5) = q(5,5)\Delta t$$

The most difficult task in the implementation of Kalman filter is in the selection of the filter parameters which depends on the characteristic of the system noise (Table 4.1). In general, this is an empirical process known as tuning, wherein the various parameters are chosen to optimally estimate the state of the system while accurately reflecting the true state error in the covariance and avoiding divergence.

Table 4.1 Kalman filter parameters

States	Correlation time	Spectral densities
Scale factor	$\alpha^{-1} = 20000 \text{ s}$	$q(3,3) = 1 \times 10^{-8} (\text{m/pluse})^2/\text{s}$
Azimuth	-	$q(4,4) = 5 \times 10^{-4} (\text{rad})^2/\text{s}$
Gyro	-	$q(5,5) = 9.5 \times 10^{-11} (\text{rad/s})^2/\text{s}$



## **CHAPTER 5**

### **EXPERIMENTAL WORK AND RESULTS ANALYSIS**

The main objectives of the experimental work are to verify the system hardware, to evaluate the developed computer program, and to assess the system performance. Three field tests were conducted to satisfy these objectives. The first two tests were carried out in an open area, where obstructions to GPS signals were not present. A third test was done under high masking conditions in Toronto's downtown core. This chapter describes the DR sensors which were installed in a private car, in addition to the GPS receiver. After the description and classification of the hardware, a MatLab program was written to deal with the sensors' outputs. At the end of this chapter, a description of field tests is presented in detail. The test results are then analyzed and the achieved system performance is evaluated.

#### **5.1 SENSORS DESCRIPTION**

The integrated system used in this research consisted of three different types of sensors, namely, GPS receivers, a Fiber Optic Gyro E-Core 1000 KVH™, and odometer. The signpost measurements were introduced from differential GPS measurements. The main positioning system is the DR (Gyro and odometer). The combination of DR and signpost sensors is done to assess the current system and to assess the developed system in the absence of GPS signals. In the next section, sensors specifications, as well as the system design, are presented. Furthermore, the system realization and hardware and software modification are illustrated.

## 5.1.1 Dead Reckoning Sensors

### 5.1.1.1 KVH E-Core 1000 Fiber Optic Gyro

The E-Core 1000 is a low-cost, single-axis, fiber optic gyro. It is an angular rate sensor, which was designed and built by KVH<sup>TM</sup> (Figure 5.1). Like other fiber optic gyros, E-Core 1000 consists of a coil made from fiber and a coherent light source, the beam of which is passed through a splitter and then directed through either end of the fiber optic coil. The specifications for the gyro are given in the KVH<sup>TM</sup> Technical Manual (KVH Industries, Inc. 1999) and are summarized in Table 5.1. There are two types available for E-Core 1000. The first is RA1100 with analog output, and the second is RD1100 with digital output. For this research, the digital one is used to avoid the use of A/D converter.

The KVH RD1100 gyro has good short-term stability but suffers from bias drift, which makes it unsuitable for long-term azimuth determination. Other problems associated with the gyro include errors due to the gyro being misaligned with respect to the local level plane (refers to east, north, and down directions).

The gyro outputs one message containing an eight-byte data packet every 0.1 second in RS-232 format at 9600 baud rate with no parity. The angle rotation rate is obtained from the last two bytes, and the full-scale gyro output represents  $\pm 100$  deg/s angular velocity when one second of data is integrated. Internal gyro temperature is transmitted every two messages with a least significant bit of  $0.05^{\circ}\text{C}$  and zero out equals  $0^{\circ}\text{C}$ . The rest of the gyro outputs are the serial number and the CHECKSUM, etc. (KVH Industries, Inc. 1999). The nominal scale factor for a 16-bit quantization and a maximum rate of  $\pm 100$  deg/s is  $0.00305$  [deg/s]/bit.

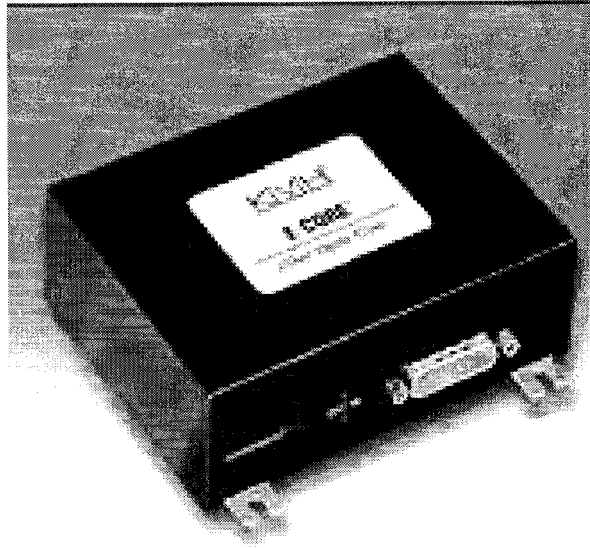


Figure 5.1 E-Core 1000 Fiber Optic Gyro (KVH™ RD1100)

Table 5.1 KVH E-Core 1000 Fiber Optic Gyro specifications

	Attribute	Specifications
Performance	Input rotation rate	to $\pm 100$ deg/s max.
	<b>Angle random walk</b>	
	Deg/hr/rt-Hz	20
	Deg/rt-hr	0.33
	<b>Bias stability</b>	
	Fixed temperature	2-4 °/hr , 1 sigma
	Full temperature	0.4°/s peak to peak
Physical	<b>Scale factor Linearity</b>	
	Constant temperature	< 0.5%
	Full temperature	< 2% RMS
	Dimension	115mm x 90mm x 41 mm excluding connector
	Weight	250 gm
Interface	Operating temperature	-40°C to +75°C
	Storage temperature	-50°C to +85°C
	Power (transient and reverse polarity protected)	+9 to +18 VDC (12 V nominal); 3W
	Sensor output	RS 232
	Connector	15-pin subminiature D-sub (DA15P)

#### *5.1.1.2 Wheel Sensor*

A private car was used in this research. The vehicle wiring diagram was studied to locate the odometer/speed signal before making any connections. The odometer signal was examined using an oscilloscope to determine if the signal type is analog or digital. Vehicle odometers generally fall into one of three categories: digital, analog, or mechanical. Digital Signals are square wave signals, usually from 0 to the vehicle's positive battery voltage (12 Volts). The pulse frequency is proportional to the vehicle speed. Analog signals are approximately sinusoidal or triangular signals, where both the frequency and amplitude increase proportionally to the vehicle speed. The mechanical odometer requires a speedometer service technician to install a Hall-effect transducer in the odometer cable line.

Reverse motion is detected externally by a connection to the back-up light wire, and an attribute is added in the output file. As discussed earlier, the scale factor changes over time, so before testing, a known distance was measured at various speeds. To get the scale factor, the number of pulses recorded must be divided by the traveled distance. The installed odometer gives 2475 pulses/km, which translates to 0.404 m/pulse.

#### **5.1.2 Dead Reckoning Interface and Time Tag**

Two modifications are done in the DR system. The first is related to the connection interface, and the second is in the data logging software. The output of FOG consists of the incremental 10 Hz angular rate at 9600 Baud rate on an RS232 interface. The interface cable for the FOG is non-standard, requiring 12 V power, which have to be constructed to ensure proper operation. The FOG interface cable use a subminiature DA-

15P connector at the sensor with a non-standard wiring pin. This interface cable is constructed to connect the gyro, power supply, and computer as illustrated in Figure 5.2.

KVH RD1100 FOG unit provides the means to convert the back motion indicator's voltage levels and the odometer pulse waveform, and combines these sensors' outputs, with its internal rate gyro's outputs, into a RS232 data output message structure. To get the odometer data, pin-13 must be connected to the odometer signal wire, pin-14 to the back-up light wire, and pin-2 to the odometer ground.

Synchronization is the most important task for different data streams. Since there was more than one sensor used in this research, the synchronization problem was solved first. Various suggestions were studied to solve this problem. The first suggestion was that the 1PPS from GPS receiver could be connected to FOG; in this case, pulses and messages could be sent through GPS to FOG. Unfortunately, the FOG can not receive messages from other sensors. The second solution was to use the PC clock. As the time tag is not part of the FOG output message, the Nlogd software was modified to get the time from the PC. However, the PC clock was not precise enough: it drifts over time, and it has different time references. To fix PC clock another GPS receiver was used to adjust the PC clock every 1 min with neglecting its position solution.

### **5.1.3 G8 Ashtech Receiver**

Ashtech's G8 is a small, high-performance GPS receiver module designed for OEMs and system integrators (Figure 5.3). Its operation is adapted to navigation, fleet management, and mobile consumer applications such as vehicle tracking, mobile data, car navigation, telematics, and handheld computing. Table 5.2 lists the most important technical specifications for G8 OEM (Magellan Corp., 1998).

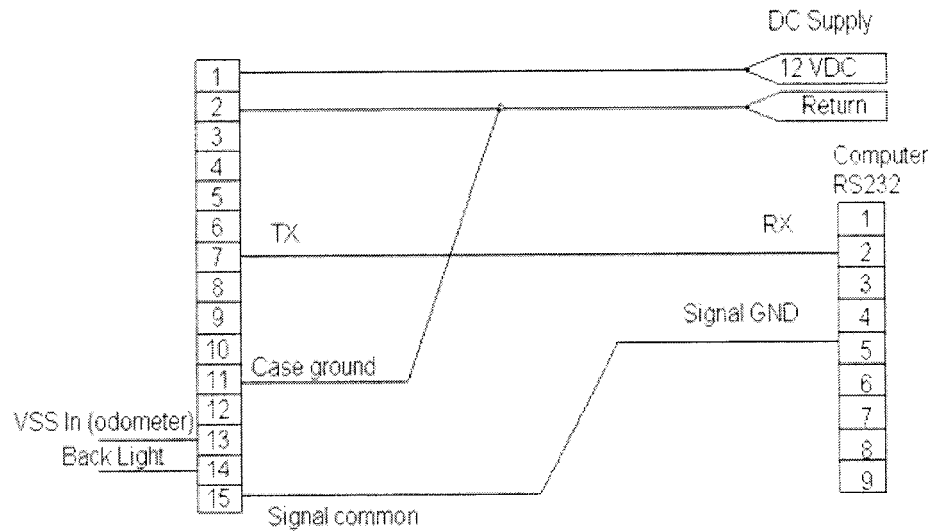


Figure 5.2 DR Wiring Diagram

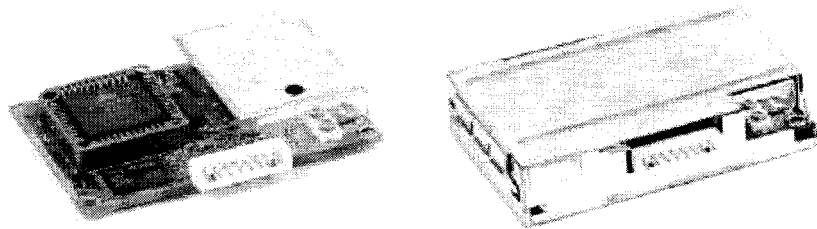


Figure 5.3 G8 OEM board and Housing (Magellan Corp., 1998)

Table 5.2 Technical specifications for G8 receiver

Attribute	Specifications
General	8-channel continuous tracking OEM GPS receiver board
GPS parameters	L1 frequency, C/A code (SPS)
Update rate	1 Hz
Communication interface	NMEA 0183 V2.1 using standard Ashtech command set
Baud rate	From 300 bps to 19200 bps (software selectable)
Size	40x61x13 mm (with mechanical shield case)
Weight	45.4 gr
Receiver noise figure	< 7 dB typical without antenna
Operating Temperature	-30°C to +80°C
Storage Temperature	-40°C to +85°C
I/O interface	TTL levels

## 5.2 HARDWARE ARCHITECTURE

The system architecture is shown in Figure 5.4. Two GPS receivers are used, one for positioning and the other for synchronization. The GPS positioning receiver gives the autonomous positioning solution in latitude, longitude, and height in the NMEA format. Since more than two serial ports were needed, but the laptop computer has only one, then a PCMCIA 232/4 multi-serial port from National Instrument is installed to provide four additional serial ports. A power supply wire was constructed to feed three sensors and the computer with DC from the car cigarette lighter. For the sake of completeness, the precise coordinates from differential GPS were used to make up the signpost measurements, which surveyed in separate day.

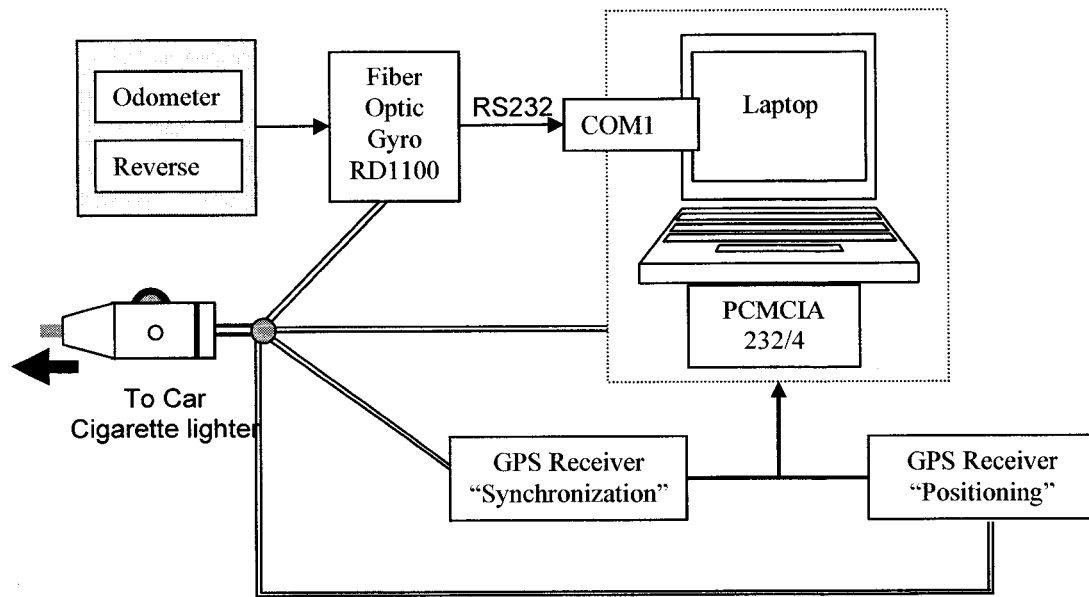


Figure 5.4 The integrated system architecture

## 5.3 DESCRIPTION OF SOFTWARE

A MatLab program is written specifically for this research; however, it can be generalized with little modifications. This program offers four different options. The first

one is the DR stand-alone which needs the user interface to input the initial position (start point) and the initial azimuth. Then applying Equations 2.1 and 2.2 the vehicle's coordinates can be obtained. However, this program can be used for different sensors by changing the input parameters, namely the odometer and the gyro scale factors which can be obtained by system calibration. The second option is the conventional positioning system (DR/signpost). It is similar to the previous option with minor differences. For this option the initial position can be obtained from the signpost data file and the vehicle's location is updated wherever the signpost exists.

The last two options have much in common (Figure 5.5). They are designed and written for the DR/GPS/signpost integrated system based on the Kalman filtering technique described in the previous chapter with five states. The parameters of Kalman filter shown in Table (4.1) are used by the program as default values. It is divided into four different cases (sub-options) to deal with the data availability. The first case is the optimal one where the position is available from all sensors (DR/GPS/signpost). The second case is in between signposts locations with GPS data available. The third case where there is no GPS data but signpost is available (conventional system). The fourth case is the DR stand-alone where no aiding system is available. Kalman filter is used in the prediction step only, as there are no measurements to update the filter.

It is worth mentioning here that the difference between the third and the fourth option is the third option is written for open area and the GPS solution is blocked artificially using attribution (0 and 1). But in the fourth option, the GPS solution is rejected if the number of satellites is less than 4.



The input files to this program are the DR data file obtained from the FOG E-Core 1000, the GPS data file including the point positioning and the number of satellites, and the signpost data file which obtained from the DGPS measurements. The output file for all options contains the vehicle location accompanied by the time stamp.

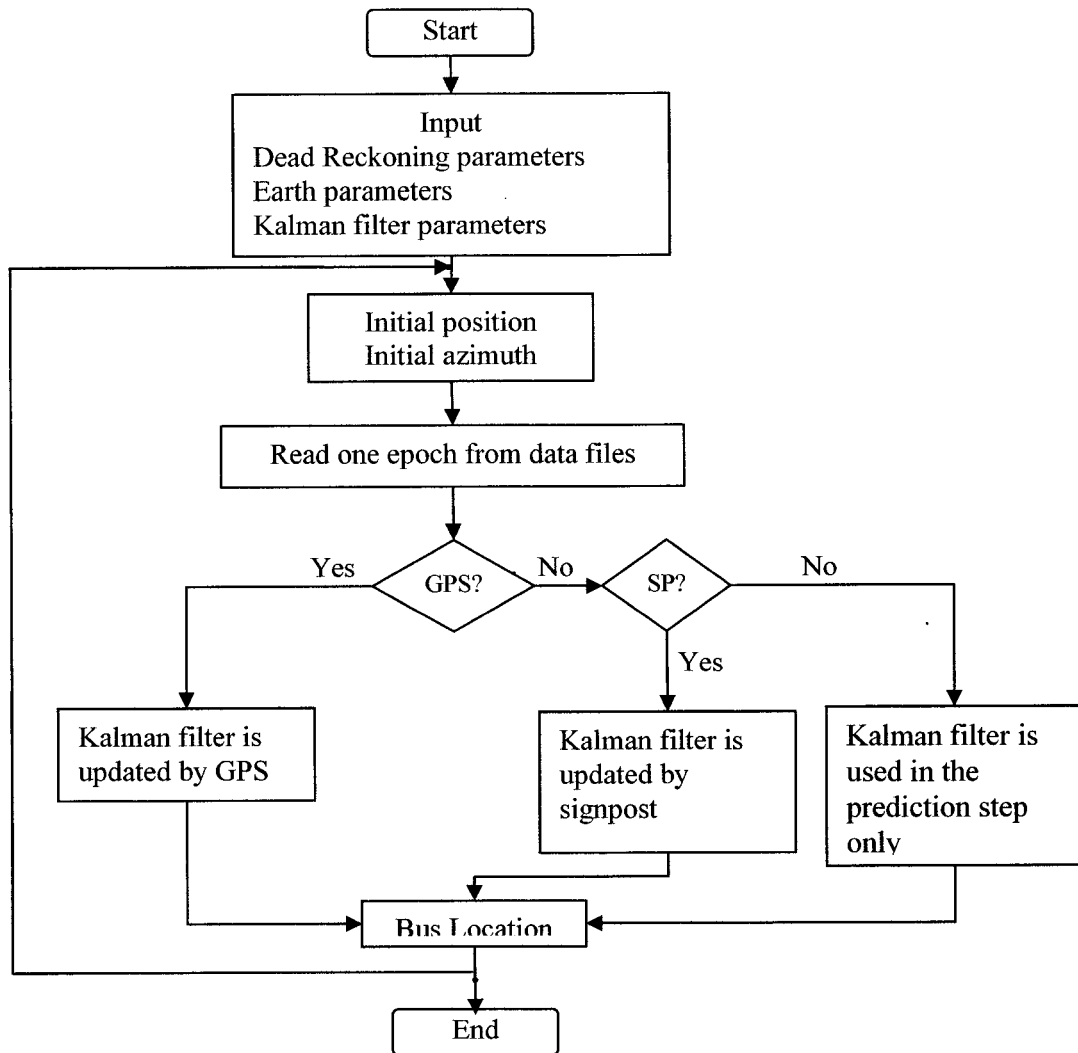


Figure 5.5 Flowchart diagram of the integrated positioning system

## 5.4 TEST DESCRIPTION

The first two field tests were carried out in the Mississauga area, west of Toronto, in August 2002. This area has low-rise buildings. To emulate the real situation, we followed

portions of two particular bus routes. These two routes contain at least 16 bus stops, either for regular or express bus services (Figure 5.6). A private car was used in all field tests. The car stopped at every bus stop for approximately 20 seconds, which is considered the average stop time for a bus. The coordinates of the bus stops were precisely determined using differential GPS on another day, and these coordinates were selected to represent the locations of the signposts.

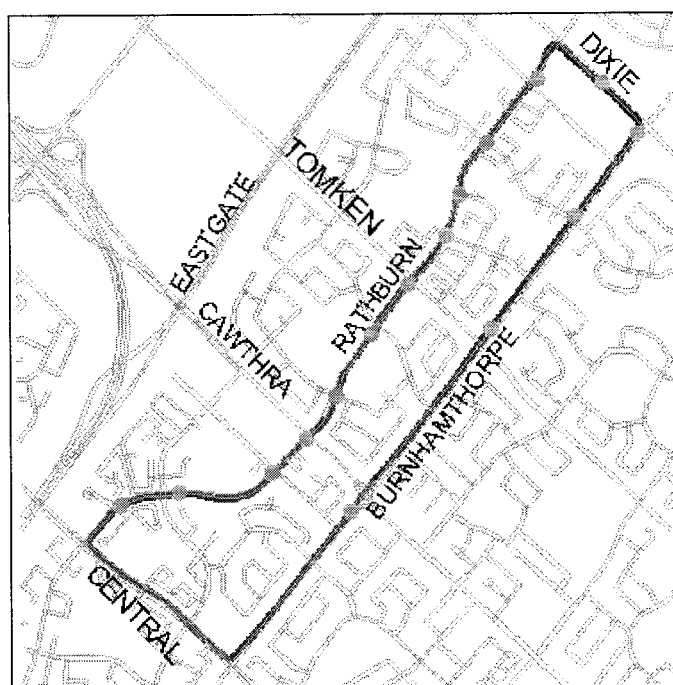


Figure 5.6 Actual trajectory of test and bus stop location

#### 5.4.1 Test One

In test one; the actual bus stops were not followed exactly; only five stops were considered, as it was very difficult to stop for 20 seconds on a weekday. This test was done on August 16, 2002 for duration of about 34 minutes. Three closed loops were done during this time period. The number of visible satellites above  $10^\circ$  elevation mask is shown in Figure 5.7. The GPS receiver is eight channels, so the maximum number of

satellites is 8. This area is open sky without any GPS signal obstructions. Eight satellites were observed 77.9% of the test time, and during 21.0% of the test time, only 7 satellites were observed. Horizontal Dilution Of Precision (HDOP), which gives an indication about the dilution in the horizontal coordinates, is plotted in Figure 5.8. The vehicle's azimuth during the test is shown in Figure 5.9. Three scenarios were investigated for this test: the DR system alone, the DR/signpost, and GPS/DR/signpost integrated system. To test the DR system alone, initial position and initial azimuth are assumed to be completely known. The second scenario applied the conventional system solution (DR/Signpost). Finally, the integrated system for all the available data was applied without any GPS outages in this case, and the initial position was obtained from the GPS measurements.

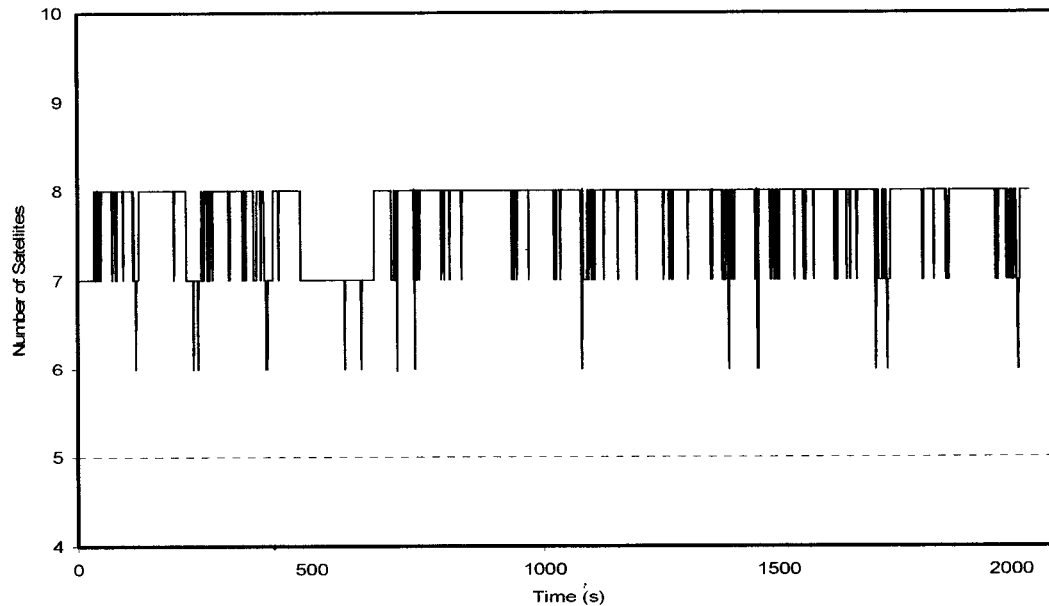


Figure 5.7 Number of Satellites observed during Test One

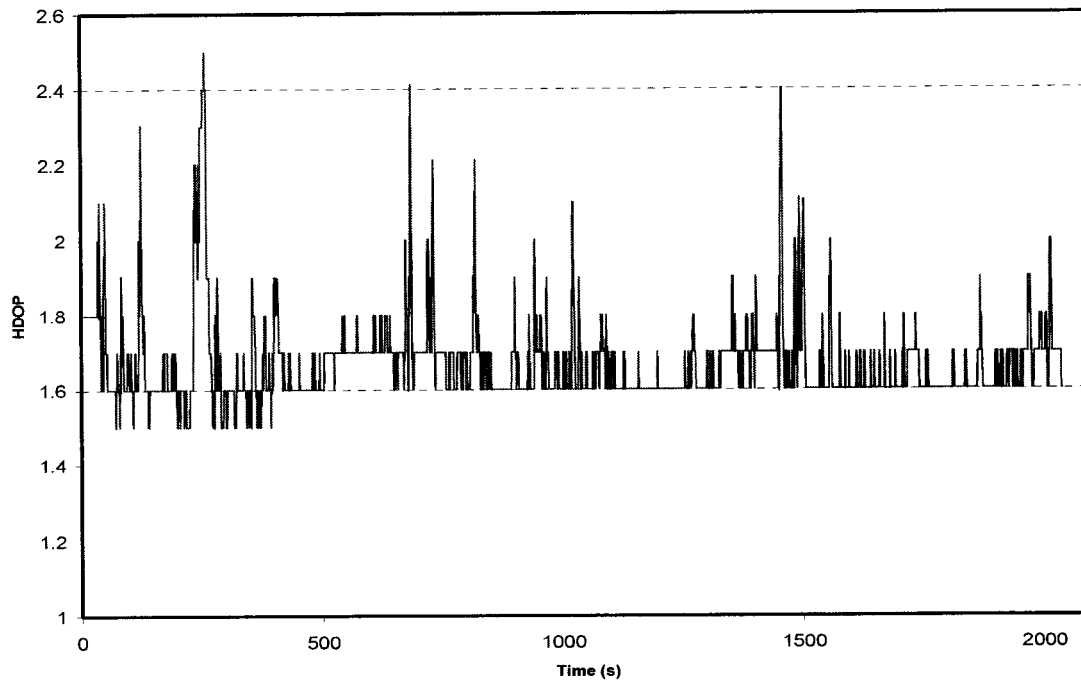


Figure 5.8 HDOP during Test One

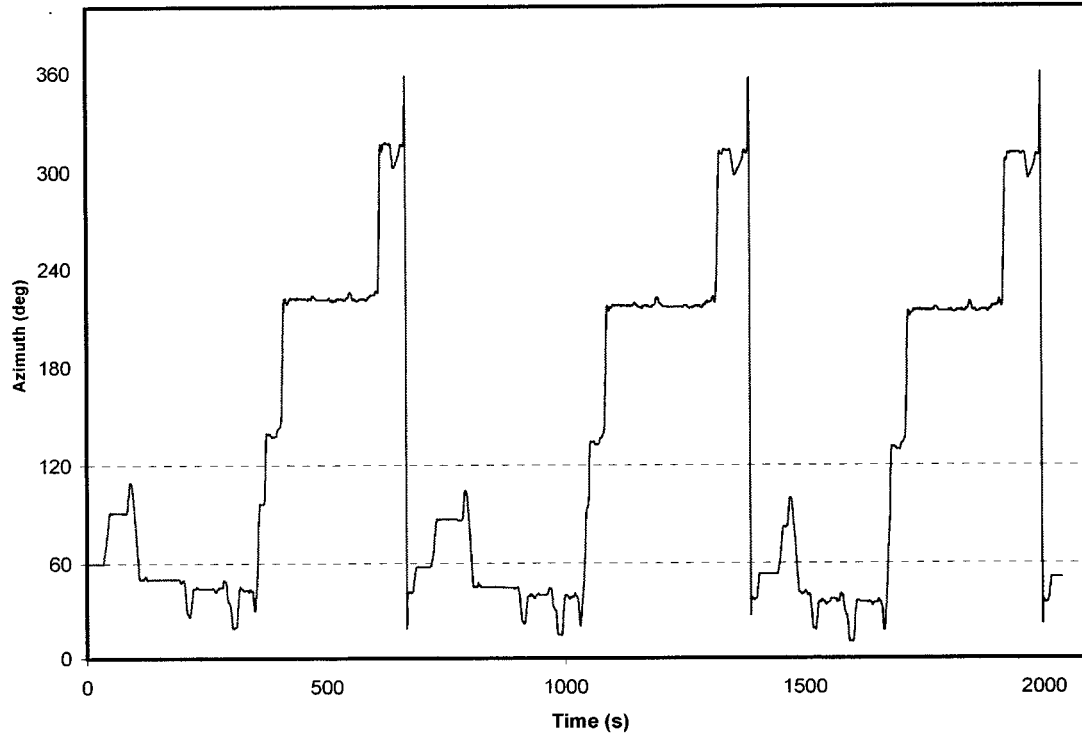


Figure 5.9 Azimuth angle during Test One

#### 5.4.1.1 The DR System Alone

In this case, the gyro and odometer measurements are combined to get the relative position, referred to as the initial azimuth and the initial coordinates. Figure 5.10 shows the errors in the north and east directions, which are obtained by comparing the DR system solution to the differential GPS. The latter is assumed to be error free. It can be seen that the solution drifts with time and distance. The maximum deviation in this case is 231.0 m and 202.0 m in the north and east directions, respectively. The same DR solution is overlaid on the street digital map in Figure 5.11. However, when the vehicle changes its direction, some errors cancel out as a result of the direction change. If the test would be carried out on the straight road without any turns, the DR error will be noticeable.

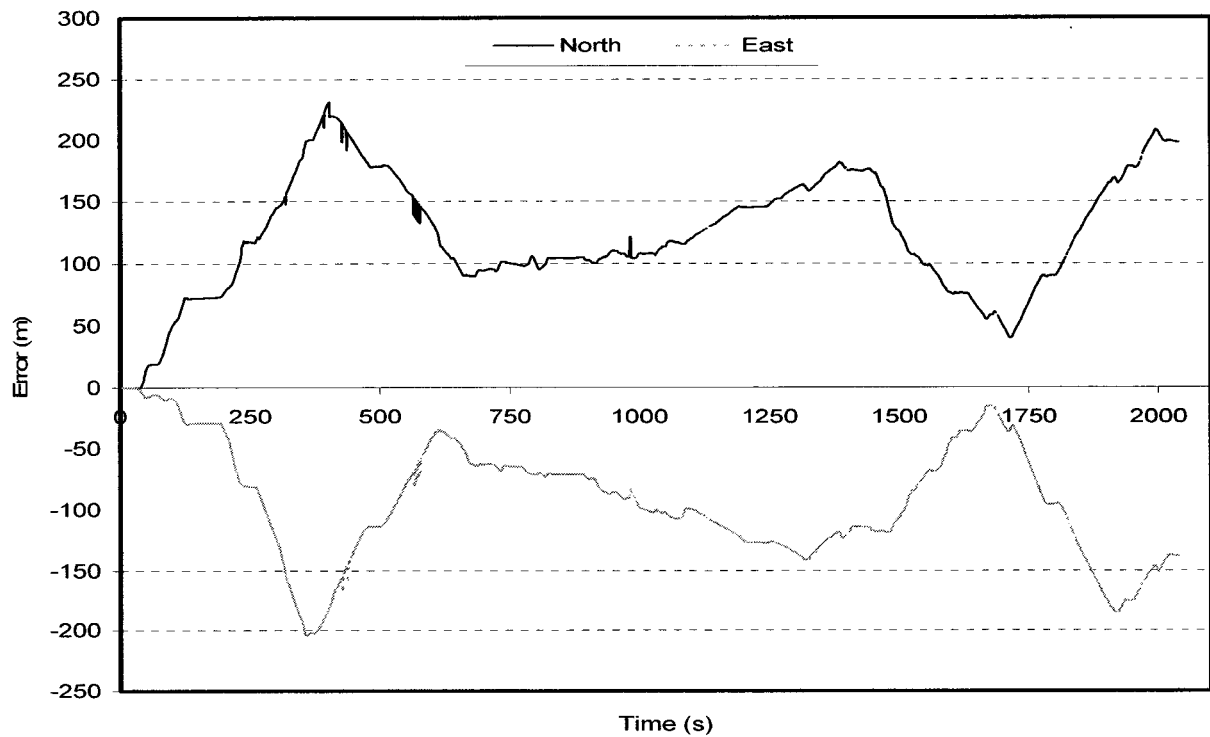


Figure 5.10 DR System with known initial azimuth and start point (Test One)

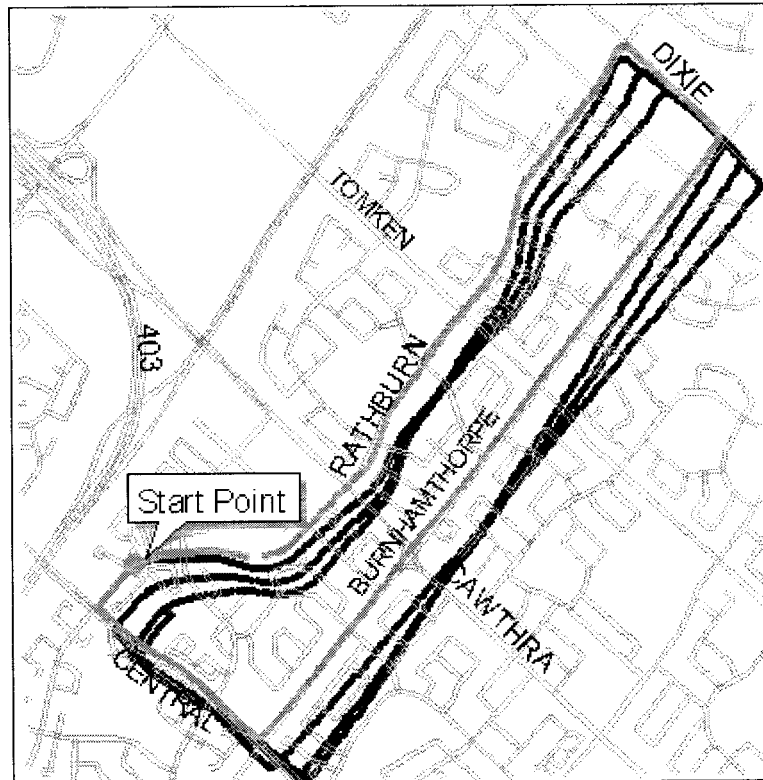


Figure 5.11 Solution of DR System alone (Test One)

#### 5.4.1.2 The DR/Signpost Solution

The main objective of this scenario is to assess the performance of the current TTC DR/signpost system. As before, the initial position and initial azimuth were provided to the DR system. In addition, the system was provided with the accurate position at 5 simulated signpost locations (Figure 5.12). It can be seen that the DR/signpost system provided a better solution than DR alone because the system is updated at every signpost with the accurate position. Figure 5.13 also shows that the solution becomes poor when the distances between the signposts increase.

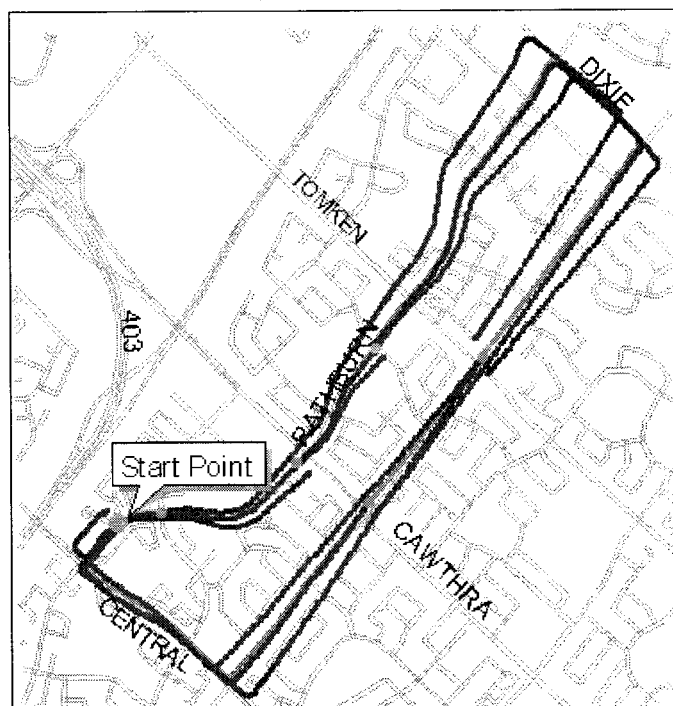


Figure 5.12 The DR/Signpost solution (Test One)

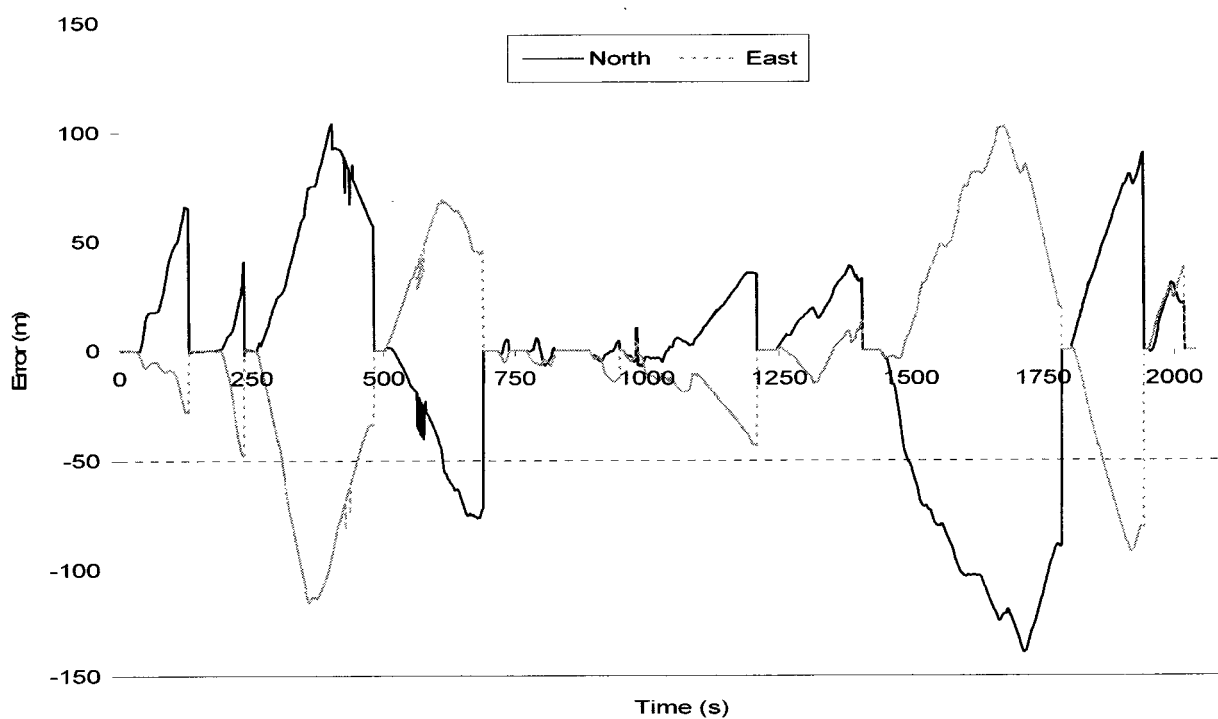


Figure 5.13 The DR/Signpost errors (Test One)

#### 5.4.1.3 GPS/DR/Signpost integrated System

The final scenario for this data set was to study the integrated system with GPS without any GPS outages. Figure 5.14 shows the solution for the integrated system. There is no difference between this solution and the digital map in the background. The results are also very close to the differential GPS solution.

#### 5.4.2 Test Two

This test was conducted on August 17, 2002 when there was no heavy traffic. Hence, we were able to stop at every bus stop for an average of 20 seconds and to stop at the start point for 2 minutes to estimate the gyro offset. The above scenarios were investigated in this test; in addition the GPS outages were simulated by rejecting the GPS data for 100 seconds continuously.

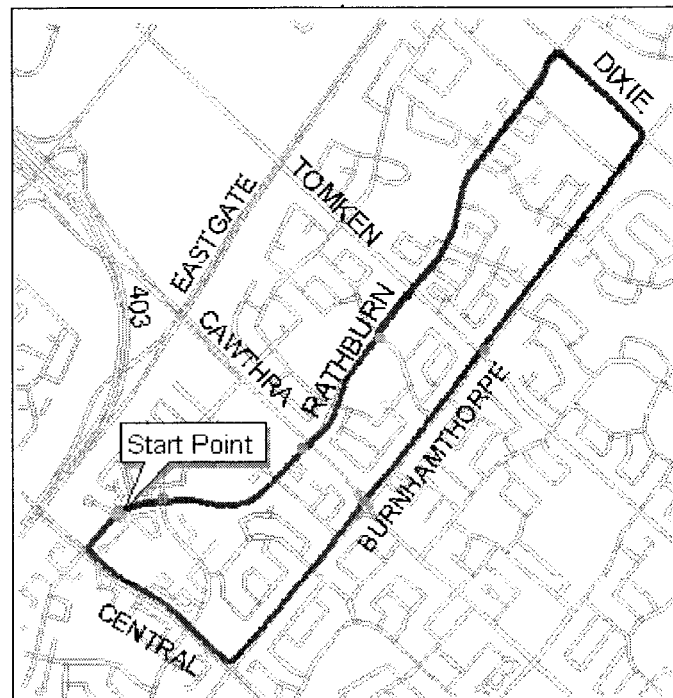


Figure 5.14 GPS/DR/Signpost integrated system (Test One)



#### 5.4.2.1 The DR System Alone

The results of this test are better than during Test One because we could stop at every stop for an average of 20 seconds, which improved the DR system solution (Figure 5.15, 5.16). This means that the gyro offset was estimated at every stop to control the drift. However, there is no differential GPS available from (180-365 second), so there is no reference data to compare in that period.

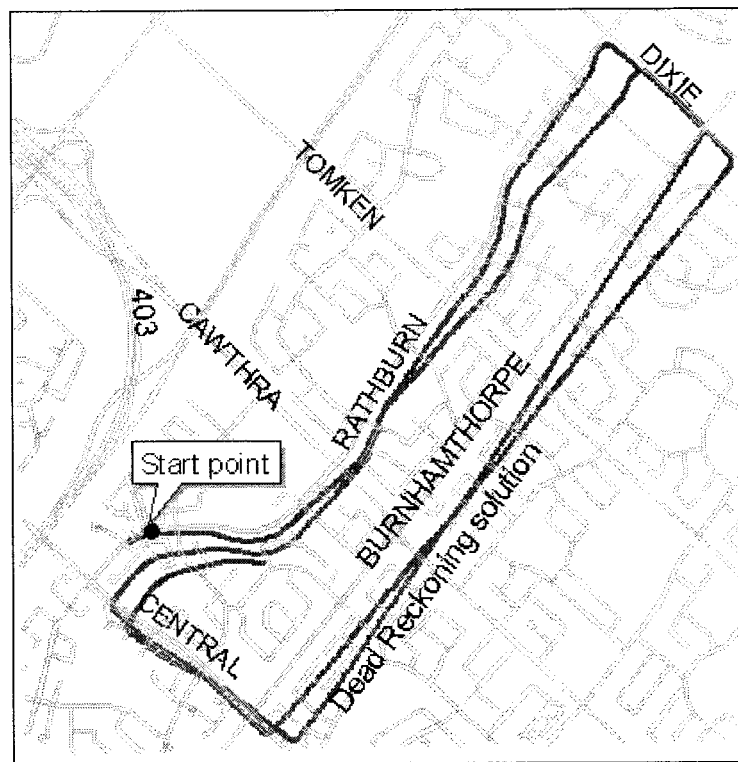


Figure 5.15 DR system alone (Test Two)

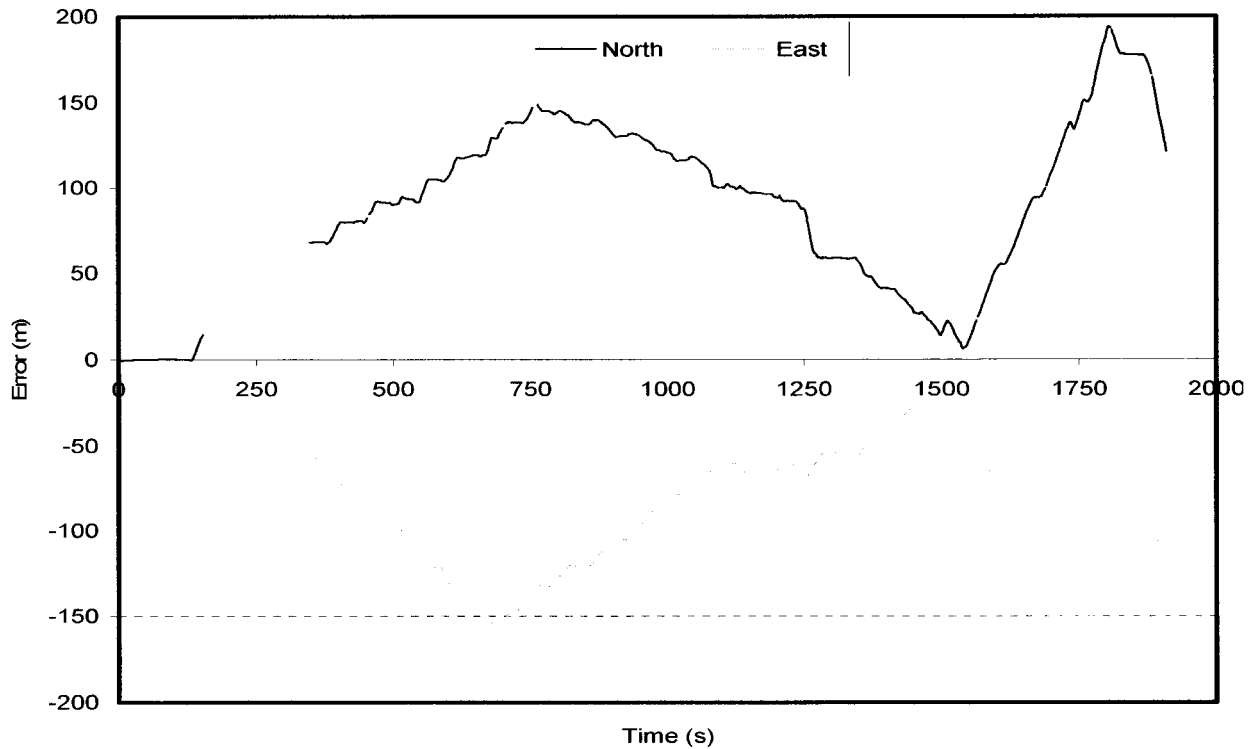


Figure 5.16 DR System with known initial azimuth and start point (Test Two)

#### 5.4.2.2 The DR/Signpost Solution

Following the actual bus stops improved the solution, as shown in Figure 5.17 and Figure 5.18. The most significant improvement is noticed in the first period (from 0 to 1200 second). In this period, several stops were conducted, which gave the system time to update its position and the gyro offset. This means that the system can be reliable with good signpost coverage in the bus route, which implies a high cost for signpost power supply and maintenance. However, in the second round, there were no more stops, which affected the obtained solution with maximum deviations of 135.0 m and 120.0 m in the north and east directions, respectively.

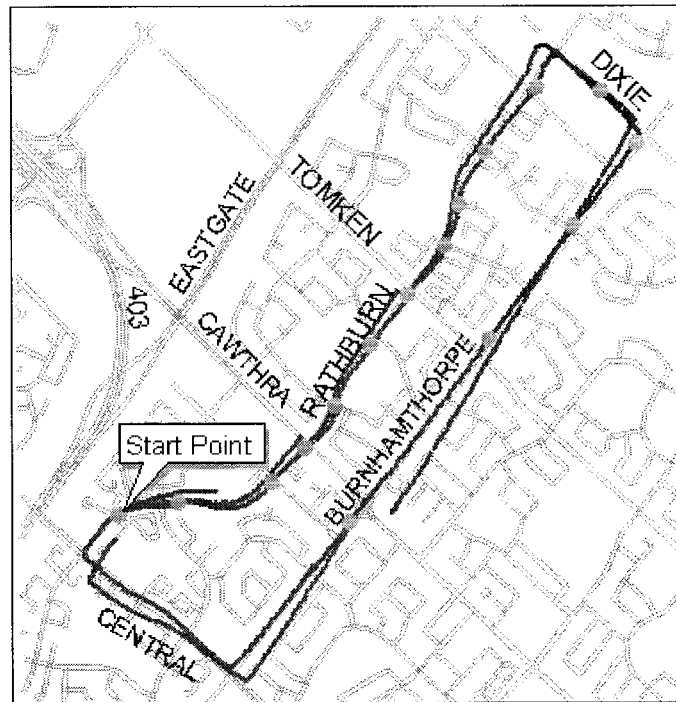


Figure 5.17 The DR/Signpost solution (Test Two)

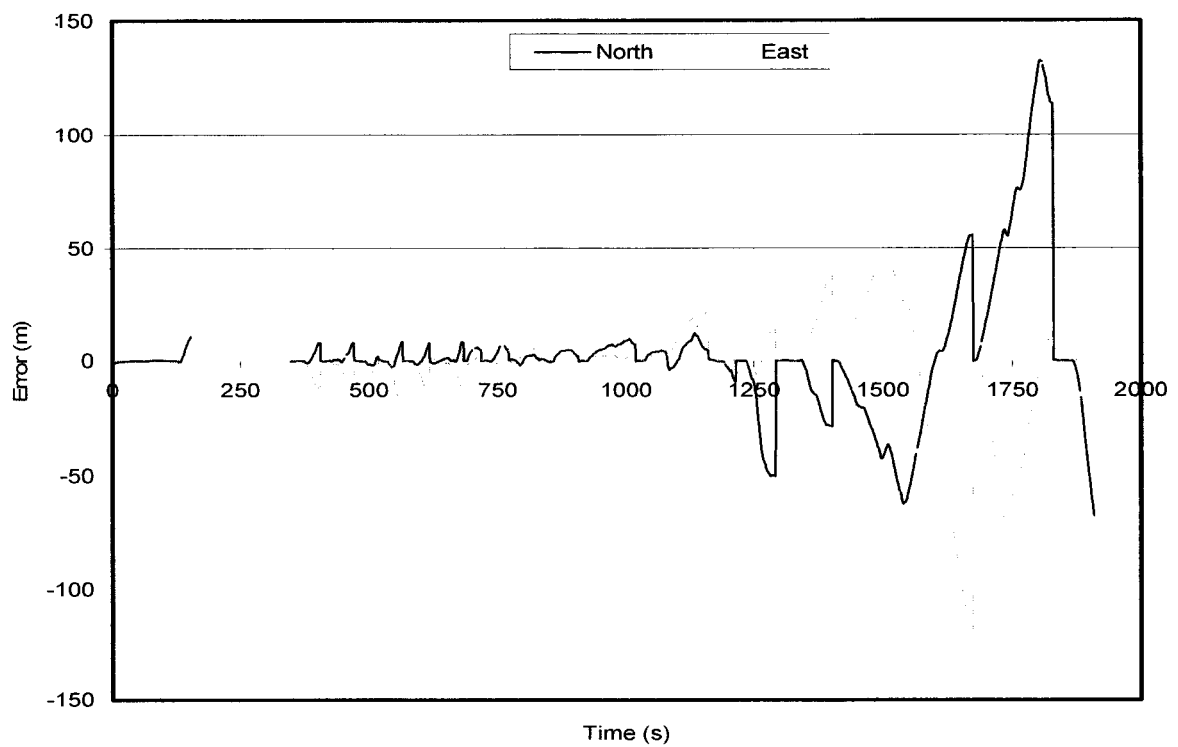


Figure 5.18 The DR/signpost system errors (Test Two)

#### 5.4.2.3 The DR/GPS Solution

Signposts may be malfunctioned as a result of e.g. power outages. In that case, the bus location can be obtained from DR/GPS integrated system. Figure 5.19 shows the DR/GPS solution without signpost update and with GPS outages for 100 s (top of the figure). The obtained solution is accurate and the maximum deviations in the north and east directions are 19.0 m and 37.0 m, respectively.

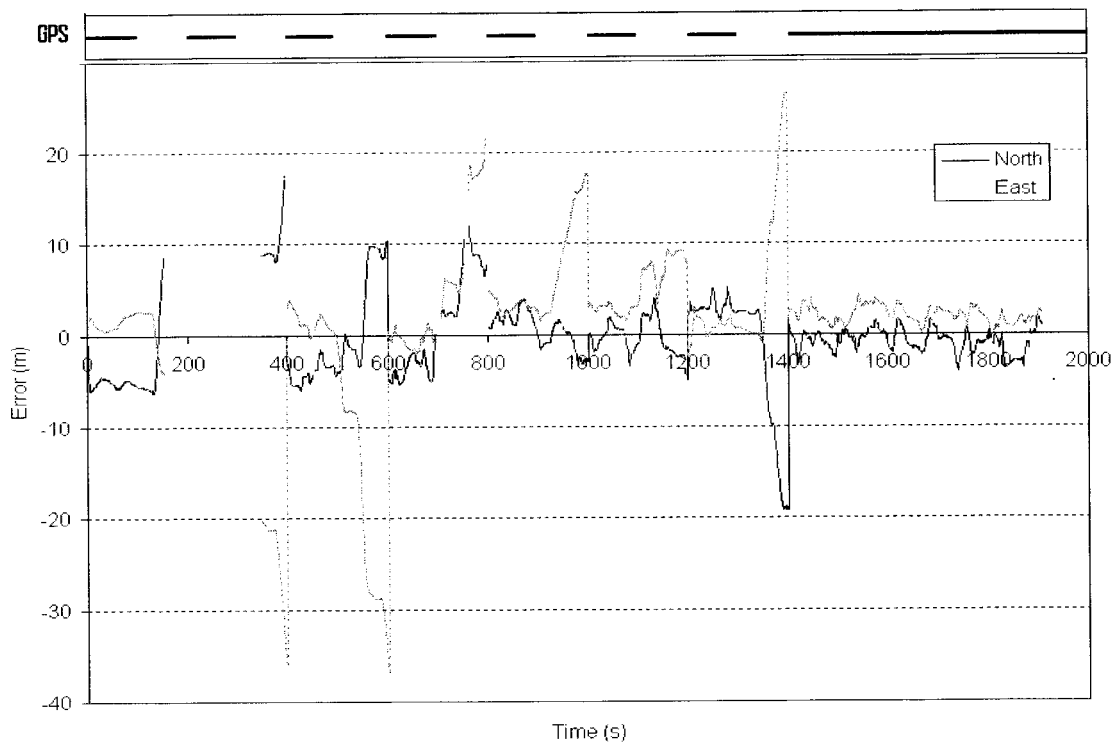


Figure 5.19 DR/ GPS error for 100 seconds GPS outages (Test Two)

#### 5.4.2.4 GPS/DR/Signpost integrated System with GPS outages

Figure 5.20 shows the integrated system solution with GPS signals blocked for 100s sequentially. Figure 5.21 shows the periods when GPS was available (top line) as well as the positioning results of the integrated system. It can be seen that when GPS is available, the maximum error is in the order of 5 m, which approaches the differential GPS

accuracy. As would be expected the accuracy is degraded during the GPS outages; the maximum error is in order of 25 m. However, taking the bus dimension into consideration, it is clear that the obtained positioning solution is still sufficiently precise. One problem with the developed system, however, is that the obtained positioning solution is not smooth. This is mainly due to the way the signpost corrections are applied to the positioning solution of the integrated system. An attempt was made to smooth the positioning solution by fitting the signpost corrections with a polynomial, but was discarded as the solution deteriorated.

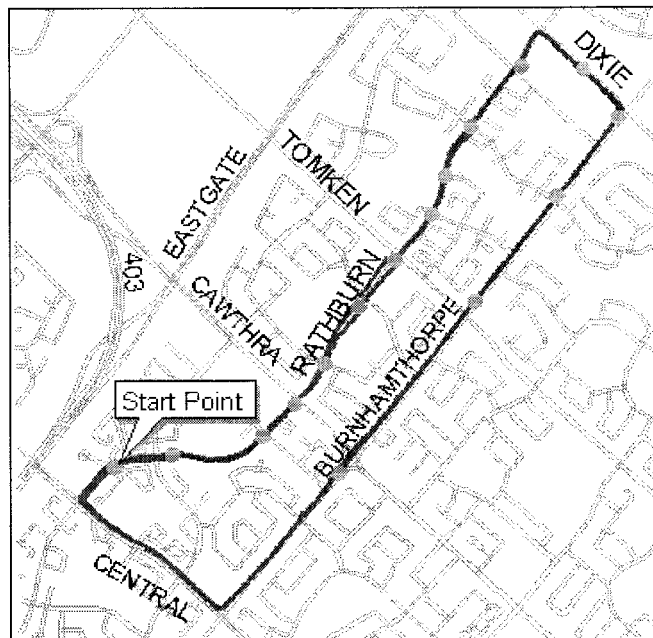


Figure 5.20 DR/GPS/Signpost for 100 seconds GPS outages (Test Two)

#### 5.4.3 Remarks on Open Area Test

Table 5.3 contains some statistics for the two-day test in the open area. According to this table, the DR solution gives poor results, particularly when there is a long bus route

without enough stops to update the gyro bias. The DR/signpost solution was better than DR alone but does not meet the requirements for the bus location. A more precise and reliable integrated system that combines a low-cost autonomous GPS, DR, and signpost has been developed. Preliminary results show that the accuracy of the integrated GPS/DR/signpost system is comparable with that of Differential GPS in unobstructed environments. Also, taking into consideration the bus length, the integrated system gives a good reliable solution.

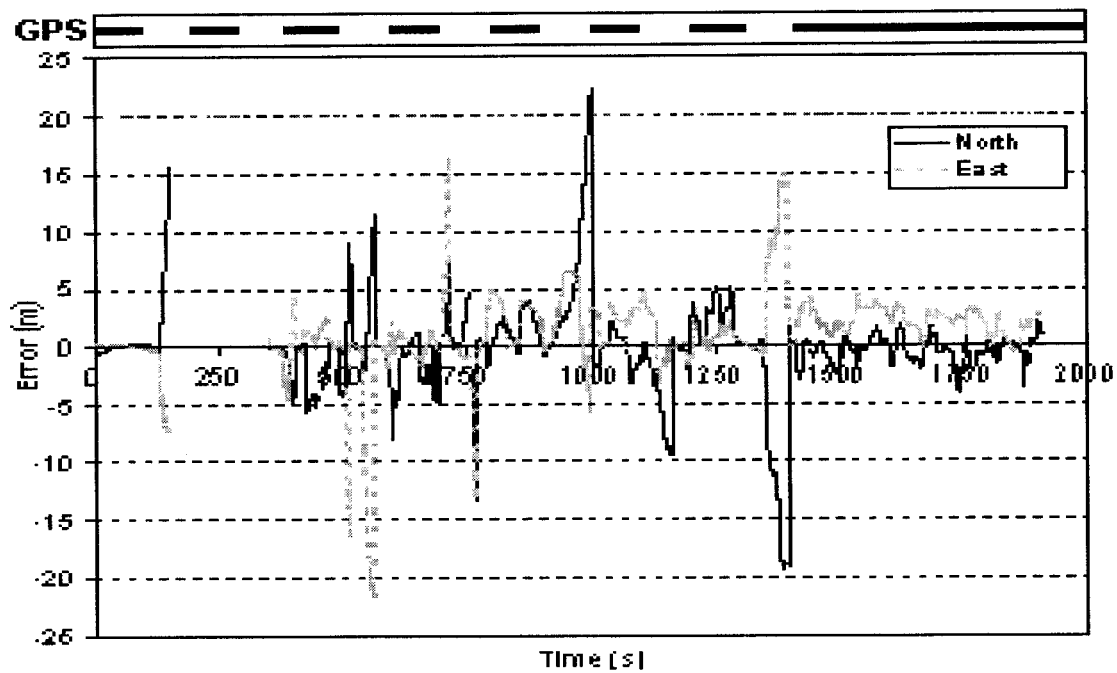


Figure 5.21 GPS/DR/Signpost error for 100 seconds GPS outages (Test Two)

Table 5.3 Results of the open area Test

		Test One		Test Two	
		North	East	North	East
DR alone	Mean (m)	112.60	-89.15	86.21	-76.90
	<b>RMS (m)</b>	<b>122.60</b>	<b>101.48</b>	<b>99.27</b>	<b>90.30</b>
DR/SP	Mean (m)	-3.51	-1.20	3.00	-3.22
	<b>RMS (m)</b>	<b>51.01</b>	<b>42.74</b>	<b>27.81</b>	<b>22.87</b>
DR/SP/GPS	Mean (m)	-0.86	-0.58	-0.40	1.12
	<b>RMS (m)</b>	<b>2.92</b>	<b>1.29</b>	<b>1.88</b>	<b>1.77</b>
DR/SP/GPS 100 second	Mean (m)	2.08	-2.93	-0.44	0.97
	<b>RMS (m)</b>	<b>15.51</b>	<b>19.72</b>	<b>4.71</b>	<b>3.74</b>

## 5.5 MASKED AREA TEST

This test was done in Toronto's downtown core to assess the system under high multipath and masking conditions. The main objective of this test is to investigate and assess the accuracy of the various system combinations in this environment, especially because there is a bus route in that area. Also, the assessment of the integrated system developed here would be more valuable if tested in the field under normal conditions, such as traveling the entire bus route from the start station to the end station, using actual bus stop locations and times.

The test period of approximately 45 minutes gave us the opportunity to make at least two loops. The start point was close to Ryerson University campus. Figure 5.22 shows the number of visible satellites above the 10° elevation angle. As can be seen, no satellites were visible in that area, as there are some bridges around, which obstructed the view of all the satellites.

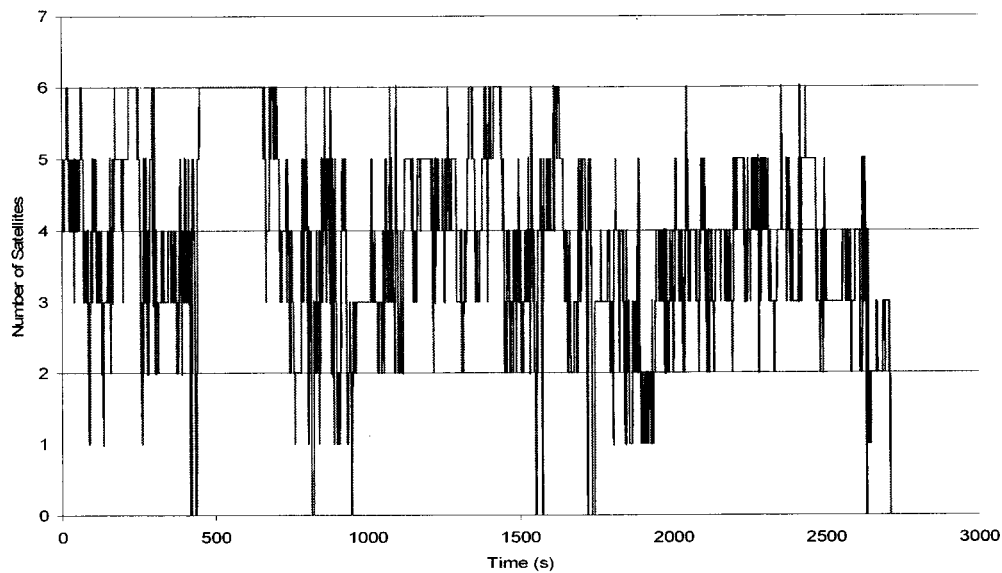


Figure 5.22 Number of Satellite during Downtown Test

### 5.5.1 The DR System Alone

Figure 5.23 shows the solution of the DR system positioning. There was no differential GPS data in this case to compare the results, but we measured the maximum deviation at intersections. The results reveal that the maximum deviation reached 260 m at the southwest intersection. There is no control or update for the DR solution over time.

### 5.5.2 The DR/Signpost Solution

As it can be seen in Figure 5.24, there are 14 stops along the test route where the DR solution can be updated. In fact, it is very difficult to stop at each stop for 20 seconds due to the heavy traffic in downtown Toronto.

The results of this scenario emphasize that the DR/signpost integrated system is better than DR stand-alone. The final solution of the DR/signpost system is compared with the digital map road centerlines. The maximum deviation reached 150 m and occurred where



there are no updates from the signpost for a relatively long time. However, the normal deviation is around 70 m when following the signpost actual update.

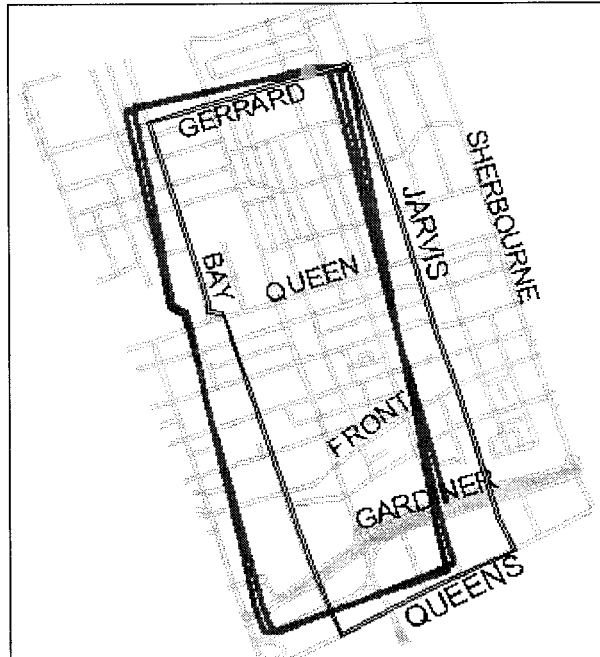


Figure 5.23 DR System alone (Downtown Test)

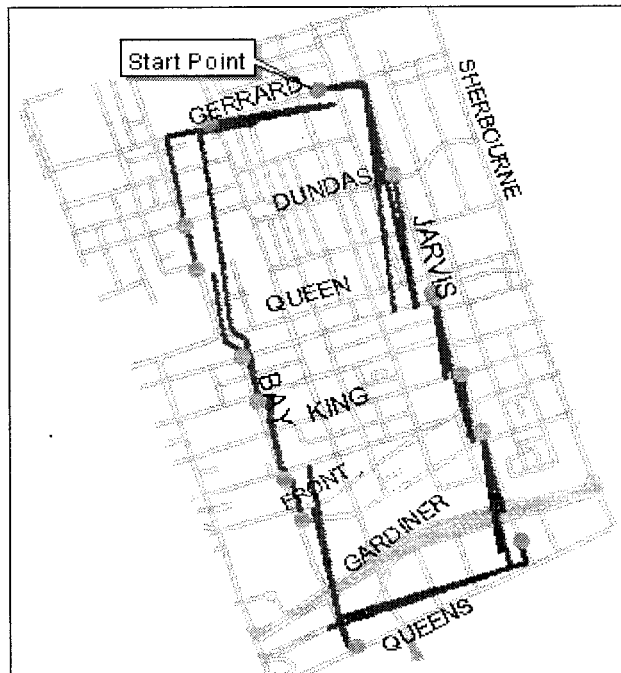


Figure 5.24 DR/signpost solution (Downtown Test)

### 5.5.3 The DR/GPS Solution

As mentioned earlier, this scenario is conducted under the assumption of no signpost signal for any reason. In fact, the solution is not accurate enough especially where GPS signals are blocked for long time also where the number of satellites is four with bad satellite configuration. From Figure 5.25, the maximum error is around 80.0 m (circle A) and the solution is not smooth (shape B).

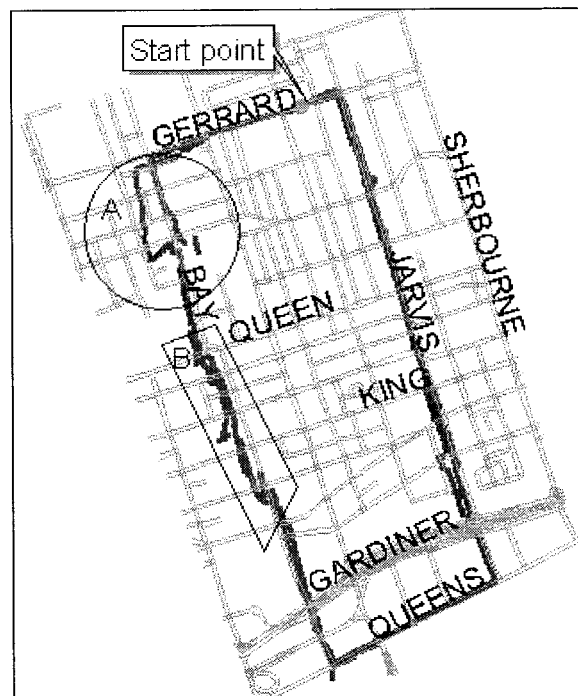


Figure 5.25 DR/GPS solution (Downtown Test)

### 5.5.4 GPS/DR/Signpost Integrated System

As would be expected, the GPS only solution in downtown area is rather poor. It can be seen in Figure 5.25 that there is a large error, particularly in the direction perpendicular to the car motion, which is attributed to the combined effects of bad geometry and multipath.

To overcome the limitation of both GPS and conventional systems, data from all sensors were fused within a Kalman filter as discussed in Chapter 4. It can be seen from Figure 5.26 that the solution of the integrated GPS/DR/signpost system is better than any of the systems alone. The analysis also shows that the average deviation from the road centre varies between 30 m and 50 m.

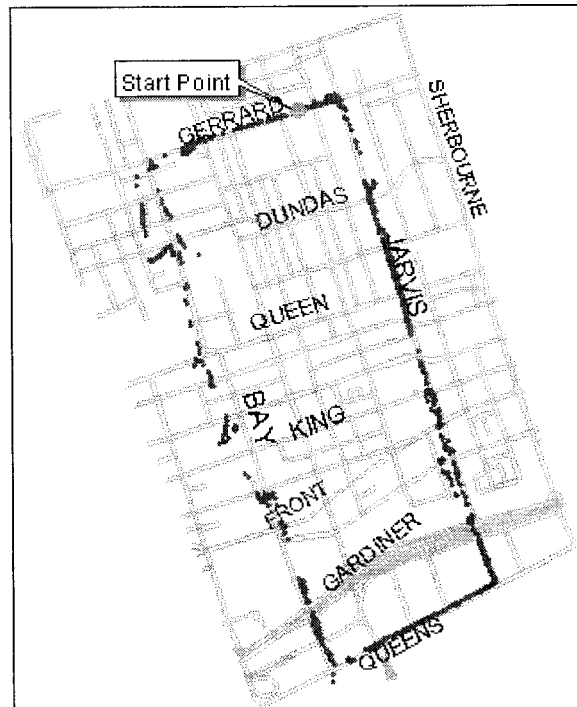


Figure 5.26 GPS solution when the number of satellites is 4 or more (Downtown Test)

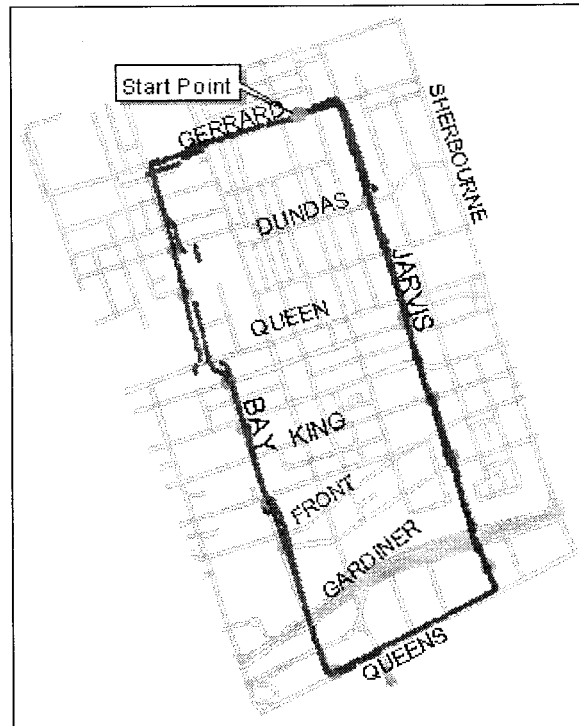


Figure 5.27 GPS/DR/SP integrated system (Downtown Test)

## **CHAPTER 6**

### **CONCLUSIONS AND RECOMMENDATIONS**

#### **6.1 CONCLUSIONS**

An integrated positioning system was developed, which combines GPS with the existing DR/signpost system. DR provides continuous positioning coverage, with signposts aiding in the position domain and GPS aiding in the time domain. A centralized Kalman filter was designed to fuse all the available data and estimate the final position.

To evaluate the integrated system, a hardware layout was designed in addition to the needed connections. Time synchronization is a critical element for multi-sensor fusion. Off-the-shelf software was used to synchronize all sensors' output with the same time tag, taking GPS time as a reference. Bus stops were precisely surveyed using differential GPS and were used to simulate the signposts.

Multiple practical tests were conducted under various conditions. Two tests were conducted in an open area to investigate the system performance under fairly good conditions, i.e., dry roads and no GPS signal obstruction. Subsequently, the GPS data were obstructed artificially. A third test was carried out in downtown Toronto to evaluate the performance of the developed system under masking and multipath conditions.

Based on this research, the following conclusions can be drawn:

- The performance of the DR system was very poor, especially if there is no position update from signposts. The maximum deviation in the north and east directions were 230 m and 200 m, respectively. However, these numbers were

higher for the bad road conditions. Frequent stops slightly improved the DR system through estimating the gyro drift offset without position update.

- The performance of the DR/signpost system is better than that of the DR alone, as the signpost updates the system and control the DR drift. The maximum deviation in the north and east directions compared to differential GPS were around 135 m and 115 m, respectively. However, this solution becomes poor when the distance between the signposts increases or when the travel time is increased, as in the case of high-density traffic.
- GPS alone provides consistent positioning accuracy at the few tens of metres, but suffers from limitations in urban areas. Therefore, an optimal solution could be obtained by integrating GPS with the conventional systems.
- The open sky test reveals that the GPS/DR/signpost integrated system gives a maximum deviation of 12.0 m and 3.5 m in the north and east directions, respectively. However, this accuracy degraded in case of GPS outages for 100 seconds with 23.0 m and 22.5 m maximum deviation in the north and east directions, respectively, but still good accuracy compared with the bus dimensions.
- The results of the downtown test (urban area) show that a continuous positioning solution with sufficient accuracy could be attained with the DR system, provided that aid from either GPS or signpost system is received. Two facts can be derived from this test: the less distance between the signposts, the more accurate will be

the results obtained; and the less time between updates during GPS outages, the more accurate the position can be obtained.

## **6.2 RECOMMENDATIONS**

Based on the above conclusions, it would be helpful to provide the following recommendations regarding improved performance and plans for the future:

- The signpost coverage should be intensified in the downtown core Toronto and be removed in open areas.
- Conventional odometers and gyros should be replaced with the newly developed Micro-electro-mechanical system (MEMS)-based inertial sensors. Inertial navigation systems are capable of measuring the actual bus speed without reference to wheels, which are affected by a number of factors including road conditions and tire pressure.
- Map matching information could likely control large errors, especially in urban areas. Further studies must be done to investigate its effect on the integrated system.

## REFERENCES

- Abbott, E. and D. Powell (1999). "Land-Vehicle Navigation Using GPS." Proceedings of the IEEE. Vol. 87, No. 1, pp. 145-162.
- Abd El-Gelil, M. and A. El-Rabbany (2002). "High Accuracy, Low Cost Autonomous Navigation System for Public Transportation." Proceedings of the ION GPS, Oregon Convention Centre, Portland, Oregon, USA, September 24-27. pp. 1766-1770, CD-ROM.
- Abd El-Gelil, M. and A. El-Rabbany (2003). "Assessment of Various Integrated Navigation Systems for Public Transportation." Proceedings of the Institute of Navigation National Technical Meeting, ION NTM 2003, Anaheim, California, USA, 22-24 January. CD-ROM.
- Aein, J. M. (1995). "An Optical Signal Processing Model for the Interferometric Fiber Optic Gyroscope." RAND, Santa Monica, CA, USA.
- Barbour, N. and G. Schmidt (2001). "Inertial Sensor Technology Trends." IEEE Sensors Journal, Vol. 1, No. 4, pp. 332-339.
- Bennett, S. M., R. Dyott, D. Allen, J. Brunner, R. Kidwell., and R. Miller. (1998). "Fiber Optic Rate Gyros as Replacement for Mechanical Gyros." AIAA, Vol. 44, No. 1.
- Borenstein, J. (1998). "Experimental Evaluation of a Fiber Optics Gyroscope for Improving Dead-Reckoning Accuracy in Mobile Robots." Proceedings of the IEEE International Conference on Robotics and Automation, Leuven, Belgium, May 16-21, pp. 3456-3461.
- Brown R. G., and P. Hwang (1997). *Introduction to Random Signals and Applied Kalman Filtering*. John Wiley & Sons, Inc., Toronto, Canada.
- Bullock, J. B. (1995). "A Prototype Portable Vehicle Navigation System Utilizing Map Aided GPS." Master's thesis, Report No. 20081, Department of Geomatics Engineering, The University of Calgary, Calgary, Canada.



- Burdess, J. S., A. J. Harris, J. Cruickshank, D. Wood, and G. Cooper (1994). "A Review of Vibratory Gyroscopes." *Engineering Science and Education Journal*, Vol. 3, No. 6, pp. 249-254.
- Da, R. and G. Dedes (1995). "Nonlinear Smoothing of Dead Reckoning Data with GPS Measurements." *Proceedings of the ION GPS*, Palm Springs, California, September 12-15, pp. 1285-1294.
- Drane, C. and C. Rizos (1997). *Positioning Systems in Intelligent Transportation Systems*. Artech House, Boston.
- El-Rabbany, A., A. Shalaby, and S. Zolfaghari (2000). "Real-time Bus Location, Passenger Information and Scheduling for Public Transportation." Presented at the GPS meeting, GEOIDE 2000 Conference, Calgary, Alberta, May 24-26.
- El-Rabbany, A. (2002). *Introduction to GPS: The Global Positioning System*. Artech House, Boston.
- El-Rabbany, A. and M. Abd El-Gelil (2003). "Positioning Toronto's Transit Vehicles: Integrating Low-cost GPS, Odometers, Gyros and Signposts." Invited Article. *GIM International*, Vol. 17, No. 4, pp. 68-71.
- El-Sheimy, N. (2002). "Inertial Techniques and INS/DGPS Integration." Course Notes, GEOIDE Summer School, University of Toronto, Scarborough, May 29-30.
- Fraden, J. (1997). *Handbook of Modern Sensors: Physics, Designs, and Applications*. American Institute of Physics, Woodbury, New York.
- French, R. L. (1986). "Historical Overview of Automobile Navigation Technology." *Proceedings of the 36<sup>th</sup> IEEE vehicular Technology Conference*, Dallas, Texas, May 20-22, pp. 350-358
- G&S Engineering. Magnetic Sensors.  
<http://www.bioweb.net/mfg/gsengineering/hall.shtml>.
- Gelb, A. (1974). *Applied Optimal Estimation*. The MIT. Press, Cambridge.

- Greenough, J. and R. Noehammer (1999). "ITS Technology Solving Bus Transit Priority Needs – The Better Way Gets Better." Proceedings of the ITS Congress, Toronto, Ontario, Canada, CD-ROM.
- Harris, C. B. (1989). "Prototype for a Land Based Automatic Vehicle Location and Navigation System." Master's thesis, Report No. 20033, Department of Geomatics Engineering, The University of Calgary, Calgary, Canada.
- Harvey, R. S. (1998). "Development of a Precision Pointing System Using an Integrated Multi-Sensor Approach." Master's thesis, Report No. 20117, Department of Geomatics Engineering, The University of Calgary, Calgary, Canada.
- Hayashi, N. (1996). "Augmentation of GPS with a Barometer and a Heading Rate Gyroscope for Urban Vehicular Navigation." Master's thesis, Report No. 20098, Department of Geomatics Engineering, The University of Calgary, Calgary, Canada.
- Hofmann-Wellenhof, B, H. Lichtenegger, and J. Collins (2001). *GPS Theory and Practice*. 5<sup>th</sup> ed., Springer-Verlag, New York.
- IGS (2001). "International GPS Service Annual Report 2000." IGS Central Bureau, Jet Propulsion Laboratory, Pasadena, California, pp. 14-16.
- Ishikawa, S., H. Maeda, A. Shibata, and F. Morisue (1995). "Hybrid GPS for Land Vehicle." Proceedings of ION GPS, Palm Spring, California, September 12-15, pp. 1301-1306.
- Jefferson, D. and Y. Bar-Sever. (2000). "Accuracy and Consistency of Broadcast GPS Ephemeris Data." Proceedings of ION GPS, Salt Lake City, Utah, September 19-22, pp. 438-446.
- Jekeli, C. (2001). *Inertial Navigation Systems with Geodetic Applications*. Walter de Gruyter, New York, NY., USA.
- Kaplan, E. (1996). *Understanding GPS: Principles and Applications*. Artech House, Boston.
- KVH Industries, Inc. (1999). "KVH E-Core 1000 Fiber Optic Gyro." Technical Manual.

- Lachapelle, G. (1991). "Capabilities of GPS for Airborne Remote Sensing." *Canadian Journal of Remote Sensing*, Vol. 17, No. 4, pp. 305-312.
- Lachapelle, G., A. Bruton, J. Henriksen, M. E. Cannon, and C. McMillan (1996a). "Evaluation of High Performance Multipath Reduction Technologies for Precise DGPS Shipborne Positioning." *The Hydrographic Journal*, Number 82, October, pp. 11-17.
- Lawrence, A. (1998). *Modern Inertial Technology: Navigation, Guidance, and Control*. 2<sup>nd</sup> ed., Springer-Verlag, New York.
- Lefevre, H. (1993). *The Fiber Optic Gyroscope*. Artech House, Boston.
- Leick, A. (1995). *GPS Satellite Surveying*. 2<sup>nd</sup> ed., John Wiley and Sons, Inc.
- Magellan Corporation (1998). "G8™ GPS OEM Board." Reference Manual.
- Mark, J., D. Tazartes, B. Fidric, and A. Cordova (1991). "A Rate Integrating Fiber Optic Gyro." *Navigation: Journal of the Institute of Navigation*, Vol. 38, No. 4, pp. 341-352.
- Okunieff, P. (1997). "Synthesis of Transit Practice 24, AVL Systems for Bus Transit." Cambridge Systematics, Inc.
- Olynik, M. C. (2002). "Temporal Characteristics of GPS Error Sources and Their Impact on Relative Positioning." Master's thesis, Report No. 20162, Department of Geomatics Engineering, The University of Calgary, Calgary, Canada.
- Pekilis, B. and G. Heti (1992). "Automatic Vehicle Location and Control Systems for Small and Medium Ontario Transit Properties: Phase 1 Report (Final)". Transportation Technology and Energy Branch, Ministry of Transportation of Ontario.
- Rabie, T., A. Shalaby, B. Abdulhai and A. El-Rabbany (2003). "Mobile Active-Vision Traffic Surveillance in Urban Networks." Paper submitted to The international journal of Computer-Aided Civil and Infrastructure Engineering.
- Raquet, J. (1998). "Development of a Method for Kinematic GPS Carrier-Phase Ambiguity Resolution Using Multiple Reference Receivers." Ph.D. thesis, Report

- No. 20116, Department of Geomatics Engineering, University of Calgary, Calgary, Canada.
- Ray, J. (2000). "Mitigation of GPS Code and carrier-phase Multipath Effects Using a Multi-Antenna System." Ph.D. thesis, Report No. 20136, Department of Geomatics Engineering, University of Calgary, Calgary, Canada.
- Rogers, R. M. (2000). *Applied Mathematics in Integrated Navigation Systems*. AIAA Education Series.
- Ryan, S. J. (2002). "Augmentation of DGPS for Marine Navigation." Ph.D. thesis, Report No. 20164, Department of Geomatics Engineering, University of Calgary, Calgary, Canada.
- Senior J. (1993). *Fiber Optic Data Transmission*. Prentice Hall.
- Shalaby, A., L. Fu, A. El-Rabbany, S. Zolfaghari, M. Jaber and T. Sayed (2002). "Real-Time Bus Location, Passenger Information and Scheduling for Public Transportation." Presented at the 4<sup>th</sup> GEOIDE Annual Meeting, Toronto, 22-24 May.
- Stephen, J. (2000). "Development of a Multi-Sensor GNSS Based Vehicle Navigation System." Master's thesis, Report No. 20140, Department of Geomatics Engineering, The University of Calgary, Calgary, Canada.
- Stephen, J. and G. Lachapelle (2000). "Development of a GNSS-based Multi-sensor Vehicle Navigation System." Proceedings of the NTM GPS-2000, Alexandria, VA., USA, pp. 268-278, CD-ROM.
- Tsakiri, M., A. Kealy, and M. Stewart (1999). "Urban Canyon Vehicle Navigation with Integrated GPS/GLONASS/DR systems." *Navigation: Journal of The US Institute of Navigation*, Vol. 46, No. 3, pp. 161-174.
- Welch G. and G. Bishop (2001). "An Introduction to the Kalman Filter." TR 95-041, Department of Computer Science, University of North Carolina at Chapel Hill.
- Wells, D. E., N. Beck, D. Delikaraoglou, A. Kleusberg, E. J. Krakiwsky, G. Lachapelle, R. B. Langley, M. Nakiboglou, K. P. Schwarz, J. Tranquilla, and P. Vanicek

- (1987). *Guide to GPS Positioning*. Canadian GPS Associates, Fredericton, New Brunswick.
- Yazdi, N., F. Ayazi, , and K. Najafi, (1998). "Micromachined Inertial Sensors." *Proceedings of the IEEE*, Vol. 86, No. 8, pp. 1640-1659.
- Zhang, Z. (1997). "Impact of Rubidium Clock Aiding on GPS Augmented Vehicular Navigation." Master's thesis, Report No. 20112, Department of Geomatics Engineering, The University of Calgary, Calgary, Canada.
- Zhao, Y. (1997). *Vehicle Location and Navigation Systems*. Artech House, Boston.
- Zickel, R. and N. Nehemia (1994). "GPS Aided Dead Reckoning Navigation." *Proceedings of NTM GPS*, Santa Monica, CA, USA, January, 24-26, pp. 577-586.